A Three-Dimensional Coupled Mode Solution for Range-Dependent Waveguides

by

Wenyu Luo

Submitted in partial fulfillment of the requirements for the degrees of

Master of Science in Ocean Engineering/Applied Ocean Science and Engineering

at the

MASSACHUSETTS INSTITUTE OF TECHNOLOGY

and the

WOODS HOLE OCEANOGRAPHIC INSTITUTION

and

Master of Science in Electrical Engineering and Computer Science

at the

MASSACHUSETTS INSTITUTE OF TECHNOLOGY

February 2005

Author . . . .
Joint Program in Ocean Engineering/Applied Ocean Science and Engineering
February, 2005

Certified by . . . .
Henrik Schmidt
Professor of Ocean Engineering
Thesis Supervisor

Certified by . . . .
Arthur B. Baggeroer
Professor of Ocean Engineering and Electrical Engineering and Computer Science
Ford Professor of Engineering
Thesis Reader

Accepted by . . . .
Michael S. Triantafyllou, Professor of Ocean Engineering
Chairman, Department Committee on Graduate Students
Department of Ocean Engineering

Accepted by . . . .
Arthur C. Smith, Professor of Electrical Engineering and Computer Science
Chairman, Department Committee on Graduate Theses
Department of Electrical Engineering and Computer Science

Accepted by . . . .
Mark Grosenbaugh
Chair, Joint Committee of Applied Ocean Science and Engineering
Massachusetts Institute of Technology/Woods Hole Oceanographic Institution

A Three-Dimensional Coupled Mode Solution for Range-Dependent Waveguides

by

Wenyu Luo

Abstract

Despite the great achievements obtained with fast-field and parabolic equation models, normal mode programs still remain a very efficient, simple and practical tool for describing ocean acoustics in range-independent environments.

Numerical implementations of wave-theory solutions for range-dependent acoustic problems can be classified as: normal-mode techniques (adiabatic or coupled modes); parabolic-approximation techniques (narrow- or wide-angle parabolic equations solved by split-step or finite-difference techniques); and finite-element/finite-difference solutions of the full wave equation.

The mode techniques provide approximate field solutions if implemented in the adiabatic approximation, while complete wave theory solutions can be obtained by including full mode coupling.

Parabolic approximations to the elliptic wave equation have been extensively studied over the past 10 years([15], [23]). The advantage of using a parabolic wave equation is that it can be efficiently solved by noniterative forward marching techniques. However, any form of the parabolic equation is an approximate wave equation derived under the assumptions of: (1) forward propagation only, and (2) that energy is propagating within a limited angular spectrum around the main propagation direction.

The last category of models based on finite-difference and finite-element solutions of the full wave equation([22]) is well suited for providing solutions for propagation in general range-dependent environments. The existing codes, however, are extremely computer intensive.

My thesis focuses on a two-dimensional two-way coupled modes model, and then expend it to a three-dimensional coupled modes model for two-dimensional, range-dependent waveguides. Numerical examples of two-dimensional and three-dimensional problems are presented, and comparisons with the results from analytical solution, as well as from COUPLE are also considered.

Thesis Supervisor: Henrik Schmidt
Professor of Ocean Engineering

Thesis Reader: Arthur B. Baggeroer
Professor of Ocean Engineering and Electrical Engineering and Computer Science
Ford Professor of Engineering

Acknowledgments

Contents

List of Figures

11

13

List of Tables

Chapter 1

The Method of Normal Modes

1.1 Introduction

Normal modes method is a widely used approach in underwater acoustics. First, we develop the theory for a point source in a horizontally stratified, fluid medium, illustrating the dependency of the technique of separation of variables and Sturm-Liouville theory. We then apply the normal modes method to the ideal waveguides, i.e., a waveguide with a soft top and a hard bottom, or a waveguide with a soft top and a soft bottom. Next, we apply the normal modes method to the Pekeris waveguide, which consists of a homogeneous fluid layer bounded above by a soft top and below by a higher velocity, homogeneous fluid half-space. In this case, the modal field is composed of both discrete and continuous spectra, and the continuous spectrum can be approximatted by a sum of discrete modes, which are referred to as improper modes (or virtual modes, leaky modes). Finally, we derive the modal field for the case of a line source in plane geometry. See [11] and [14] for a more detailed discussion about the method of normal modes.

17

1.2 A Point Source in a Horizontally Stratified, Fluid Medium in Cylindrical Geometry

We consider a point source with cylindrical coordinates $(0, z_s)$ in a horizontally stratified medium with density $\rho(z)$ and sound speed $c(z)$, as shown in Fig. 1-1. We assume the waveguide involves a pressure-release (soft) surface at $z = 0$ and a perfect rigid (hard) bottom at $z = D$.
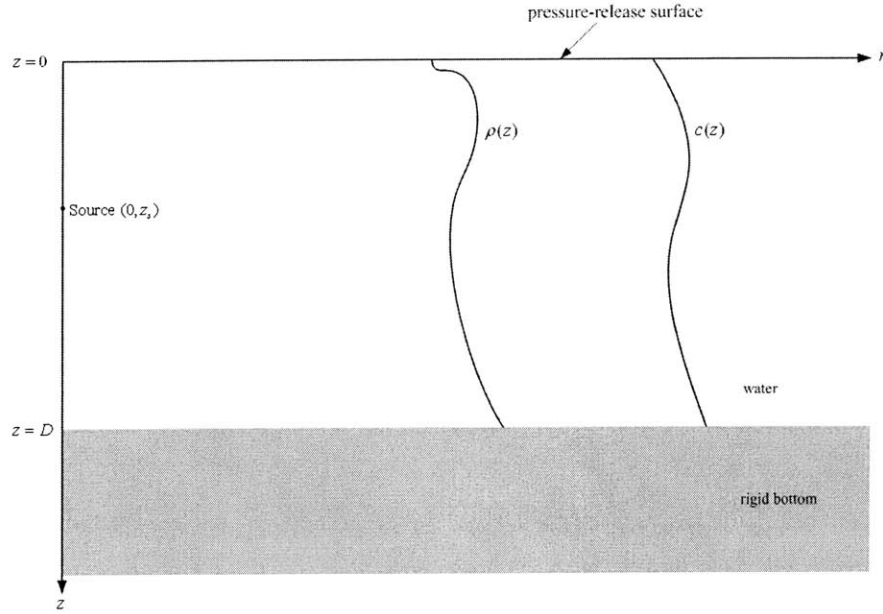
Figure 1-1: Geometry of a point source in a horizontally stratified, fluid medium.

The Helmholtz equation of this problem is[14]

$$\frac{1}{r}\frac{\partial}{\partial r}\left(r\frac{\partial p}{\partial r}\right) + \rho(z)\frac{\partial}{\partial z}\left(\frac{1}{\rho(z)}\frac{\partial p}{\partial z}\right) + \frac{\omega^2}{c^2(z)}p = -\frac{\delta(r)\delta(z - z_s)}{2\pi r}, \qquad (1.1)$$

First, we seek a solution of the unforced equation of Eq. (1.1), i.e.

$$\frac{1}{r}\frac{\partial}{\partial r}\left(r\frac{\partial p}{\partial r}\right) + \rho(z)\frac{\partial}{\partial z}\left(\frac{1}{\rho(z)}\frac{\partial p}{\partial z}\right) + \frac{\omega^2}{c^2(z)}p = 0. \qquad (1.2)$$

Using separation of variables, we substitute $p(r, z) = \Phi(r)\Psi(z)$ into Eq. (1.2), and

divide through by $\Phi(r)\Psi(z)$, we have

$$\frac{1}{\Phi}\left[\frac{1}{r}\frac{\mathrm{d}}{\mathrm{d}r}\left(r\frac{\mathrm{d}\Phi}{\mathrm{d}r}\right)\right] + \frac{1}{\Psi}\left[\rho(z)\frac{\mathrm{d}}{\mathrm{d}z}\left(\frac{1}{\rho(z)}\frac{\mathrm{d}\Psi}{\mathrm{d}z}\right) + \frac{\omega^2}{c^2(z)}\Psi\right] = 0. \tag{1.3}$$

Each component of Eq. (1.3) is equal to a separation constant, denoted by k_{rm}^2, thus we obtain the depth-separated equation

$$\rho(z)\frac{\mathrm{d}}{\mathrm{d}z}\left[\frac{1}{\rho(z)}\frac{\mathrm{d}\Psi_m(z)}{\mathrm{d}z}\right] + \left[\frac{\omega^2}{c^2(z)} - k_{rm}^2\right]\Psi_m(z) = 0. \tag{1.4}$$

The modal equation Eq. (1.4), together with boundary conditions

$$\text{soft surface: } \Psi_m(0) = 0, \tag{1.5}$$

$$\text{rigid bottom: } \left.\frac{\mathrm{d}\Psi_m(z)}{\mathrm{d}z}\right|_{z=D} = 0, \tag{1.6}$$

is a proper *Sturm-Liouville* problem, with weighting function $w(z) = \frac{1}{\rho(z)}$.

The main properties of a proper *Sturm-Liouville* problem are as follows:

1. The eigenfunctions $\Psi_m(z)$ satisfy a *Sturm-Liouville* equation on the interval $0 \le z \le D$. At the endpoints $z = 0$ and $z = D$, $\Psi_m(z)$ satisfy one of the conditions listed below:

   (a) *Dirichlet*[1]

   (b) *Neumann*[2]

   (c) periodic, i.e., $\rho(0) = \rho(D)$, $\Psi_m(0) = \Psi_m(D)$, and $\left.\frac{\mathrm{d}\Psi_m}{\mathrm{d}z}\right|_{z=0} = \left.\frac{\mathrm{d}\Psi_m}{\mathrm{d}z}\right|_{z=D}$

---

[1]For a soft, or pressure-release, boundary S, the pressure vanishes on the boundary:

$$p|_S = 0.$$

This condition is also known as a *Dirichlet* boundary condition([11, p. 33]).

[2]For a hard boundary S, the normal velocity, i.e., the derivative of the pressure normal to the boundary, vanishes on S:

$$\left.\frac{\partial p}{\partial n}\right|_S = 0.$$

This condition is also known as a *Neumann* boundary condition([11, p. 33]).

(d) mixed boundary conditions of the type $A\Psi_m(z) + B\frac{\mathrm{d}\Psi_m(z)}{\mathrm{d}z} = 0$, where A and B are real constants.

2. The modal equation has an infinite number of solutions which are like the modes of a vibrating string. The modes are characterized by a mode shape function, known as eigenfunctions, $\Psi_m(z)$, and a horizontal propagation constant, known as eigenvalues, k_{rm}.

3. $\Psi_m(z)$ has m zeros in the interval $[0, D]$.

4. The eigenfunctions are orthonormal with respect to the weighting function $w(z) = \frac{1}{\rho(z)}$, i.e.,

$$\int_0^D w(z)\Psi_m(z)\Psi_n(z)\mathrm{d}z = \int_0^D \frac{1}{\rho(z)}\Psi_m(z)\Psi_n(z)\mathrm{d}z$$
$$= \delta_{nm},$$

where δ_{nm} is the *Kronecker* delta.

5. The eigenfunctions $\Psi_m(z)$ constitute a complete set in the sense that an arbitrary function $f(z)$ can be expanded in terms of them:

$$f(z) = \sum_m c_m \Psi_m(z),$$

where c_m are the coefficients of the expansion.

6. The eigenfunction $\Psi_m(z)$ satisfy the completeness relation:

$$\sum_m w(z_0)\Psi_m^*(z_0)\Psi_m(z) = \sum_m \frac{1}{\rho(z_0)}\Psi_m^*(z_0)\Psi_m(z)$$
$$= \delta(z - z_0).$$

This property can be easily proven with Property 5.

We represent the pressure field as

$$p(r, z) = \sum_{m=1}^{\infty} \Phi_m(r) \Psi_m(z), \tag{1.7}$$

and substitute this into Eq. (1.1), then we obtain

$$\sum_{m=1}^{\infty} \left\{ \frac{1}{r} \frac{\mathrm{d}}{\mathrm{d}r} \left(r \frac{\mathrm{d}\Phi_m(r)}{\mathrm{d}r} \right) \Psi_m(z) + \Phi_m(r) \left[\rho(z) \frac{\mathrm{d}}{\mathrm{d}z} \left(\frac{1}{\rho(z)} \frac{\mathrm{d}\Psi_m(z)}{\mathrm{d}z} \right) + \frac{\omega^2}{c^2(z)} \Psi_m(z) \right] \right\}$$
$$= -\frac{\delta(r)\delta(z - z_s)}{2\pi r}. \tag{1.8}$$

Inserting the depth-separated equation, Eq. (1.4), into Eq. (1.8), we obtain

$$\sum_{m=1}^{\infty} \left\{ \frac{1}{r} \frac{\mathrm{d}}{\mathrm{d}r} \left(r \frac{\mathrm{d}\Phi_m(r)}{\mathrm{d}r} \right) \Psi_m(z) + k_{rm}^2 \Phi_m(r)\Psi_m(z) \right\} = -\frac{\delta(r)\delta(z - z_s)}{2\pi r}. \tag{1.9}$$

Apply the operator

$$\int_0^D (\cdot) \frac{1}{\rho(z)} \Psi_n(z)\mathrm{d}z,$$

to Eq. (1.9), we obtain the range-separated equation,

$$\frac{1}{r} \frac{\mathrm{d}}{\mathrm{d}r} \left[r \frac{\mathrm{d}\Phi_n(r)}{\mathrm{d}r} \right] + k_{rn}^2 \Phi_n(r) = -\frac{\delta(r)\Psi_n(z_s)}{2\pi r \rho(z_s)}. \tag{1.10}$$

The solution to Eq. (1.10) is

$$\Phi_n(r) = \frac{i}{4\rho(z_s)} \Psi_n(z_s) H_0^{(1)}(k_{rn}r). \tag{1.11}$$

Thus we obtain the pressure field

$$p(r, z) = \sum_{m=1}^{\infty} \Phi_m(r)\Psi_m(z)$$
$$= \frac{i}{4\rho(z_s)} \sum_{m=1}^{\infty} \Psi_m(z_s)\Psi_m(z) H_0^{(1)}(k_{rm}r). \tag{1.12}$$

In the far field ($k_{rm}r \gg 1$), we can substitute the asymptotic form for the Hankel

21

function,

$$H_0^{(1)}(z) \sim \sqrt{\frac{2}{\pi z}} e^{i\left(z - \frac{\pi}{4}\right)},$$
(1.13)

into Eq. (1.12), and obtain

$$p(r, z) \simeq \frac{i}{\rho(z_s)\sqrt{8\pi r}} e^{-i\frac{\pi}{4}} \sum_{m=1}^{\infty} \Psi_m(z_s)\Psi_m(z)\frac{e^{ik_{rm}r}}{\sqrt{k_{rm}}}$$
(1.14)

1.3 Normal Modes for the Ideal Waveguides

1.3.1 Normal Modes for a Homogeneous Fluid Layer with a Soft Top and a Hard Bottom

We consider an ideal waveguide with a homogeneous water layer bounded by a soft top and a hard bottom, the depth-separated equation, Eq. (1.4), becomes

$$\frac{d^2\Psi_m(z)}{dz^2} + \left[\frac{\omega^2}{c^2} - k_{rm}^2\right]\Psi_m(z) = 0,$$
(1.15)

with boundary conditions

$$\Psi_m(0) = 0,$$
(1.16)

$$\left.\frac{d\Psi_m(z)}{dz}\right|_{z=D} = 0.$$
(1.17)

Since

$$k_{zm}^2 = k^2 - k_{rm}^2$$

$$= \frac{\omega^2}{c^2} - k_{rm}^2,$$

Eq. (1.15) is therefore

$$\frac{d^2\Psi_m(z)}{dz^2} + k_{zm}^2\Psi_m(z) = 0.$$
(1.18)

22

The general solution to Eq. (1.18) is

$$\Psi_m(z) = A\sin(k_{zm}z) + B\cos(k_{zm}z), \tag{1.19}$$

satisfying the boundary condition at surface, $\Psi_m(0) = 0$, we obtain $B = 0$, and the boundary condition at $z = D$ leads to

$$Ak_{zm}\cos(k_{zm}D) = 0,$$

thus

$$k_{zm}D = \left(m - \frac{1}{2}\right)\pi, \qquad m = 1, 2, \ldots$$

and we obtain the eigenvalues

$$\begin{aligned}
k_{rm} &= \sqrt{k^2 - k_{zm}^2} \\
&= \sqrt{k^2 - \left[\left(m - \frac{1}{2}\right)\frac{\pi}{D}\right]^2}, \qquad m = 1, 2, \ldots
\end{aligned} \tag{1.20}$$

The eigenfunctions are given by

$$\Psi_m(z) = A\sin(k_{zm}z),$$

where A can be obtained by the orthonormal property,

$$\begin{aligned}
\int_0^D \frac{1}{\rho(z)}\Psi_m^2(z)\mathrm{d}z &= \int_0^D \frac{1}{\rho}A^2\sin^2(k_{zm}z)\mathrm{d}z \\
&= \frac{A^2}{\rho}\frac{D}{2} \\
&= 1,
\end{aligned}$$

which leads to

$$A = \sqrt{\frac{2\rho}{D}},$$

thus the normalized eigenfunctions are

$$\Psi_m(z) = \sqrt{\frac{2\rho}{D}} \sin(k_{zm}z),$$ (1.21)

where

$$k_{zm} = \left(m - \frac{1}{2}\right)\frac{\pi}{D}, \quad m = 1, 2, \ldots$$

The pressure field is therefore

$$
\begin{aligned}
p(r, z) &= \frac{i}{4\rho(z_s)} \sum_{m=1}^{\infty} \Psi_m(z_s)\Psi_m(z)H_0^{(1)}(k_{rm}r) \\
&= \frac{i}{4\rho} \sum_{m=1}^{\infty} \frac{2\rho}{D} \sin(k_{zm}z_s) \sin(k_{zm}z)H_0^{(1)}(k_{rm}r) \\
&= \frac{i}{2D} \sum_{m=1}^{\infty} \sin(k_{zm}z_s) \sin(k_{zm}z)H_0^{(1)}(k_{rm}r).
\end{aligned}
$$ (1.22)

Number of propagating (in range) modes

The propagating modes have real eigenvalues,

$$k_{rm} = \sqrt{k^2 - k_{zm}^2},$$

so,

$$k_{zm} \leq k,$$

inserting in $k_{zm} = (m - \frac{1}{2})\frac{\pi}{D}$ and $k = \frac{2\pi}{\lambda}$, we have

$$(m - \frac{1}{2})\frac{\pi}{D} \leq \frac{2\pi}{\lambda},$$

thus, we get the number of propagating modes

$$M = \left[\frac{2D}{\lambda} + \frac{1}{2}\right] \approx \left[\frac{2D}{\lambda}\right] \quad \text{for } \frac{D}{\lambda} \gg \frac{1}{4}.$$ (1.23)

where $[x]$ rounds x to the nearest integer towards infinity.

For long-range propagation, we can obtain a good approximation to the total field

24

by retaining the propagating modes only.

1.3.2 Normal Modes for a Homogeneous Fluid Layer with a Soft Top and a Soft Bottom

We consider a waveguide with a homogeneous water layer bounded by a soft top and a hard bottom, the depth-separated equation is

$$\frac{\mathrm{d}^2\Psi_m(z)}{\mathrm{d}z^2} + k_{zm}^2\Psi_m(z) = 0, \tag{1.24}$$

with boundary conditions

$$\Psi_m(0) = 0, \tag{1.25}$$

$$\Psi_m(D) = 0. \tag{1.26}$$

The general solution to Eq. (1.24) is

$$\Psi_m(z) = A\sin(k_{zm}z) + B\cos(k_{zm}z).$$

The boundary condition at surface, $\Psi_m(0) = 0$, leads to $B = 0$. The boundary condition at bottom leads to

$$A\sin(k_{zm}D) = 0,$$

thus

$$k_{zm}D = m\pi, \quad m = 1, 2, \ldots$$

So we obtain the eigenvalues

$$k_{rm} = \sqrt{k^2 - k_{zm}^2}$$

$$= \sqrt{k^2 - \left(\frac{m\pi}{D}\right)^2}, \quad m = 1, 2, \ldots \tag{1.27}$$

The eigenfunctions are

$$\Psi_m(z) = \sqrt{\frac{2\rho}{D}} \sin(k_{zm}z), \tag{1.28}$$

where

$$k_{zm} = \frac{m\pi}{D}, \quad m = 1, 2, \ldots$$

The pressure field is

$$p(r, z) = \frac{i}{4\rho(z_s)} \sum_{m=1}^{\infty} \Psi_m(z_s)\Psi_m(z)H_0^{(1)}(k_{rm}r)$$

$$= \frac{i}{2D} \sum_{m=1}^{\infty} \sin(k_{zm}z_s)\sin(k_{zm}z)H_0^{(1)}(k_{rm}r) \tag{1.29}$$

Number of propagating (in range) modes

The propagating modes have real eigenvalues,

$$k_{rm} = \sqrt{k^2 - k_{zm}^2},$$

so,

$$k_{zm} \leq k,$$

insert in $k_{zm} = m\frac{\pi}{D}$ and $k = \frac{2\pi}{\lambda}$, we have

$$m\frac{\pi}{D} \leq \frac{2\pi}{\lambda},$$

thus, we get the number of propagating modes

$$M = [\frac{2D}{\lambda}]. \tag{1.30}$$

where $[x]$ rounds x to the nearest integer towards infinity.

By comparing the results of these two ideal waveguides (waveguide with a hard bottom or a soft bottom), we find they have the same function forms of eigenfunctions (in k_{zm}) and pressure field, while different eigenvalues k_{rm} and k_{zm}, as well as mode shapes, which is due to the different boundary condition at the bottom.

1.4 Eigenvalue Equation for a Homogeneous Fluid Layer Bounded by Arbitrary Horizontally Stratified Media

Suppose that we have a homogeneous fluid layer bounded above by a horizontally stratified media with plane wave reflection coefficient R_S and below by a horizontally stratified media with plane wave reflection coefficient R_B, as shown in Fig. 1-2. We can determine the eigenvalues by eigenvalue equation.
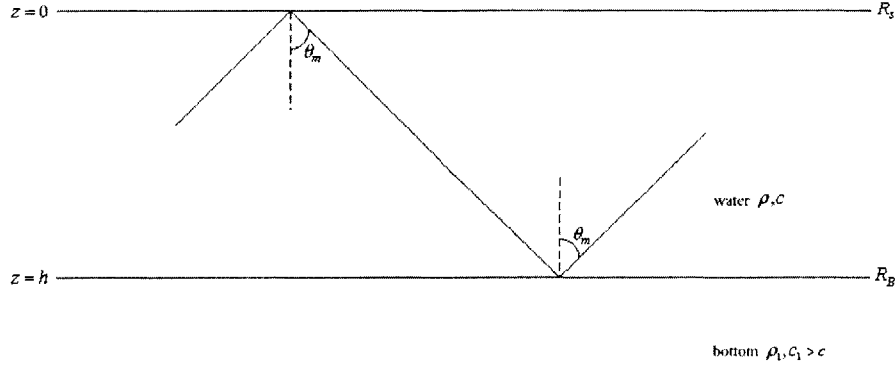
Figure 1-2: Homogeneous fluid layer bounded by arbitrary horizontally stratified media with plane wave reflection coefficients R_S and R_B.

The eigenfunction $\Psi_m(z)$ can be written as the sum of a down-going plane wave $\Psi_{dm}(z)$ and an up-going plane wave $\Psi_{um}(z)$,

$$\Psi_m(z) = \Psi_{dm}(z) + \Psi_{um}(z)$$
$$= A_m e^{ik_{zm}z} + B_m e^{-ik_{zm}z}, \tag{1.31}$$

where A_m, B_m are arbitrary constants to be determined by the boundary conditions (cf. Fig. 1-3).
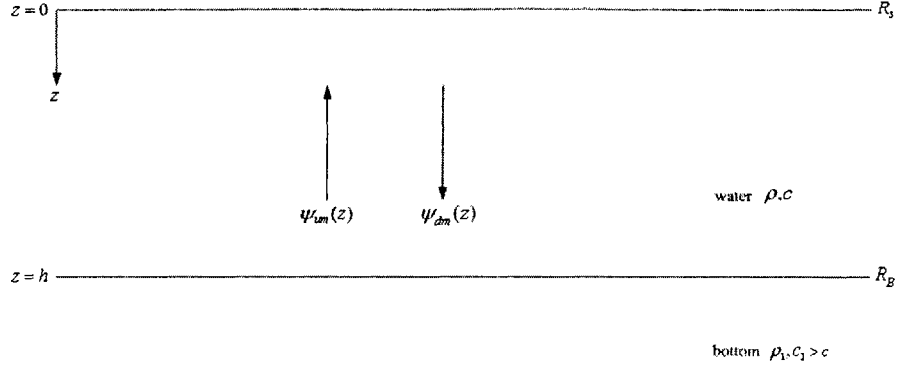
Figure 1-3: Up-going part and down-going part of eigenfunction.

The contribution of mode m to the pressure field is

$$
\begin{aligned}
p_m(r, z) &= a_m \Psi_m(z) \Phi_m(r) \\
&= a_m [\Psi_{um}(z) + \Psi_{dm}(z)] \Phi_m(r) \\
&= p_{um}(r, z) + p_{dm}(r, z),
\end{aligned}
$$

where

$$
p_{um}(r, z) = a_m \Psi_{um}(z) \Phi_m(r),
$$

$$
p_{dm}(r, z) = a_m \Psi_{dm}(z) \Phi_m(r),
$$

thus, with incident angle $\theta_m = \tan^{-1}\left(\frac{k_{rm}}{k_{zm}}\right)$,

$$
\begin{aligned}
R_{Sm} &= \left.\frac{p_{dm}(r, z)}{p_{um}(r, z)}\right|_{z=0} \\
&= \left.\frac{\Psi_{dm}(z)}{\Psi_{um}(z)}\right|_{z=0} \\
&= \frac{A_m}{B_m},
\end{aligned} \tag{1.32}
$$

28

$$
\begin{aligned}
R_{Bm} &= \left. \frac{p_{um}(r,z)}{p_{dm}(r,z)} \right|_{z=h} \\
&= \left. \frac{\Psi_{um}(z)}{\Psi_{dm}(z)} \right|_{z=h} \\
&= \frac{B_m}{A_m} e^{-i2k_{zm}h}.
\end{aligned}
\tag{1.33}
$$

Multiply Eq. (1.32) by Eq. (1.33), we get the eigenvalue equation,

$$
R_{Sm} R_{Bm} = e^{-i2k_{zm}h},
$$

or,

$$
R_{Sm} R_{Bm} e^{i2k_{zm}h} = 1.
\tag{1.34}
$$

From above we see that both R_{Sm} and R_{Bm} correspond to incident angle $\theta_m = \tan^{-1}\left(\frac{k_{rm}}{k_{zm}}\right)$, while not vertically incident $\theta_m = 0$.

If we write R_{Sm} and R_{Bm} as

$$
R_{Sm} = |R_{Sm}|\, e^{i\phi_{Sm}},
$$

$$
R_{Bm} = |R_{Bm}|\, e^{i\phi_{Bm}},
$$

then Eq. (1.34) becomes

$$
|R_{Sm}|\,|R_{Bm}|\, e^{i(2k_{zm}h + \phi_{Sm} + \phi_{Bm})} = 1.
\tag{1.35}
$$

Furthermore, the plane wave reflection coefficient for the case of reflection from a homogeneous fluid half-space is ([11])

$$
R = \frac{m\cos\theta - \sqrt{n^2 - \sin^2\theta}}{m\cos\theta + \sqrt{n^2 - \sin^2\theta}},
$$

where θ is the incident angle, $m = \frac{\rho_1}{\rho}$, $n = \frac{k_1}{k} = \frac{c}{c_1}$, and n is called the index of refraction.

29

Now let us use the eigenvalue equation to find the eigenvalues for ideal waveguides.

1. A homogeneous fluid layer with a soft top and a hard bottom

   Soft top is characterized by $R_S = -1 = e^{-i\pi}$, and hard bottom is characterized by $R_B = 1$, thus the eigenvalue equation (1.35) gives

   $$e^{i(2k_z h - \pi)} = 1,$$

   and therefore

   $$2k_{zm}h - \pi = 2(m-1)\pi, \quad m = 1, 2, \cdots$$

   so we obtain

   $$k_{zm} = (m - \frac{1}{2})\frac{\pi}{h}, \quad m = 1, 2, \cdots$$

   and

   $$k_{rm} = \sqrt{k^2 - k_{zm}^2}.$$

2. A homogeneous fluid layer with a soft top and a soft bottom

   In this case, $R_S = -1 = e^{-i\pi}$ and $R_B = -1 = e^{-i\pi}$, the eigenvalue equation (1.35) gives

   $$e^{i(2k_{zm}h - \pi - \pi)} = 1,$$

   which leads to

   $$2k_{zm}h - 2\pi = 2(m-1)\pi, \quad m = 1, 2, \cdots$$

   so we obtain

   $$k_{zm} = m\frac{\pi}{h}, \quad m = 1, 2, \cdots$$

   and

   $$k_{rm} = \sqrt{k^2 - k_{zm}^2}.$$

1.5 Normal Modes for the Pekeris Waveguide

The Pekeris waveguide consists of a homogeneous fluid layer with a pressure-release top and a homogeneous, higher velocity halfspace bottom (cf. Fig. 1-4). The Pekeris waveguide is of particular interest in ocean acoustics because it embodies many of the fundamental features of acoustic propagation in shallow water.

Pressure-release surface

$z = 0$ ———————————————————————————————————— $p = 0$

water ρ, c

$z = h$ ——————————————————————————————

bottom $\rho_1, c_1 > c$
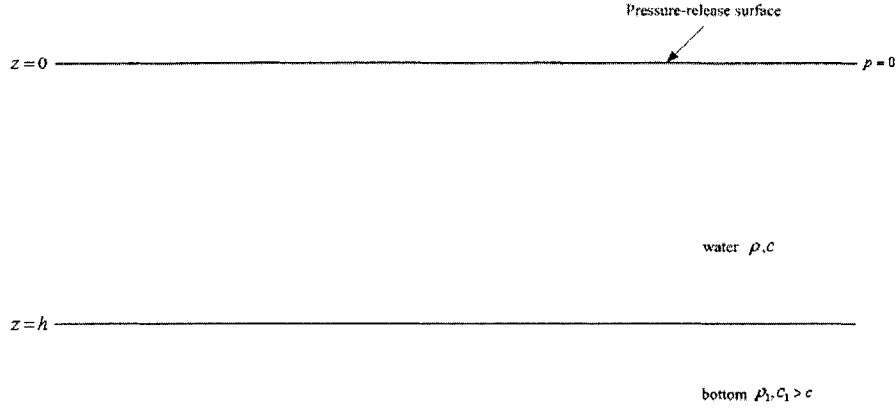
Figure 1-4: Pekeris waveguide.

From section 1.3 we have known that, when the waveguide has impenetrable boundaries, the solution consists totally of a sum of discrete sums. In this section, we will see that for the Pekeris waveguide, which has one penetrable boundary, the solution consists of both discrete and continuum sets due to the total internal reflection.

The top of the Pekeris waveguide is a pressure-release surface, which is characterized by $R_s = -1 = e^{-i\pi}$, and the plane wave reflection coefficient at the bottom is

$$R_{Bm} = \frac{m \cos \theta_m - \sqrt{n^2 - \sin^2 \theta_m}}{m \cos \theta_m + \sqrt{n^2 - \sin^2 \theta_m}}.$$

For angles of incidence $\theta_m < \theta_c$, where θ_c is the critical angle corresponding to total internal reflection,

$$\sin \theta_c = \frac{c}{c_1} = n,$$

31

we have $\sin\theta_m < n$, and

$$|R_{Bm}| = \frac{m\cos\theta_m - \sqrt{n^2 - \sin^2\theta_m}}{m\cos\theta_m + \sqrt{n^2 - \sin^2\theta_m}},$$

$$\phi_{Bm} = 0,$$

so, the eigenvalue equation (1.35) gives

$$|R_{Bm}|\,e^{i(2k_{zm}h - \pi)} = 1.$$

Since $|R_{Bm}| < 1$ for $\theta_m < \theta_c$, so k_{zm} must be complex, violating the condition that eigenvalues are real for a proper Sturm-Liouville problem. Thus, $\theta_m < \theta_c$ corresponds to an improper Sturm-Liouville problem.

However, for angles of incidence $\theta_m \geq \theta_c$, since $\sin\theta_c = n$, we have $\sin\theta_m \geq n$, thus

$$R_{Bm} = \frac{m\cos\theta_m - i\sqrt{\sin^2\theta_m - n^2}}{m\cos\theta_m + i\sqrt{\sin^2\theta_m - n^2}},$$

so,

$$|R_{Bm}| = 1,$$

and

$$\phi_{Bm} = -2\tan^{-1}\left[\frac{\sqrt{\sin^2\theta_m - n^2}}{m\cos\theta_m}\right],$$

so, the eigenvalue equation (1.35) gives

$$e^{i(2k_{zm}h - \pi + \phi_{Bm})} = 1, \tag{1.36}$$

which implies that k_{zm} are real and associate with a proper Sturm-Liouville problem.

Thus we can see, for plane wave reflection from a higher velocity half-space, the critical angle θ_c delineates two distinct regimes (cf. Fig. 1-5):

1. For angle of incidence $\theta \geq \theta_c$, due to total internal reflection, the reflection coefficient has magnitude $|R_B| = 1$, corresponding to a proper Sturm-Liouville problem, and discrete modes (trapped modes, proper modes).

32
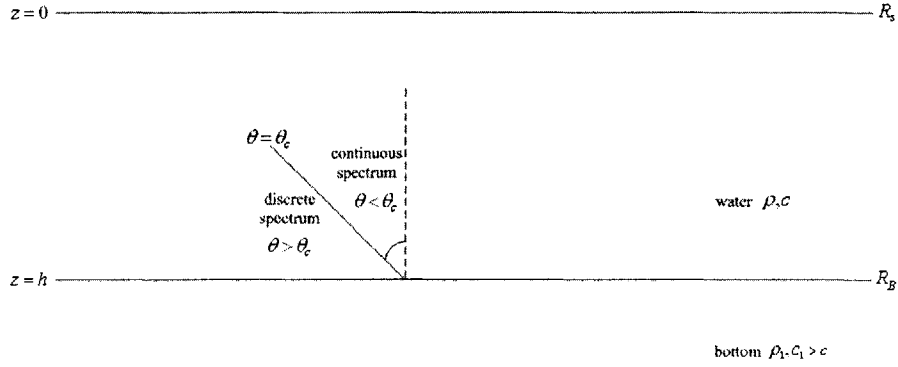
Figure 1-5: Angular regions for the discrete modes and continuous modes.

2. For angles of incidence $\theta < \theta_c$, we have $|R_B| < 1$, corresponding to an improper Sturm-Liouville problem, and continuous modes(leaky modes, improper modes).

The total field is the superposition of the fields for these two angular regimes,

$$p(r, z) = p_t(r, z) + p_c(r, z),$$

where $p(r, z)$ is the total field, $p_t(r, z)$ and $p_c(r, z)$ are the contribution of the trapped and continuous modes, respectively.

1.5.1 Proper Modes of the Pekeris Waveguide

Eigenvalue equation for the proper modes

For $\theta_m \geq \theta_c$, we have

$$e^{i(2k_{zm}h - \pi + \phi_{Bm})} = 1,$$

where

$$\phi_{Bm} = -2\tan^{-1}\left(\frac{\sqrt{\sin^2\theta_m - n^2}}{m\cos\theta_m}\right), \tag{1.37}$$

thus we have

$$2k_{zm}h - \pi + \phi_{Bm} = 2(m-1)\pi, \quad m = 1, 2, \cdots$$

33

and therefore we obtain the eigenvalue equation,

$$k_{zm} = \frac{1}{h}\left[(m - \frac{1}{2})\pi - \frac{1}{2}\phi_{Bm}\right],$$
(1.38)

and

$$k_{rm} = \sqrt{k^2 - k_{zm}^2},$$

where ϕ_{Bm} is given by Eq. (1.37).

Eigenfunction of proper modes

For the modes that are perfected trapped in the Pekeris waveguide, the eigenfunction can be determined as below (cf. Fig. 1-6):
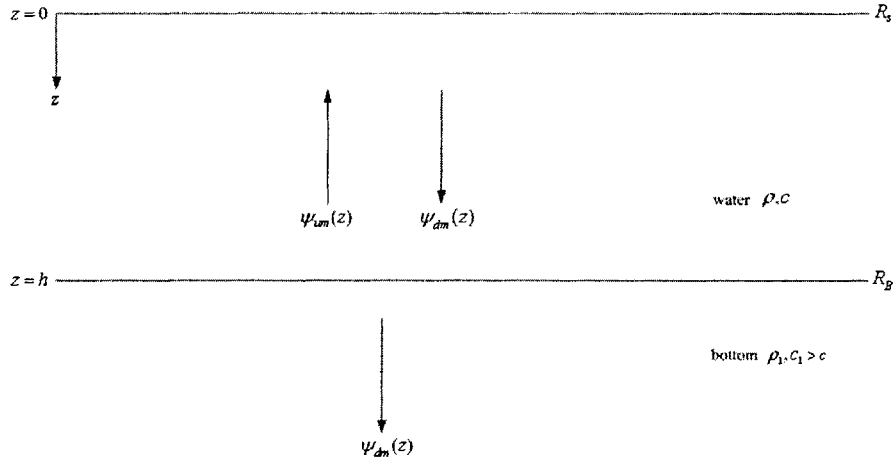
Figure 1-6: Eigenfunctions in water and bottom.

For $0 \leq z \leq h$,

$$\Psi_m(z) = \Psi_{dm}(z) + \Psi_{um}(z)$$
$$= a_m e^{ik_{zm}z} + b_m e^{-ik_{zm}z},$$
(1.39)

where a_m, b_m are arbitrary constants to be determined by boundary conditions.

For pressure-release surface, we have

$$\Psi_m(0) = 0,$$

so, Eq. (1.39) gives

$$a_m + b_m = 0 \implies b_m = -a_m,$$

thus, in the water, we have

$$\Psi_m(z) = a_m(e^{ik_{zm}z} - e^{-ik_{zm}z})$$

$$= 2ia_m \sin(k_{zm}z)$$

$$= A_m \sin(k_{zm}z).$$

For $z > h$,

$$\Psi_m(z) = B_m e^{ik_{1zm}z},$$

since $k_{1zm} = \sqrt{k_1^2 - k_{rm}^2}$, and $k_1 < k_{rm}$ for discrete modes, so, $k_{1zm} = i\sqrt{k_{rm}^2 - k_1^2}$, and

$$\Psi_m(z) = B_m e^{-\sqrt{k_{rm}^2 - k_1^2}z} = B_m e^{-\gamma_m z},$$

where $\gamma_m = \sqrt{k_{rm}^2 - k_1^2}$.

Thus, the eigenfunctions can be written as:

$$\Psi_m(z) = \begin{cases} A_m \sin(k_{zm}z), & 0 \le z \le h \\ B_m e^{-\gamma_m z}, & z > h \end{cases} \tag{1.40}$$

With orthonormal property of $\Psi_m(z)$, we can show that (See Appendix A)

$$A_m = \sqrt{2} \left[\frac{1}{\rho} \left(h - \frac{\sin(2k_{zm}h)}{2k_{zm}} \right) + \frac{1}{\rho_1} \frac{\sin^2(k_{zm}h)}{\gamma_m} \right]^{-\frac{1}{2}}, \tag{1.41}$$

$$B_m = A_m \sin(k_{zm}h)e^{\gamma_m h}. \tag{1.42}$$

Thus, with Eq. (1.40), Eq. (1.41), and Eq. (1.42), we can calculate the eigenfunction of the discrete modes. In Fig. 1-7, we show the first four eigenfunctions (calculated by C-SNAP with input file listed in Appendix B).

From Fig. 1-7 we can see the fact that the rate of exponential decay in the bottom decreases with increasing mode number for trapped modes. This is because the

35
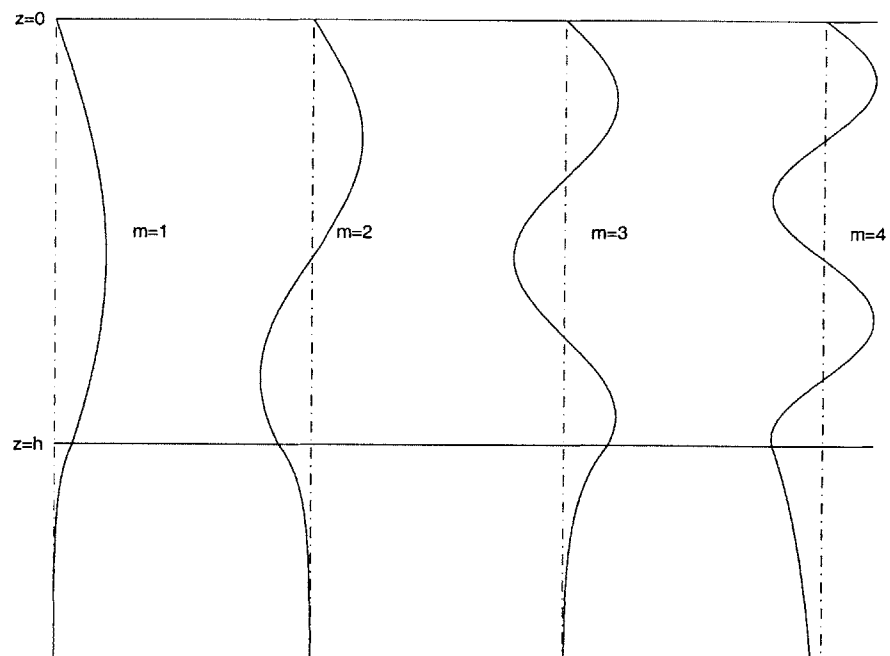
Figure 1-7: Eigenfunctions of the first 4 modes of the Pekeris waveguide with $c = 1500$ m/s, $\rho = 1.0$ g/cm^3, $c_1 = 1800$ m/s, $\rho = 1.5$ g/cm^3, no absorption, at frequency $= 50$ Hz.

decaying rate of mode m, i.e., $\gamma_m = \sqrt{k_{rm}^2 - k_1^2}$, decreases with increasing mode number for trapped modes ($k_{rm} > k_1$). As mode number continues increasing, the oscillatory behavior takes the place of the exponential decay, which corresponds to the leaky modes (cf. Fig. 1-8).

leaky modes   trapped modes

k_{r4} k_{r3} k_{r2} k_{r1} wavenumber

$k_1 = \dfrac{\omega}{c_1} < k$ k
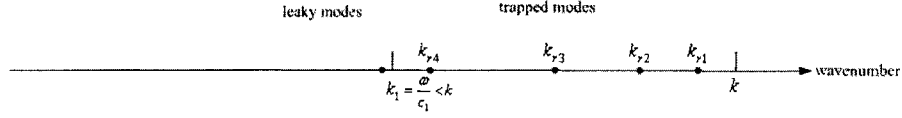
Figure 1-8: Illustration of locations of eigenvalues and wavenumbers in water and in bottom.

From Fig. 1-8 it is clear that:

1. For trapped modes, the eigenvalue $k_{rm} > k_1$, so $k_{1zm} = \sqrt{k_1^2 - k_{rm}^2} = i\sqrt{k_{rm}^2 - k_1^2} = i\gamma_m$, and thus $e^{ik_{1zm}z} = e^{-\gamma_m z}$, i.e., the wave decays exponentially in z direction for $z > h$, so the energy is trapped in water layer.

2. For leaky modes, the eigenvalue $k_{rm} < k_1$, so $k_{1zm} = \sqrt{k_1^2 - k_{rm}^2}$, and thus $e^{ik_{1zm}z}$ is oscillatory, which means the energy leaks into the bottom.

Pressure-field of trapped modes

Having found the eigenfunctions, we can calculate the pressure-field contributed by the trapped modes by

$$p_t(r, z) = \frac{i}{4\rho(z_s)} \sum_{m=1}^{M_t} \Psi_m(z_s)\Psi_m(z)H_0^{(1)}(k_{rm}r)$$

where M_t is the maximum number of the trapped modes.

Determine the number of the trapped modes M_t

According to Fig. 1-5, the trapped modes are in the region $\theta_m \geq \theta_c$, so we have

$$\sin\theta_m \geq \sin\theta_c, \tag{1.43}$$

recall that

$$\sin\theta_c = \frac{c}{c_1},$$

37

and

$$\sin \theta_m = \frac{k_{rm}}{k},$$

so Eq. (1.43) leads to

$$\frac{k_{rm}}{k} \geq \frac{c}{c_1},$$

i.e.,

$$\frac{k^2 - k_{zm}^2}{k^2} \geq \frac{c^2}{c_1^2},$$

so,

$$\frac{k_{zm}}{k} \leq \sqrt{1 - \frac{c^2}{c_1^2}}, \qquad (1.44)$$

insert in eigenvalue equation, Eq. (1.38), we get

$$\frac{1}{h} \left[(m - \frac{1}{2})\pi - \frac{\phi_{Bm}}{2} \right] \leq \frac{2\pi}{\lambda} \sqrt{1 - \frac{c^2}{c_1^2}},$$

which leads to

$$m \leq \frac{1}{2} + \frac{\phi_{Bm}}{2\pi} + \frac{2h}{\lambda} \sqrt{1 - \frac{c^2}{c_1^2}}$$

$$- \pi \leq \phi_{Bm} \leq 0$$

$$\leq \frac{1}{2} + \frac{2h}{\lambda} \sqrt{1 - \frac{c^2}{c_1^2}}, \qquad (1.45)$$

thus we obtain

$$M_t = \left[\frac{1}{2} + \frac{2h}{\lambda} \sqrt{1 - \frac{c^2}{c_1^2}} \right], \qquad (1.46)$$

where $[x]$ rounds x to the nearest integer towards infinity.

From Eq. (1.46), we can see as $c_1 \to \infty$, M_t reduces to the number of propagating modes with hard bottom, i.e., Eq. (1.23)

For a given ratio $\frac{h}{\lambda}$, the number of trapped modes in the Pekeris waveguide is smaller than the number of propagating modes in the wageguide with hard bottom because of the more constrained angular regime for perfect reflection in the Pekeris

38

waveguide.

1.5.2 Improper Modes of the Pekeris Waveguide

We have known that $\theta_m < \theta_c$ corresponds to an improper Sturm-Liouville problem. In order to evaluate the contribution of the modal continuum to the field in the Pekeris waveguide, we introduce a hard boundary at a finite distance from the surface(cf. Fig 1-9). We solve the related proper Sturm-Liouville problem shown in Fig. 1-9 and examine the limit of the solution as the thickness of the lower layer becomes infinite ($H \rightarrow \infty$). We will thereby arrive at the solution of the original, improper posed Sturm-Liouville problem.
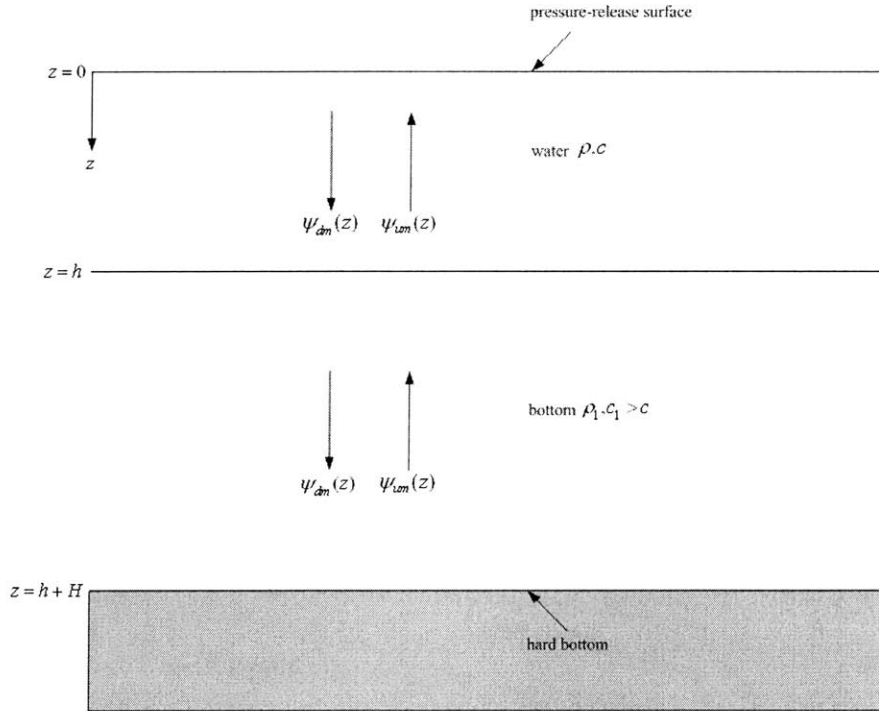
Figure 1-9: The proper Sturm-Liouville problem which, in the limit of infinite H, leads to the solution of the improper Sturm-Liouville problem shown in Fig. 1-4.

39

The eigenfunction for the configuration in Fig. 1-9 is (See Appendix C):

$$\Psi_m(z) = \begin{cases} A_m \sin(k_{zm}z), & 0 \le z \le h \\ B_m e^{ik_{1zm}(h+H)} \cos k_{1zm}[z - (h+H)], & h \le z \le h+H \end{cases} \tag{1.47}$$

where

$$B_m = A_m \frac{\sin(k_{zm}h)}{\cos(k_{1zm}H)} e^{-ik_{1zm}(h+H)},$$

$$A_m = \left[\frac{1}{\rho}(\frac{h}{2} - \frac{\sin(2k_{zm}h)}{4k_{zm}}) + \frac{1}{\rho_1} \frac{\sin^2(k_{zm}h)}{\cos^2(k_{1zm}H)}(\frac{H}{2} + \frac{1}{4k_{1zm}} \sin 2k_{1zm}H) \right]^{-\frac{1}{2}}.$$

The eigenvalue equation is (See Appendix C):

$$\tan(k_{zm}h) \tan(k_{1zm}H) = \frac{\rho_1 k_{zm}}{\rho k_{1zm}}. \tag{1.48}$$

In the limit $\rho_1 \to \rho$, $c_1 \to c$, we have $k_1 = k$ and $k_{1zm} = k_{zm} = \sqrt{k_1^2 - k_{rm}^2} = \sqrt{k^2 - k_{rm}^2}$, the eigenvalue equation (1.48) is therefore

$$\tan(k_{zm}h) \tan(k_{zm}H) = 1, \tag{1.49}$$

which leads to

$$\cos(k_{zm}h) \cos(k_{zm}H) - \sin(k_{zm}h) \sin(k_{zm}H) = 0,$$

i.e.,

$$\cos k_{zm}(h + H) = 0,$$

thus,

$$k_{zm}(h + H) = (m - \frac{1}{2})\pi, \quad m = 1, 2, \ldots \tag{1.50}$$

or

$$k_{zm} = (m - \frac{1}{2})\frac{\pi}{h + H}, \quad m = 1, 2, \ldots$$

40

We see this result is the same as the eigenvalue equation in the ideal waveguide with hard bottom at depth $(h + H)$.

With Eq. (1.49) and Eq. (1.50), we can simplify the eigenfunction (1.47) for $\rho_1 \rightarrow \rho$, $c_1 \rightarrow c$.

$$A_m = \left[\frac{1}{\rho} \left(\frac{h}{2} - \frac{\sin 2k_{zm}h}{4k_{zm}} \right) + \frac{1}{\rho_1} \frac{\sin^2(k_{zm}h)}{\cos^2(k_{zm}H)} \left(\frac{H}{2} + \frac{\sin 2k_{zm}H}{4k_{zm}} \right) \right]^{-\frac{1}{2}}, \qquad (1.51)$$

since

$$\frac{\sin^2 k_{zm}h}{\cos^2 k_{zm}H} = \frac{1 - \cos 2k_{zm}h}{1 + \cos 2k_{zm}H}$$

$$\text{insert in } k_{zm} = (m - \tfrac{1}{2})\frac{\pi}{h+H}$$

$$= \frac{1 - \cos(2m-1)\pi \frac{h}{h+H}}{1 + \cos(2m-1)\pi \frac{H}{h+H}}$$

$$= \frac{1 - \cos(2m-1)\pi (1 - \frac{H}{h+H})}{1 + \cos(2m-1)\pi \frac{H}{h+H}}$$

$$= \frac{1 + \cos(2m-1)\pi \frac{H}{h+H}}{1 + \cos(2m-1)\pi \frac{H}{h+H}}$$

$$= 1,$$

and

$$\sin 2k_{zm}H = \sin 2 \left[(m - \frac{1}{2})\frac{\pi}{h+H} \right] H$$

$$= \sin(2m-1)\pi \frac{H}{h+H}$$

$$= \sin \left[(2m-1)\pi (1 - \frac{h}{h+H}) \right]$$

$$= \sin 2k_{zm}h,$$

41

so we have

$$A_m = \left[\frac{h}{2\rho} - \frac{1}{\rho}\frac{\sin 2k_{zm}h}{4k_{zm}} + \frac{1}{\rho}\frac{H}{2} + \frac{1}{\rho}\frac{\sin 2k_{zm}h}{4k_{zm}} \right]^{-\frac{1}{2}}$$

$$= \sqrt{\frac{2\rho}{h+H}},$$

thus for $0 \leq z \leq h$, we have

$$\Psi_m(z) = A_m \sin(k_{zm}z)$$

$$= \sqrt{\frac{2\rho}{h+H}} \sin(k_{zm}z),$$

and

$$B_m = A_m \frac{\sin(k_{zm}h)}{\cos(k_{1zm}H)} e^{-ik_{1zm}(h+H)} \tag{1.52}$$

$$= \sqrt{\frac{2\rho}{h+H}} \frac{\sin(k_{zm}h)}{\cos(k_{zm}H)} e^{-ik_{zm}(h+H)},$$

thus for $h \leq z \leq h + H$, we have

$$\Psi_m(z) = B_m e^{ik_{1zm}(h+H)} \cos k_{1zm}[z - (h + H)]$$

$$= \sqrt{\frac{2\rho}{h+H}} \frac{\sin(k_{zm}h)}{\cos(k_{zm}H)} e^{-ik_{zm}(h+H)} e^{ik_{zm}(h+H)} \cos k_{zm}[z - (h + H)]$$

$$\text{insert in } k_{zm} = (m - \tfrac{1}{2})\frac{\pi}{h+H}$$

$$= \sqrt{\frac{2\rho}{h+H}} \sin(k_{zm}z).$$

Thus we can see the eigenfunction Eq. (1.47) takes a unique form,

$$\Psi_m(z) = \sqrt{\frac{2\rho}{h+H}} \sin(k_{zm}z), \quad \text{for } 0 \leq z \leq h + H,$$

as $\rho_1 \to \rho$, $c_1 \to c$. This result is the same as that of the ideal waveguide with hard bottom at depth $(h + H)$.

Having obtained the eigenvalues and the eigenfunctions, we can write the normal

42

mode solution for this proper Sturm-Liouville problem,

$$p(r, z) = \frac{i}{4\rho(z_s)} \sum_m \Psi_m(z_s)\Psi_m(z)H_0^{(1)}(k_{rm}r). \tag{1.53}$$

For $H \gg h$, it can be shown ([11, p. 157]) that the sum in Eq. (1.53) becomes an integral, and the final result for the modal continuum $p_c(r, z)$ has the form (when both the source and the receiver are in water)([11, p. 157]):

$$p_c(r, z) \approx \frac{i\rho_1}{2\pi\rho} \int_{C_B} \frac{k_z}{k_{1z}} \frac{\sin k_z z_s \sin k_z z}{\left[\sin^2 k_z h + \frac{\rho_1^2 k_z^2}{\rho^2 k_{1z}^2} \cos^2 k_z h\right]} H_0^{(1)}(k_r r)\mathrm{d}k_z, \tag{1.54}$$

where the path of integration C_B is shown in Fig. 1-10.
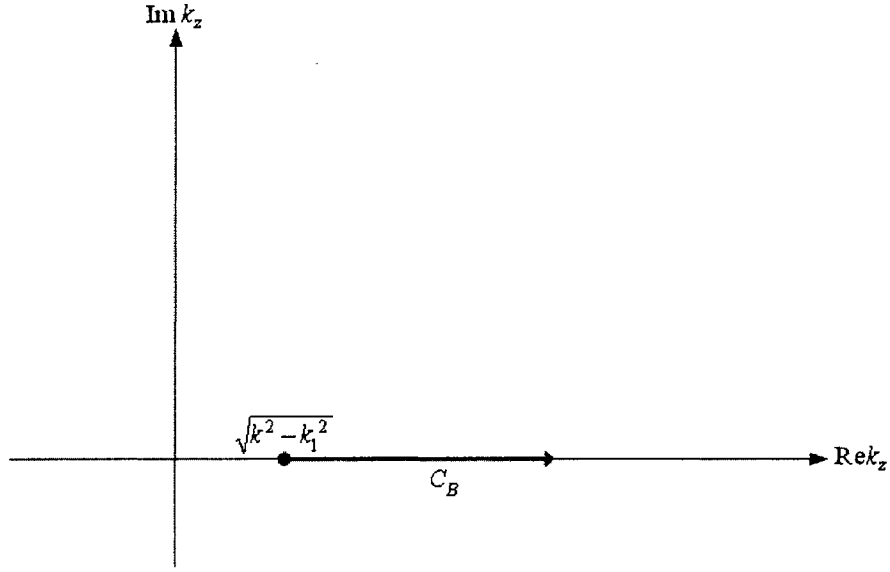
Figure 1-10: Path of integration C_B in the complex k_z-plane associated with the modal continuum part of the solution to the problem shown in Fig. 1-4.

A leaky mode decomposition

The continuum field in Eq. (1.54) can be decomposed into leaky modes, with the eigenvalue equation (See Appendix D)

$$\cot k_{zm}h = i\frac{\rho k_{1zm}}{\rho_1 k_{zm}}, \tag{1.55}$$

and the final result for the continuum field by leaky modes is (See [11, p. 162])

$$p_c(r,z) \sim \sqrt{\frac{2}{\pi}} \frac{1}{2h} e^{i\frac{\pi}{4}} \sum_{m=M_t+1}^{\infty} \sin k_{zm}^{(0)} z_s \sin k_{zm}^{(0)} z e^{-\frac{\rho k_{1zm}^{(0)}}{\rho_1 h k_m^{(0)}} r} \frac{e^{ik_m^{(0)} r}}{\sqrt{k_m^{(0)} r}}, \tag{1.56}$$

where

$$k_{zm}^{(0)} = \frac{(m - \frac{1}{2})\pi}{h}, \quad m = 1, 2, \ldots$$

$$k_m^{(0)} = \sqrt{k^2 - k_{zm}^{(0)2}},$$

$$k_{1zm}^{(0)} = \sqrt{k_1^2 - k_m^{(0)2}} = \sqrt{k_1^2 - k^2 + k_{zm}^{(0)2}}.$$

From Eq. (1.56) we can see the exponentially decaying term $e^{-\frac{\rho k_{1zm}^{(0)}}{\rho_1 h k_m^{(0)}} r}$, so as the leaky modes propagate along the waveguide, they lose energy into the bottom.

1.5.3   The Total Field in the Pekeris Waveguide

The total field in the Pekeris waveguide is composed of discrete and continuum modal contributions,

$$p(r,z) = p_t(r,z) + p_c(r,z).$$

With increasing range, the trapped modes tend to dominate the total field because of the exponentially decaying factor in the leaky mode field.

A general derivation can be found in Chapter 4 in [14].

1.6   A Line Source in a Horizontally Stratified Fluid Medium in Plane Geometry

The Helmholtz equation for a line source in a horizontally stratified fluid media (cf. Fig 1-11) is ([14, p. 275])

$$\frac{\partial^2 p}{\partial x^2} + \rho(z)\frac{\partial}{\partial z}\left(\frac{1}{\rho(z)}\frac{\partial p}{\partial z}\right) + \frac{\omega^2}{c^2(z)}p = -\delta(x)\delta(z - z_s). \tag{1.57}$$

44
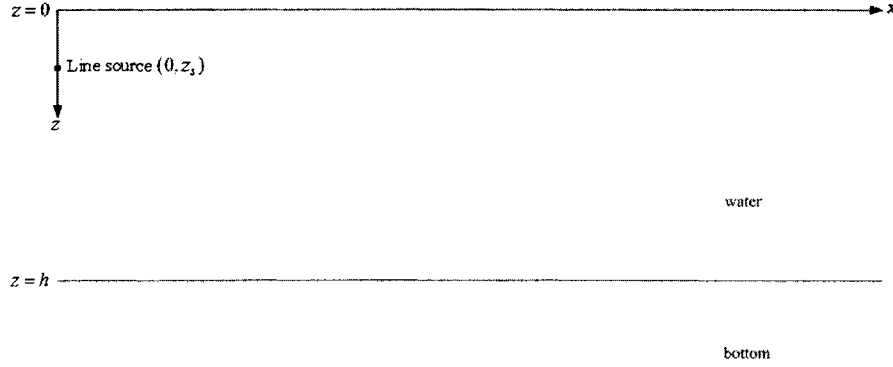
Figure 1-11: A line source located at $(x, z) = (0, z_s)$ in a horizontally stratified fluid media (plane geometry).

We seek a solution in the form

$$p(x, z) = \sum_m \Phi_m(x)\Psi_m(z), \tag{1.58}$$

where $\Psi_m(z)$ are eigenfunctions of the depth-separated equation

$$\rho(z)\frac{\mathrm{d}}{\mathrm{d}z}\left[\frac{1}{\rho(z)}\frac{\mathrm{d}\Psi_m(z)}{\mathrm{d}z}\right] + \left[\frac{\omega^2}{c^2(z)} - k_{xm}^2\right]\Psi_m(z) = 0, \tag{1.59}$$

Insert Eq. (1.58) and Eq. (1.59) into Eq. (1.57), we obtain

$$\sum_m \left[\frac{\mathrm{d}^2\Phi_m(x)}{\mathrm{d}x^2}\Psi_m(z) + k_{xm}^2\Phi_m(x)\Psi_m(z)\right] = -\delta(x)\delta(z - z_s), \tag{1.60}$$

apply the operator $\int_0^\infty (\cdot)\frac{1}{\rho(z)}\Psi_n(z)\mathrm{d}z$ to Eq. (1.60), we obtain the equation for $\Phi_n(x)$,

$$\frac{\mathrm{d}^2\Phi_n(x)}{\mathrm{d}x^2} + k_{xn}^2\Phi_n(x) = -\frac{\delta(x)\Psi_n(z_s)}{\rho(z_s)}. \tag{1.61}$$

We can solve ODE (1.61) by the endpoint method (See Appendix E), and obtain the solution

$$\Phi_n(x) = \frac{i}{2\rho(z_s)}\Psi_n(z_s)\frac{e^{ik_{xn}|x|}}{k_{xn}}. \tag{1.62}$$

45

Thus we obtain the final solution of Eq. (1.57),

$$p(x, z) = \frac{i}{2\rho(z_s)} \sum_m \Psi_m(z_s) \Psi_m(z) \frac{e^{ik_{xm}|x|}}{k_{xm}}. \tag{1.63}$$

1.7 Transmission Loss

1.7.1 Definition

In underwater acoustics, the field is traditionally expressed in terms of transmission loss, defined as

$$\mathrm{TL}(\boldsymbol{r}, \boldsymbol{r_s}) = -20 \log_{10} \left| \frac{p(\boldsymbol{r}, \boldsymbol{r_s})}{p_0(1)} \right|, \tag{1.64}$$

where $\boldsymbol{r}$ is the location of the field point, $\boldsymbol{r_s}$ is the location of the source, $p_0(1)$ is the pressure produced at a distance of $1m$ from the same source in an infinite, homogeneous medium with sound speed $c(\boldsymbol{r_s})$ and density $\rho(\boldsymbol{r_s})$.

1.7.2 $p_0(1)$ of a Point Source and a Line Source

1. $p_0(r)$ of a point source

   For a point source in an infinite, homogeneous medium,

   $$p_0(r) = \frac{e^{ik_0 r}}{4\pi r}, \tag{1.65}$$

   where $k_0 = \frac{\omega}{c_0}$ is the wavenumber at the source depth. So,

   $$|p_0(1)| = \frac{1}{4\pi}.$$

2. $p_0(r)$ of a line source

   For a line source in an infinite, homogeneous medium, $p_0(r)$ satisfies([14, p. 276])

   $$\frac{1}{r} \frac{\mathrm{d}}{\mathrm{d}r}(r \frac{\mathrm{d}p_0(r)}{\mathrm{d}r}) + k_0^2 p_0(r) = -\frac{\delta(r)}{r}. \tag{1.66}$$

46

The solution of Eq. (1.66) is

$$p_0(r) = \frac{i}{4} H_0^{(1)}(k_0 r),$$

where $k_0 = \frac{\omega}{c_0}$ is the wavenumber at the source depth.

Thus, we have

$$|p_0(1)| = \frac{1}{4} H_0^{(1)}(k_0).$$

1.7.3 Coherent and Incoherent Transmission Loss ([14, p. 274])

If we represent the field as $p(r, z) = \sum_m \Phi_m(r) \Psi_m(z)$, then

- Coherent transmission loss

$$\text{TL}_{\text{coh}}(r, z) = -20 \log_{10} \left[\frac{1}{|p_0(1)|} \left| \sum_m \Phi_m(r) \Psi_m(z) \right| \right],$$

- Incoherent transmission loss

$$\text{TL}_{\text{inc}}(r, z) = -20 \log_{10} \left[\frac{1}{|p_0(1)|} \sqrt{\sum_m |\Phi_m(r) \Psi_m(z)|^2} \right].$$

For example, for a point source case, in the far field, we have

$$\Phi_m(r) = \frac{i}{\rho(z_s)\sqrt{8\pi r}} \Psi_m(z_s) \frac{e^{ik_{rm} r}}{\sqrt{k_{rm}}},$$

and

$$|p_0(1)| = \frac{1}{4\pi},$$

thus,

$$
\begin{aligned}
\mathrm{TL_{coh}}(r, z) &= -20 \log_{10} \left[\frac{1}{|p_0(1)|} \left| \sum_m \Phi_m(r) \Psi_m(z) \right| \right] \\
&= -20 \log_{10} \left[\frac{4\pi}{\rho(z_s)\sqrt{8\pi r}} \left| \sum_m \Psi_m(z_s) \Psi_m(z) \frac{e^{ik_{rm}r}}{\sqrt{k_{rm}}} \right| \right] \\
&= -20 \log_{10} \left[\frac{1}{\rho(z_s)} \sqrt{\frac{2\pi}{r}} \left| \sum_m \Psi_m(z_s) \Psi_m(z) \frac{e^{ik_{rm}r}}{\sqrt{k_{rm}}} \right| \right],
\end{aligned}
\tag{1.67}
$$

and

$$
\begin{aligned}
\mathrm{TL_{inc}} &= -20 \log_{10} \left[\frac{1}{|p_0(1)|} \sqrt{\sum_m |\Phi_m(r) \Psi_m(z)|^2} \right] \\
&= -20 \log_{10} \left[\frac{4\pi}{\rho(z_s)\sqrt{8\pi r}} \sqrt{\sum_m \left| \Psi_m(z_s) \Psi_m(z) \frac{e^{ik_{rm}r}}{\sqrt{k_{rm}}} \right|^2} \right] \\
&= -20 \log_{10} \left[\frac{1}{\rho(z_s)} \sqrt{\frac{2\pi}{r}} \sqrt{\sum_m \left| \Psi_m(z_s) \Psi_m(z) \frac{e^{ik_{rm}r}}{\sqrt{k_{rm}}} \right|^2} \right].
\end{aligned}
\tag{1.68}
$$

Note that we can not drop off the term $e^{ik_{rm}r}$ in Eq. (1.68) because k_{rm} is complex.

The incoherent transmission sums up the modes with a uniformly distributed random phase, so it is particularly useful when the detailed interference structure presented by the coherent summation of modes is not physically meaningful and a smoothed result is preferred. For example, for shallow-water problems, where the modes are bottom-interacting, since the bottom properties are usually poorly known, the interference pattern predicted by a coherent transmission loss is not always physically meaningful. In this case, incoherent transmission loss is appropriate.

Chapter 2

Two-Dimensional Coupled Modes in a Two-Dimensional Waveguide

In Chapter 1, we presented the normal modes solutions to the range-independent problems. In this chapter, we will extend them to range-dependent problems.

In this chapter, we first develop the two-way coupled modes model, followed by a description about the decoupling of stepwise coupled modes algorithm (COUPLE) by Evans[8]) . Then we explore two simplifications, i.e., single-scattering approximation and one-way coupled modes model. Next, we show how to modify C-SNAP to an approximate two-way model. In the last section of this chapter, we will present some numerical examples.

2.1   Coupled Modes Method

Following the derivation by Evans([8]), we begin by dividing the range axis into a number of segment (cf. Fig. 2-1), and approximate the field as range-independent in each segment. The interface conditions are used to "glue" the normal modes solutions in each segment together.

If we neglect the continuous spectrum, the solution in segment j can be represented

49
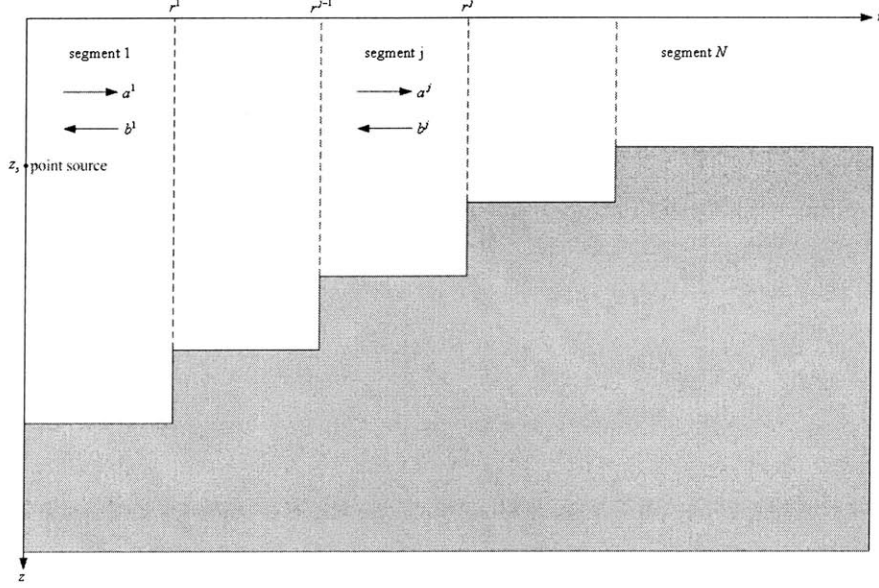
Figure 2-1: Range-segmentation for coupled-modes formulation.

as([14])

$$p^j(r, z) = \sum_{m=1}^{M} [a_m^j \hat{H}1_m^j(r) + b_m^j \hat{H}2_m^j(r)]\Psi_m^j(z), \qquad (2.1)$$

where $r^{j-1} < r < r^j$, and

$$\hat{H}1_m^j(r) = \frac{H_0^{(1)}(k_{rm}^j r)}{H_0^{(1)}(k_{rm}^j r^{j-1})},$$

$$\hat{H}2_m^j(r) = \frac{H_0^{(2)}(k_{rm}^j r)}{H_0^{(2)}(k_{rm}^j r^{j-1})},$$

are Hankel functions of order zero, types one and two that are normalized at $r = r^{j-1}$. The case $j = 1$ is special with $r^{j-1} = r^1$, k_{rm}^j are horizontal wavenumbers (eigenvalues) in segment j, $\Psi_m^j(z)$ are eigenfunctions in segment j.

For $k_{rm}^j r \gg 1$, we use the asymptotic representation of Hankel functions,

$$H_0^{(1)}(k_{rm}^j r) \approx \sqrt{\frac{2}{\pi k_{rm}^j r}} e^{i(k_{rm}^j r - \frac{\pi}{4})},$$

$$H_0^{(2)}(k_{rm}^j r) \approx \sqrt{\frac{2}{\pi k_{rm}^j r}} e^{-i(k_{rm}^j r - \frac{\pi}{4})},$$

50

so we get

$$\hat{H}1_m^j(r) = \frac{H_0^{(1)}(k_{rm}^j r)}{H_0^{(1)}(k_{rm}^j r^{j-1})} \approx \sqrt{\frac{r^{j-1}}{r}} e^{ik_{rm}^j(r-r^{j-1})} \equiv H1_m^j(r), \qquad (2.2)$$

$$\hat{H}2_m^j(r) = \frac{H_0^{(2)}(k_{rm}^j r)}{H_0^{(2)}(k_{rm}^j r^{j-1})} \approx \sqrt{\frac{r^{j-1}}{r}} e^{-ik_{rm}^j(r-r^{j-1})} \equiv H2_m^j(r). \qquad (2.3)$$

We will use the asymptotic representations, Eq. (2.2) and Eq. (2.3), throughout the remainder of this chapter.

Impose continuity of pressure at the interface between segment j and segment $j+1$, i.e., at $r = r^j$,

$$p^{j+1}(r^j, z) = p^j(r^j, z), \qquad (2.4)$$

insert in Eq. (2.1), and we notice that

$$H1_m^{j+1}(r^j) = \sqrt{\frac{r^j}{r^j}} e^{ik_{rm}^j(r^j-r^j)} = 1,$$

$$H2_m^{j+1}(r^j) = \sqrt{\frac{r^j}{r^j}} e^{-ik_{rm}^j(r^j-r^j)} = 1,$$

thus, Eq. (2.4) gives

$$\sum_{m=1}^{M}[a_m^{j+1} + b_m^{j+1}]\Psi_m^{j+1}(z) = \sum_{m=1}^{M}[a_m^j H1_m^j(r^j) + b_m^j H2_m^j(r^j)]\Psi_m^j(z), \qquad (2.5)$$

Apply the operator

$$\int (\cdot)\frac{1}{\rho^{j+1}(z)}\Psi_l^{j+1}(z)\mathrm{d}z,$$

to Eq. (2.5), we have

$$a_l^{j+1} + b_l^{j+1} = \sum_{m=1}^{M}[a_m^j H1_m^j(r^j) + b_m^j H2_m^j(r^j)]\tilde{C}_{lm}^j, \qquad (2.6)$$

where

$$\tilde{C}_{lm}^j = \int \frac{1}{\rho^{j+1}(z)}\Psi_l^{j+1}(z)\Psi_m^j(z)\mathrm{d}z. \qquad (2.7)$$

51

Eq. (2.6) can be written in matrix:

$$a^{j+1} + b^{j+1} = \bar{C}^j (H1^j a^j + H2^j b^j), \qquad (2.8)$$

Where a^j and b^j are column vectors containing the coefficients a_m^j and b_m^j, respectively, and

$$\bar{C}^j = \begin{bmatrix} \tilde{C}_{11}^j & \tilde{C}_{12}^j & \cdots & \tilde{C}_{1M}^j \\ \tilde{C}_{21}^j & \tilde{C}_{22}^j & \cdots & \tilde{C}_{2M}^j \\ \vdots & \vdots & \vdots & \vdots \\ \tilde{C}_{M1}^j & \tilde{C}_{M2}^j & \cdots & \tilde{C}_{MM}^j \end{bmatrix},$$

$H1^j$ and $H2^j$ are diagonal matrices,

$$H1^j = \begin{bmatrix} H1_1^j & & & 0 \\ & H1_2^j & & \\ & & \ddots & \\ 0 & & & H1_M^j \end{bmatrix}, \quad H2^j = \begin{bmatrix} H2_1^j & & & 0 \\ & H2_2^j & & \\ & & \ddots & \\ 0 & & & H2_M^j \end{bmatrix}.$$

We next impose continuity of radial particle velocity at the interface between segment j and segment $j + 1$, i.e., at $r = r^j$,

$$v_r^{j+1}(r^j, z) = v_r^j(r^j, z), \qquad (2.9)$$

since

$$v_r \propto \frac{1}{\rho} \frac{\partial p}{\partial r},$$

and, with asymptotic representation of Hankel function, we have

$$
\begin{aligned}
\frac{\partial H1_m^j(r)}{\partial r} &= \frac{\partial}{\partial r}\left[\sqrt{\frac{r^{j-1}}{r}}e^{ik_{rm}^j(r-r^{j-1})}\right] \\
&= \left[\sqrt{r^{j-1}}(-\frac{1}{2})r^{-\frac{3}{2}} + \sqrt{\frac{r^{j-1}}{r}}ik_{rm}^j\right]e^{ik_{rm}^j(r-r^{j-1})} \\
&\approx \sqrt{\frac{r^{j-1}}{r}}ik_{rm}^j e^{ik_{rm}^j(r-r^{j-1})} \quad \text{for large } r \\
&= ik_{rm}^j H1_m^j(r),
\end{aligned}
$$

similarly,

$$
\frac{\partial H2_m^j(r)}{\partial r} \approx -ik_{rm}^j H2_m^j(r), \quad \text{for large } r
$$

Thus, Eq. (2.9) gives

$$
\frac{1}{\rho^{j+1}(z)}\sum_{m=1}^{M}k_{rm}^{j+1}[a_m^{j+1} - b_m^{j+1}]\Psi_m^{j+1}(z) = \frac{1}{\rho^j(z)}\sum_{m=1}^{M}k_{rm}^j[a_m^j H1_m^j(r^j) - b_m^j H2_m^j(r^j)]\Psi_m^j(z),
$$

$$(2.10)$$

Apply the operator

$$
\int(\cdot)\Psi_l^{j+1}(z)\mathrm{d}z,
$$

We get

$$
k_{rl}^{j+1}[a_l^{j+1} - b_l^{j+1}] = \sum_{m=1}^{M}k_{rm}^j[a_m^j H1_m^j(r^j) - b_m^j H2_m^j(r^j)]\int\frac{1}{\rho^j(z)}\Psi_l^{j+1}(z)\Psi_m^j(z)\mathrm{d}z,
$$

or,

$$
a_l^{j+1} - b_l^{j+1} = \sum_{m=1}^{M}[a_m^j H1_m^j(r^j) - b_m^j H2_m^j(r^j)]\hat{C}_{lm}^j,
$$

$$(2.11)$$

where

$$
\hat{C}_{lm}^j = \frac{k_{rm}^j}{k_{rl}^{j+1}}\int\frac{1}{\rho^j(z)}\Psi_l^{j+1}(z)\Psi_m^j(z)\mathrm{d}z.
$$

Eq. (2.11) can be written in matrix

$$
\boldsymbol{a}^{j+1} - \boldsymbol{b}^{j+1} = \hat{\boldsymbol{C}}^j(\boldsymbol{H1}^j\boldsymbol{a}^j - \boldsymbol{H2}^j\boldsymbol{b}^j),
$$

$$(2.12)$$

where

$$\hat{C}^j = [\hat{C}^j_{lm}]$$

$$= \begin{bmatrix} \hat{C}^j_{11} & \hat{C}^j_{12} & \cdots & \hat{C}^j_{1M} \\ \hat{C}^j_{21} & \hat{C}^j_{22} & \cdots & \hat{C}^j_{2M} \\ \vdots & \vdots & \vdots & \vdots \\ \hat{C}^j_{M1} & \hat{C}^j_{M2} & \cdots & \hat{C}^j_{MM} \end{bmatrix}. \tag{2.13}$$

Combine Eq. (2.8) and Eq. (2.12), we get

$$\begin{cases} a^{j+1} = & \frac{1}{2}(\tilde{C} + \hat{C})H1^j a^j + \frac{1}{2}(\tilde{C}^j - \hat{C}^j)H2^j b^j, \\ b^{j+1} = & \frac{1}{2}(\tilde{C} - \hat{C}^j)H1^j a^j + \frac{1}{2}(\tilde{C}^j + \hat{C}^j)H2^j b^j, \end{cases}$$

Thus, we obtain an explicit expression for a^{j+1} and b^{j+1},

$$\begin{bmatrix} b^{j+1} \\ a^{j+1} \end{bmatrix} = \begin{bmatrix} R^j_4 & R^j_3 \\ R^j_2 & R^j_1 \end{bmatrix} \begin{bmatrix} b^j \\ a^j \end{bmatrix}, \tag{2.14}$$

where

$$\begin{cases} R^j_1 = \frac{1}{2}(\tilde{C}^j + \hat{C}^j)H1^j, \\ R^j_2 = \frac{1}{2}(\tilde{C}^j - \hat{C}^j)H2^j, \\ R^j_3 = \frac{1}{2}(\tilde{C}^j - \hat{C}^j)H1^j, \\ R^j_4 = \frac{1}{2}(\tilde{C}^j + \hat{C}^j)H2^j. \end{cases} \tag{2.15}$$

In addition, the unknown coefficients satisfy the radiation condition $b^N = 0$ where segment N is the last segment (cf. Fig. 2-1), and the source condition([14])

$$a^1_m = \frac{i}{4\rho(z_s)}\Psi^1_m(z_s)H^{(1)}_0(k^1_{rm}r^1) + b^1_m \frac{H^{(1)}_0(k^1_{rm}r^1)}{H^{(2)}_0(k^1_{rm}r^1)}, \quad m = 1,\ldots,M \tag{2.16}$$

We can rewrite Eq. (2.16) in matrix form,

$$a^1 = d + Db^1, \tag{2.17}$$

54

where

$$d_m = \frac{i}{4\rho(z_s)} \Psi_m^1(z_s) H_0^{(1)}(k_{rm}^1 r^1),$$

$$D = \begin{bmatrix} \frac{H_0^{(1)}(k_{r1}^1 r^1)}{H_0^{(2)}(k_{r1}^1 r^1)} & & \\ & \ddots & \\ & & \frac{H_0^{(1)}(k_{rM}^1 r^1)}{H_0^{(2)}(k_{rM}^1 r^1)} \end{bmatrix}.$$

In fact, d_m can be determined easily by equaling the outgoing component and the range-independent solution in the source region. The outgoing component is

$$p_{out}^1(r, z) = \sum_m a_m^1 H1_m^1(r)\Psi_m^1(z)$$

$$= \sum_m a_m^1 \frac{H_0^{(1)}(k_{rm}^1 r)}{H_0^{(1)}(k_{rm}^1 r^1)} \Psi_m^1(z), \tag{2.18}$$

and the range-independent solution in the source region is

$$p_{indep}(r, z) = \frac{i}{4\rho(z_s)} \sum_m \Psi_m^1(z_s)\Psi_m^1(z)H_0^{(1)}(k_{rm}^1 r), \tag{2.19}$$

Equal Eqs. (2.18) and (2.19) and we have

$$a_m^1 \frac{1}{H_0^{(1)}(k_{rm}^1 r^1)} = \frac{i}{4\rho(z_s)} \Psi_m^1(z_s),$$

so,

$$a_m^1 = \frac{i}{4\rho(z_s)} \Psi_m^1(z_s)H_0^{(1)}(k_{rm}^1 r^1) \equiv d_m.$$

Having obtained all the coefficients a^j, b^j, we may obtain the pressure field in segment j by

$$p^j(r, z) = \sum_m [a_m^j H1_m^j(r) + b_m^j H2_m^j(r)]\Psi_m^j(z)$$

$$= \Psi^j(z)[H1^j(r)a^j + H2^j(r)b^j], \tag{2.20}$$

55

where $\Psi^j(z)$ is a row vector,

$$\Psi^j(z) = \begin{bmatrix} \Psi_1^j(z) & \cdots & \Psi_M^j(z) \end{bmatrix},$$

$H1^j(r)$ and $H2^j(r)$ are diagonal matrices.

To deal with the same problem with a line source, slight modifications are needed. For $x > 0$, we represent the pressure field in segment j as

$$p^j(x,z) = \sum_{m=1}^{M} [a_m^j E1_m^j(x) + b_m^j E2_m^j(x)] \Psi_m^j(z), \qquad (2.21)$$

where $x^{j-1} < x < x^j$, and

$$E1_m^j(x) = \frac{e^{ik_{xm}^j x}}{e^{ik_{xm}^j x^{j-1}}} = e^{ik_{xm}^j(x - x^{j-1})},$$

$$E2_m^j(x) = \frac{e^{-ik_{xm}^j x}}{e^{-ik_{xm}^j x^{j-1}}} = e^{-ik_{xm}^j(x - x^{j-1})}.$$

After imposing continuity of pressure and continuity of radial particle velocity at the interface between segment j and segment $j + 1$, i.e., at $r = r^j$, we get the same expression for a^{j+1} and b^{j+1}, Eq. (2.14). While d for line source has different form,

$$d_m = \frac{i}{2\rho(z_s)} \Psi_m^1(z_s) \frac{e^{ik_{xm}^1 x^1}}{k_{xm}^1}.$$

2.1.1 Approximate Coupled Modes

The full two-way coupled modes formulation allows for interactions between each segment in range and as a result leads to a global problem rather than a marching type of solution provided by, for instance, the parabolic equation. Computation time can be reduced by neglecting these multiple interactions, usually with only a minor degradation in accuracy.

An efficient marching implementation of coupled modes can be done in several ways with different degrees of accuracy([20]). Next we introduce two frequently used approximations.

1. Single-scatter approximation

   Single-scatter formulation treats each interface in range as an independent process thus neglects the higher-order multiple-scattering terms. We have known the matching at the interface $r = r^j$ is

   $$\begin{bmatrix} b^{j+1} \\ a^{j+1} \end{bmatrix} = \begin{bmatrix} R_4^j & R_3^j \\ R_2^j & R_1^j \end{bmatrix} \begin{bmatrix} b^j \\ a^j \end{bmatrix}.$$ (2.22)

   For the single-scatter approximation, the incoming wave in the left segment, i.e., a^j is assumed to be given. Initially,

   $$a^1 = d,$$

   where

   $$d_m = \frac{i}{4\rho(z_s)}\Psi_m(z_s)H_0^{(1)}(k_{rm}^1 r^1),$$

   and we require that the solution is purely outgoing in the right segment, i.e., $b^{j+1} = 0$. Solving for the backscattered amplitudes b^j yields

   $$b^j = -R_4^{j-1}R_3^j a^j.$$ (2.23)

   Therefore, the forward-scattered amplitudes a^{j+1} are given by

   $$a^{j+1} = (R_1^j - R_2^j R_4^{j-1} R_3^j)a^j,$$ (2.24)

   which is an explicit equation for the forward-scattered field.

2. One-way approximation

   One-way approximation neglects both the back-scattered amplitudes in the right segment b^{j+1} and b^j in the left segment. Thus from Eq. (2.22) we have

   $$a^{j+1} = R_1^j a^j.$$ (2.25)

Note that from Eq. (2.15) we know the one-way approximation Eq. (2.25), involves both pressure matching and velocity matching.

2.1.2 Matching Methods in One-Way Models

Porter, Jensen and Ferla([20]) presented several matching methods in one-way models. Here we make a brief review of those matching methods.

Fig. 2-2 shows a stair-case representation of a sloping bottom. The important interfaces with strong impedance contrasts are the horizontal interface I_h and the vertical interface I_V along the stair steps.
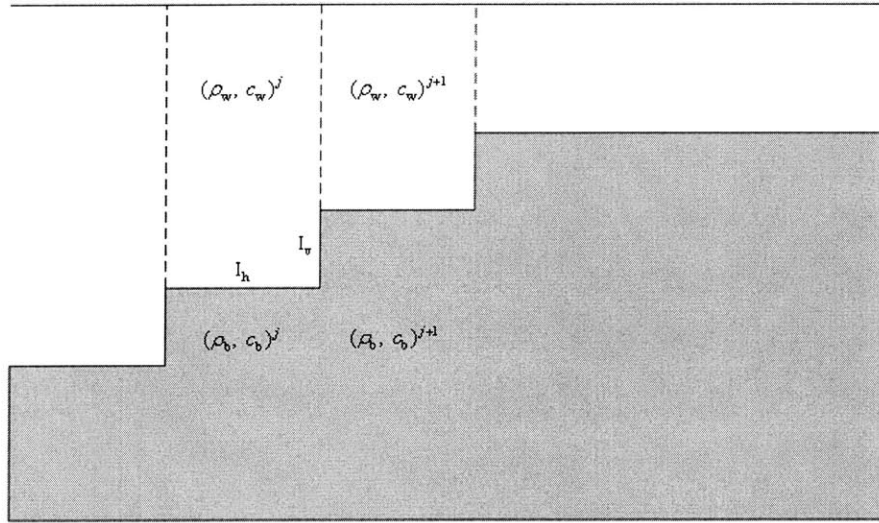
Figure 2-2: Stair-step representation of a sloping interface.

While conditions at horizontal interfaces (continuity of pressure and vertical particle velocity) are accurately implemented in finding the range-independent solution in each segment, the vertical interfaces I_V are treated very loosely in one-way models. The full-interface condition (continuity of pressure and horizontal particle velocity) at vertical interface I_V cannot in general be satisfied within the framework of a one-way solution.

As suggested by [20], next we consider which type of approximate interface condition should be used in one-way solutions in order to improve accuracy. Some guidance

can be gained by examining a 1-D wave equation. Thus we consider a problem with $c(x)$ being the sound speed and $\rho(x)$ being the density as a function of axial distance x. For such a 1-D problem, the 3-D Helmholtz equation

$$\rho \nabla \cdot \left(\frac{1}{\rho} \nabla p\right) + \frac{\omega^2}{c^2} p = 0$$

reduces to

$$\rho \frac{d}{dx}\left(\frac{1}{\rho} \frac{dp}{dx}\right) + \frac{\omega^2}{c^2(x)} p = 0, \tag{2.26}$$

where $p(x)$ is the acoustic pressure and ω is the frequency of the time-harmonic source.

For slowly varying $\rho(x)$, the WKB approximation to $p(x)$ is given by ([20], [2])

$$p(x) \sim A_0 \sqrt{\frac{\rho(x)}{\rho_0} \frac{k_0}{k(x)}} e^{i \int_0^x k(s)\,ds}, \tag{2.27}$$

where A_0, ρ_0 and k_0 is respectively amplitude, density and wavenumber at $x = 0$.

We now consider the results obtained by a piecewise constant discretization. Thus, as illustrated schematically in Fig. 2-3, the medium is approximated by a sequence of N segments with both sound speed and density constant within a segment.
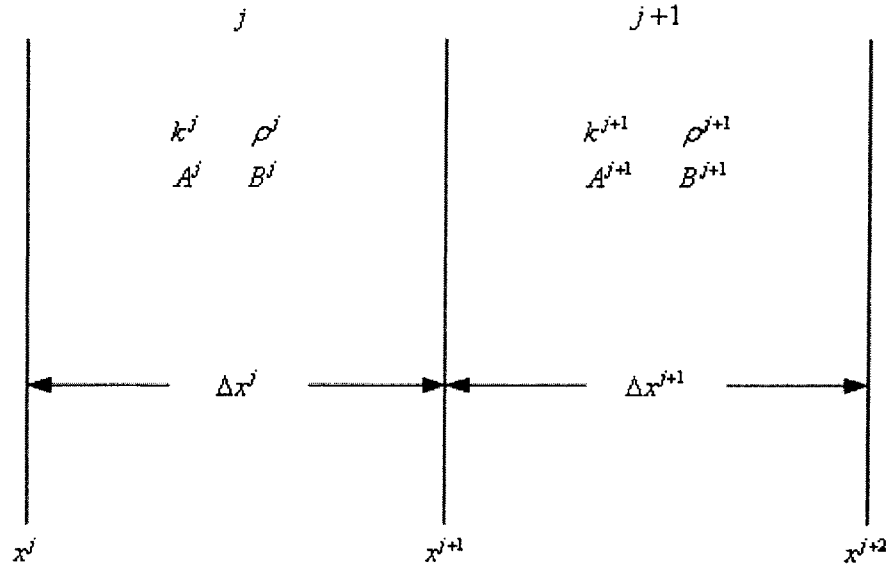
Figure 2-3: Discretization of the 1-D wave equation.

The solution in the jth segment can then be written as the sum of a right- and left- traveling wave as follows:

$$p^j(x) = A^j e^{ik^j(x-x^j)} + B^j e^{-ik^j(x-x^j)}, \qquad (2.28)$$

where x^j and x^{j+1} are the endpoints of the jth segment and k^j is the wave number in that segment. We next consider the effect of several possible interface conditions.

A. Pressure-matching

In this case, we assume that $B^j = 0$ for each segment, so

$$p^j(x) = A^j e^{ik^j(x-x^j)},$$

matching pressure at $x = x^{j+1}$ leads to

$$A^j e^{ik^j(x^{j+1}-x^j)} = A^{j+1} e^{ik^{j+1}(x^{j+1}-x^{j+1})},$$

denote $\Delta x^j = x^{j+1} - x^j$, then we obtain

$$A^{j+1} = A^j e^{ik^j \Delta x^j}, \qquad (2.29)$$

which implies

$$\begin{aligned}
A^N &= A^{N-1} e^{ik^{N-1}\Delta x^{N-1}} \\
&= (A^{N-2} e^{ik^{N-2}\Delta x^{N-2}}) e^{ik^{N-1}\Delta x^{N-1}} \\
&= A^0 e^{ik^0 \Delta x^0} \cdot e^{ik^1 \Delta x^1} \cdots e^{ik^{N-1}\Delta x^{N-1}} \\
&= A^0 e^{i \sum\limits_{j=0}^{N-1} k^j \Delta x^j}. \qquad (2.30)
\end{aligned}$$

Now taking the limit as the number of segments goes to infinity yields:

$$p(x) = A^0 e^{i \int_0^x k(s)\,\mathrm{d}s}. \qquad (2.31)$$

By comparing Eq. (2.31) and Eq. (2.27), the pressure-matched solution shows a constant amplitude, while the WKB amplitude varies in proportion $\sqrt{\frac{\rho(x)}{k(x)}}$.

B. Velocity matching

Again, we assume $B^j = 0$ for each segment. Matching $\frac{dp}{dx}/\rho$ at each interface leads to

$$A^j i k^j e^{ik^j(x^{j+1}-x^j)}\frac{1}{\rho^j} = A^{j+1} i k^{j+1} e^{ik^{j+1}(x^{j+1}-x^{j+1})}\frac{1}{\rho^{j+1}},$$

thus we obtain

$$A^{j+1} = A^j \frac{\rho^{j+1}}{\rho^j}\frac{k^j}{k^{j+1}}e^{ik^j\Delta x^j},\tag{2.32}$$

which implies

$$A_N = A_0 \prod_{j=0}^{N-1}\frac{\rho^{j+1}}{\rho^j}\frac{k^j}{k^{j+1}}e^{ik^j\Delta x^j}$$

$$= A_0 \frac{\rho^N}{\rho^0}\frac{k^0}{k^N}e^{i\sum\limits_{j=0}^{N-1}k^j\Delta x^j}.\tag{2.33}$$

Now taking the limit as the number of segments goes to infinity yields

$$p(x) = A_0 \frac{\rho(x)}{\rho^0}\frac{k^0}{k(x)}e^{i\int_0^x k(s)ds}.\tag{2.34}$$

Once again, the phase factor is correct while the amplitude incorrect.

C. Reduced-pressure matching

We still assume $B^j = 0$, matching $p/\sqrt{\rho}$ at each interface leads to

$$\frac{A^j e^{ik^j(x^{j+1}-x^j)}}{\sqrt{\rho^j}} = \frac{A^{j+1} e^{ik^{j+1}(x^{j+1}-x^{j+1})}}{\sqrt{\rho^{j+1}}},$$

thus we obtain

$$A^{j+1} = A^j \sqrt{\frac{\rho^{j+1}}{\rho^j}}e^{ik^j\Delta x^j},\tag{2.35}$$

which implies

$$A^N = A^0 \prod_{j=1}^{N-1} \sqrt{\frac{\rho^{j+1}}{\rho^j}} e^{ik^j \Delta x^j}$$

$$= A_0 \sqrt{\frac{\rho^N}{\rho^0}} e^{i \sum\limits_{j=0}^{N-1} k^j \Delta x^j} \qquad (2.36)$$

Again, taking the limit as the number of segments goes to infinity yields

$$p(x) = A^0 \sqrt{\frac{\rho(x)}{\rho^0}} e^{i \int_0^x k(s) ds}. \qquad (2.37)$$

Thus, by matching reduced pressure, we correct for the errors due to density variation but not for those due to the change in sound speed.

D. Impedance matching

It is evident that some additional correction is needed to account for the effect of variations in $k(x)$, i.e., of variations in sound speed $c(x)$. As suggested by Westwood and Collins ([5]), we match $p/\sqrt{\rho c}$ across interfaces. (We refer to this matching method as impedance matching although it actually involves the square root of the material impedance.)

We still assume $B^j = 0$ in each segment, impedance matching at each interface implies

$$\frac{A^j e^{ik^j(x^{j+1} - x^j)}}{\sqrt{\rho^j c^j}} = \frac{A^{j+1} e^{ik^{j+1}(x^{j+1} - x^{j+1})}}{\sqrt{\rho^{j+1} c^{j+1}}},$$

thus we obtain

$$A^{j+1} = A^j \sqrt{\frac{\rho^{j+1}}{\rho^j} \frac{c^{j+1}}{c^j}} e^{ik^j \Delta x^j}$$

$$= A^j \sqrt{\frac{\rho^{j+1}}{\rho^j} \frac{k^j}{k^{j+1}}} e^{ik^j \Delta x^j}. \qquad (2.38)$$

62

Taking the limit as the number of segments goes to infinity yields

$$p(x) = A^0 \sqrt{\frac{\rho(x)}{\rho^0} \frac{k^0}{k(x)}} e^{i \int_0^x k(s) ds}, \qquad (2.39)$$

which agrees precisely with the energy conserving WKB result.

E. Single scatter

The single-scatter result is obtained by treating each pair of segments as an independent problem, thus neglecting the higher-order terms resulting from multiple scattering (reflection and transmission) at other interfaces.

In the left segment, we allow both an incident right-traveling wave with coefficient A^j and a reflected left-traveling wave with coefficient B^j. In the right segment, we allow only an outgoing transmitted wave with coefficient A^{j+1}. The two unknowns, B^j and A^{j+1}, permit us to impose both continuity of pressure and particle velocity:

$$A^{j+1} = A^j e^{ik^j \Delta x^j} + B^j e^{-ik^j \Delta x^j}, \qquad (2.40)$$

$$A^{j+1} = \frac{\rho^{j+1}}{\rho^j} \frac{k^j}{k^{j+1}} (A^j e^{ik^j \Delta x^j} - B^j e^{-ik^j \Delta x^j}), \qquad (2.41)$$

solving for A^{j+1}, we obtain

$$A^{j+1} = A^j \frac{2 e^{ik^j \Delta x^j}}{1 + \frac{\rho^j}{\rho^{j+1}} \frac{k^{j+1}}{k^j}}, \qquad (2.42)$$

which implies

$$A^N = A^0 \prod_{j=0}^{N-1} \frac{2 e^{ik^j \Delta x^j}}{1 + \frac{\rho^j}{\rho^{j+1}} \frac{k^{j+1}}{k^j}}. \qquad (2.43)$$

It can be shown ([20], [3]) that

$$p(x) = A^0 \sqrt{\frac{\rho(x)}{\rho^0} \frac{k^0}{k(x)}} e^{i \int_0^x k(s) ds}, \qquad (2.44)$$

which is precisely the WKB result.

Summary of results:

The results of these various interface conditions are summarized as follows:

$$e^{i \int_0^x k(s)ds} \qquad p \text{ matched}$$

$$\frac{\rho(x)}{\rho_0} \frac{k_0}{k(x)} e^{i \int_0^x k(s)ds} \qquad \frac{dp}{dx}/\rho \text{ matched}$$

$$\sqrt{\frac{\rho(x)}{\rho_0}} e^{i \int_0^x k(s)ds} \qquad \frac{p}{\sqrt{\rho}} \text{ matched}$$

$$\sqrt{\frac{\rho(x)}{\rho_0} \frac{k_0}{k(x)}} e^{i \int_0^x k(s)ds} \qquad \frac{p}{\sqrt{\rho c}} \text{ matched/single scatter/WKB}$$

Comparing these forms we see that the pressure matched solution shows serious deficiencies for moderate density variation. Velocity matching is also a poor choice, however, reduced-pressure matching corrects entirely for the density effect. If $c(x)$ varies much less than $\rho(x)$ the reduced-pressure matching would correct most of the error. A further improvement may be obtained using the impedance matching or the single-scatter approximation.

For one-dimensional problems, the impedance matching and the single-scatter approximation corrects for sound speed changes as well as density changes across interfaces. However, for two-dimensions some complications arise, and matching $p/\sqrt{\rho c}$ or single-scatter approximation does not entirely resolve the energy conservation problem.

2.1.3 Implementation of Coupled Modes in Ideal Waveguides

For ideal waveguide with a homogeneous water layer bounded above by a pressure-release surface and below by a rigid or soft bottom, we may obtain analytical representation for the coupling matrixes $\tilde{C}^j$ and $\hat{C}^j$.

Due to the homogeneous water layer, both $\tilde{C}^j_{lm}$ and $\hat{C}^j_{lm}$ depend on the integral

$$I = \int_0^D \Psi_l^{j+1}(z)\Psi_m^j(z)dz, \qquad (2.45)$$

64

where $D = \min(D^j, D^{j+1})$, D^j and D^{j+1} are the water depth in segment j and $j+1$, respectively.

For ideal waveguides (rigid or soft bottom), eigenfunctions take the form

$$\Psi_m(z) = \sqrt{\frac{2\rho}{D}} \sin(k_{zm} z),$$

thus, the integral in Eq. (2.45) becomes

$$
\begin{aligned}
I &= \int_0^D \Psi_m^j(z) \Psi_l^{j+1}(z) \mathrm{d}z \\
&= \int_0^D \sqrt{\frac{2\rho}{D_1}} \sin(k_{zm}^j z) \sqrt{\frac{2\rho}{D_2}} \sin(k_{zl}^{j+1} z) \mathrm{d}z \\
&= \frac{2\rho}{\sqrt{D_1 D_2}} \int_0^D \sin(k_{zm}^j z) \sin(k_{zl}^{j+1} z) \mathrm{d}z \\
\sin\alpha \sin\beta &= \frac{1}{2}[\cos(\alpha - \beta) - \cos(\alpha + \beta)] \\
&= \frac{2\rho}{\sqrt{D_1 D_2}} \frac{1}{2} \left[\int_0^D \cos(k_{zm}^j - k_{zl}^{j+1}) z \mathrm{d}z - \int_0^D \cos(k_{zm}^j + k_{zl}^{j+1}) z \mathrm{d}z \right]
\end{aligned}
$$

- When $k_{zm}^j = k_{zl}^{j+1}$,

$$I = \frac{\rho}{\sqrt{D_1 D_2}} \left[D - \frac{1}{2k_{zm}^j} \sin(2k_{zm}^j D) \right].$$

- When $k_{zm}^j \neq k_{zl}^{j+1} l$,

$$I = \frac{\rho}{\sqrt{D_1 D_2}} \left[\frac{1}{k_{zm}^j - k_{zl}^{j+1}} \sin(k_{zm}^j - k_{zl}^{j+1}) D - \frac{1}{k_{zm}^j + k_{zl}^{j+1}} \sin(k_{zm}^j + k_{zl}^{j+1}) D \right].$$

2.2 The Decoupling of Stepwise Coupled Modes

In this part, we will show the decoupling algorithm used in the program COUPLE([8]). COUPLE is a program that performs a stepwise coupled modes ([7], [14]) calculation of the two dimensional underwater acoustic field with a vertical array of harmonic point sources in cylindrical geometry or with a line source in plane geometry. The method of eliminating the instabilities in COUPLE is similar to the invariant embed-

ding approach used for wavenumber integration ([14, p. 227]).

2.2.1 Numerical Problem of the Traditional Two-Way Coupled Modes Method

The modes coupling equation may be written as

$$
\begin{bmatrix} b^{j+1} \\ a^{j+1} \end{bmatrix} = R^j \begin{bmatrix} b^j \\ a^j \end{bmatrix}, \quad j = 1, 2, \ldots, N-1 \tag{2.46}
$$

where R^j is the $2M \times 2M$ matrix containing the block submatrices R_4^j, R_3^j, R_2^j and R_1^j,

$$
R^j = \begin{bmatrix} R_4^j & R_3^j \\ R_2^j & R_1^j \end{bmatrix},
$$

thus, we have

$$
\begin{aligned}
\begin{bmatrix} b^N \\ a^N \end{bmatrix} &= R^{N-1} \begin{bmatrix} b^{N-1} \\ a^{N-1} \end{bmatrix} \\
&= R^{N-1} R^{N-2} \cdots R^1 \begin{bmatrix} b^1 \\ a^1 \end{bmatrix} \\
&= \begin{bmatrix} S_4 & S_3 \\ S_2 & S_1 \end{bmatrix} \begin{bmatrix} b^1 \\ a^1 \end{bmatrix},
\end{aligned} \tag{2.47}
$$

where S is a product of the matrices R^j, $j = N-1, N-2, \ldots, 1$,

$$
S = R^{N-1} R^{N-2} \cdots R^1
$$

so,

$$
b^N = S_4 b^1 + S_3 a^1, \tag{2.48}
$$

The radiation condition $b^N = 0$ implies that

$$S_4 b^1 + S_3 a^1 = 0, \qquad (2.49)$$

Combine Eq. (2.49) with the source condition

$$a^1 = d + D b^1, \qquad (2.50)$$

we can obtain the equation for b^1,

$$b^1 = -(S_4 + S_3 D)^{-1} S_3 d \qquad (2.51)$$

Known b^1, a^1 is obtained by Eq. (2.50). Having obtained b^1 and a^1, the rest of the coefficients, b^j and a^j for $j = 2, \ldots, N$ are obtained from Eq. (2.46). The resulting coefficients are substituted into Eq. (2.20) to give the stepwise coupled mode solution.

The traditional two-way coupled modes method described above is simple but may encounter numerical problems, when propagation is carried out over many wavelengths. The matrix S is a product of the matrices R^j, $j = N - 1, \ldots, 1$. Each of the R^j contains exponentially growing and decaying factors resulting from the normalized Hankel functions in Eq. (2.1). The growing and decaying factors are coupled by different basis(mode coupling) at the stepwise depth variations. It is not always possible to evaluate the inverse of the matrix $S_4 + S_3 D$ in Eq. (2.51), because both $S_4 + S_3 D$ and $S_3 d$ may be too large to obtain a meaningful solution for b^1. This difficulty with the traditional two-way coupled modes method suggests that we should attempt to decouple the growing and decaying solutions. This is the motivation for the decoupling algorithm.

67

2.2.2 Decoupling of Stepwise Coupled Modes

Define the $2M \times 1$ column vector x^j as

$$x^j = \begin{bmatrix} b^j \\ a^j \end{bmatrix},$$

then matrix-vector recursion in Eq. (2.46) becomes

$$x^{j+1} = R^j x^j, \quad j = 1, \ldots, N-1 \tag{2.52}$$

A fundamental matrix solution of Eq. (2.52) is a $2M \times 2M$ matrix X^j with linear independent columns that satisfies the matrix recursion

$$X^{j+1} = R^j X^j, \quad j = 1, \ldots, N-1 \tag{2.53}$$

Define the transformation

$$X^j = T^j Y^j, \tag{2.54}$$

where $T^1 = I$ and T^{j+1} is found by the modified Gram-Schmidt orthogonalization([21]) of the columns of $R^j T^j$ for $j = 1, \ldots, N-1$. This decomposition has the form

$$R^j T^j = T^{j+1} U^j, \tag{2.55}$$

where T^{j+1} is unity and U^j is upper triangular. Substituting Eq. (2.54) and Eq. (2.55) into Eq. (2.53),

$$T^{j+1} Y^{j+1} = R^j T^j Y^j$$
$$= T^{j+1} U^j Y^j,$$

so we obtain the matrix recursion for the new unknown matrix Y^j,

$$Y^{j+1} = U^j Y^j, \quad j = 1, \ldots, N-1 \tag{2.56}$$

U^j in Eq. (2.56) is upper triangular, partition it as

$$U^j = \begin{bmatrix} B^j & C^j \\ 0 & E^j \end{bmatrix},$$

and partition Y^j as

$$Y^j = \begin{bmatrix} Y_4^j & Y_3^j \\ Y_2^j & Y_1^j \end{bmatrix},$$

then Eq. (2.56) leads to

$$\begin{bmatrix} Y_4^{j+1} & Y_3^{j+1} \\ Y_2^{j+1} & Y_1^{j+1} \end{bmatrix} = \begin{bmatrix} B^j & C^j \\ 0 & E^j \end{bmatrix} \begin{bmatrix} Y_4^j & Y_3^j \\ Y_2^j & Y_1^j \end{bmatrix},$$

thus we have

$$Y_4^{j+1} = B^j Y_4^j + C^j Y_2^j, \qquad (2.57a)$$

$$Y_3^{j+1} = B^j Y_3^j + C^j Y_1^j, \qquad (2.57b)$$

$$Y_2^{j+1} = E^j Y_2^j, \qquad (2.57c)$$

$$Y_1^{j+1} = E^j Y_1^j. \qquad (2.57d)$$

It is apparent that Y_1^{j+1} and Y_2^{j+1} are decoupled from Y_3^j and Y_4^j. The original unknowns are not decopled but they can be obtained from the new decoupled unknowns using Eq. (2.54). It turns out([8]) that Eq. (2.57) can be solved without the numerical problems encountered in solving Eq. (2.53).

A matrix solution of Eq. (2.57) will be generated as follows. Let $Y_2^1 = 0$ and $Y_1^1 = I$. Then Eq. (2.57c) implies $Y_2^j = 0$ for $j = 1, \ldots, N$, so Eq. (2.57c) is not explicitly needed. From Eq. (2.57d) we may obtain Y_1^{j+1} in the remaining region in the outgoing direction for $j = 1, \ldots, N-1$.

Having found Y_1^N, choose Y_4^N and Y_3^N to satisfy the radiation condition in the last region, which requires the ingoing components(first M rows, which corresponds to the coefficients b^j) of the matrix $X^N = T^N Y^N$ are identically zero.

69

Let T^N be partitioned as

$$T^N = \begin{bmatrix} T_4^N & T_3^N \\ T_2^N & T_1^N \end{bmatrix}$$

then

$$X^N = T^N Y^N = \begin{bmatrix} T_4^N & T_3^N \\ T_2^N & T_1^N \end{bmatrix} \begin{bmatrix} Y_4^N & Y_3^N \\ Y_2^N & 0 & Y_1^N \end{bmatrix} = \begin{bmatrix} T_4^N Y_4^N & T_4^N Y_3^N + T_3^N Y_1^N \\ T_2^N Y_4^N & T_2^N Y_3^N + T_1^N Y_1^N \end{bmatrix}$$

so the first M rows of X^N are zero leads to

$$T_4^N Y_4^N = 0, \tag{2.58}$$

and

$$T_4^N Y_3^N + T_3^N Y_1^N = 0 \tag{2.59}$$

To satisfy Eq. (2.58), we may choose $Y_4^N = 0$, thus together with $Y_2^j = 0$, for $j = 1, \ldots, N$, Eq. (2.57a) implies that $Y_4^j = 0$ for $j = 1, \ldots, N$, which means, like Eq. (2.57c), Eq. (2.57a) is not used explicitly.

From Eq. (2.59), we get

$$Y_3^N = -(T_4^N)^{-1} T_3^N Y_1^N,$$

thus we can solve Eq. (2.57b) for Y_3^j in each remaining segment in the ingoing direction with decreasing $j = N - 1, \ldots, 1$.

The solution to Eq. (2.57) just obtained(i.e., Y^j for $j = 1, \ldots, N$) is multiplied by T^j to obtain the general matrix solution of Eq. (2.53) that satisfies the radiation condition in segment N. Thus any vector solution of Eq. (2.52) satisfies the radiation condition in segment N can be written as

$$x^j = \begin{bmatrix} b^j \\ a^j \end{bmatrix} = T^j Y^j c, \tag{2.60}$$

where c is an arbitrary $2M \times 1$ vector.

If $c = \begin{bmatrix} c_2 \\ c_1 \end{bmatrix}$, then

$$
\begin{aligned}
Y^j c &= \begin{bmatrix} Y_4^j{}^{0} & Y_3^j \\ Y_2^j{}^{0} & Y_1^j \end{bmatrix} \begin{bmatrix} c_2 \\ c_1 \end{bmatrix} \\
&= \begin{bmatrix} Y_3^j c_1 \\ Y_1^j c_1 \end{bmatrix},
\end{aligned}
\tag{2.61}
$$

thus we have

$$
\begin{aligned}
x^N &= \begin{bmatrix} b^N \\ a^N \end{bmatrix} \\
&= T^N Y^N c \\
&= \begin{bmatrix} T_4^N & T_3^N \\ T_2^N & T_1^N \end{bmatrix} \begin{bmatrix} Y_3^N c_1 \\ Y_1^N c_1 \end{bmatrix} \\
&= \begin{bmatrix} T_4^N Y_3^N c_1 + T_3^N Y_1^N c_1 \\ T_2^N Y_3^N c_1 + T_1^N Y_1^N c_1 \end{bmatrix} \\
&\text{insert in Eq. (2.59)} \\
&= \begin{bmatrix} 0 \\ T_2^N Y_3^N c_1 + T_1^N Y_1^N c_1 \end{bmatrix},
\end{aligned}
\tag{2.62}
$$

so we can see, the radiation condition $b^N = 0$ is already satisfied. We can get c_1 with the source condition.

In the first segment,

$$x^1 = \begin{bmatrix} b^1 \\ a^1 \end{bmatrix} = T^1 Y^1 c$$

insert in $T^1 = I$

$$= Y^1 c$$

Eq. (2.61)

$$= \begin{bmatrix} Y_3^1 c_1 \\ Y_1^1 c_1 \end{bmatrix}$$

insert in $Y_1^1 = I$

$$= \begin{bmatrix} Y_3^1 c_1 \\ c_1 \end{bmatrix}, \qquad (2.63)$$

so, $a^1 = c_1$, and $b^1 = Y_3^1 c_1$, insert into the source condition,

$$a^1 = d + D b^1,$$

we have

$$c_1 = d + D Y_3^1 c_1,$$

thus, we obtain c_1,

$$c_1 = (I - D Y_3^1)^{-1} d. \qquad (2.64)$$

Having found c_1, we may obtain a^1 and b^1 from Eq. (2.63), and the remaining coefficients a^j and b^j, for $j = 2, \ldots, N$, are obtained from Eqs. (2.60) and (2.61).

2.2.3 Comparison of the Traditional Two-Way Coupled Modes Method with the Decoupling Algorithm

To make the comparison, it is helpful to introduce the reflection matrix for segment 2 through segment N. The reflection matrix relates the incoming (reflected) coefficients

to the outgoing (incident) coefficient in segment 1.

For the decoupling algorithm, since $a^1 = c_1$, and $b^1 = Y_3^1 c_1$, which leads to $b^1 = Y_3^1 a^1$, the matrix Y_3^1 is the reflection matrix for segment 2 through N, denoted as

$$R_d = Y_3^1,$$

the coefficient a^1 is found by

$$a^1 = (I - DR_d)d. \qquad (2.65)$$

For the traditional two-way coupled modes method, the source condition and the radiation condition imply that

$$b^1 = -S_4^{-1} S_3 a^1,$$

thus the reflection matrix is given by $-S_4^{-1} S_3$, denoted as

$$R_t = -S_4^{-1} S_3,$$

the coefficient a^1 is found by

$$a^1 = (I - DR_t)d. \qquad (2.66)$$

Comparing Eq. (2.65) and Eq. (2.66), we see that the only difference is the way the reflection matrix is computed.

We expect, from physical consideration, that the reflection matrix is well behaved and small in most applications. There should be no problem in computing the reflection matrix if the calculation is arranged correctly. The calculation of $S_4^{-1} S_3$ can be difficult since, although $S_4^{-1} S_3$ is well behaved, both S_4 and S_3 can contain very large matrix elements. The decoupling algorithm is a better way of computing the reflection matrix since it avoids this calculation.

A comparison based on computational and storage requirements is also needed.

The steps in the traditional two-way coupled modes method:

(1) For $j = 1, \ldots, N - 1$, find and store R^j; accumulate the product S.

(2) Solve Eq. (2.51) for b^1 and compute a^1 using the source condition.

(3) For $j = 1, \ldots, N - 1$, read R^j; generate a^{j+1} and b^{j+1}.

The steps in the decoupling algorithm:

(0) Let $T_1 = I$ and $Y_1^1 = I$.

(1) For $j = 1, \ldots, N - 1$, find R^j; orthogonalize $R^j T^j$ to find T^{j+1} and U^j; compute Y_1^{j+1} using Eq. (2.57d); store T^{j+1}, B^j, C^j, and Y_1^{j+1}.

(2a) Solve Eq. (2.59) for Y_3^N and store it.

(2b) For $j = N - 1, \ldots, 1$, read B^j, C^j, and Y_1^j; solve Eq. (2.57b) for Y_3^j; store Y_3^j.

(2c) Solve Eq. (2.65) for $c_1 = a^1$ and compute $b^1 = Y_3^1 a^1$.

(3) For $j = 2, \ldots, N$, read T^j, Y_3^j, and Y_1^j; generate a^j and b^j using Eqs. (2.60) and (2.61).

We see from the lists above that the decoupling algorithm involves more steps than the traditional two-way coupled modes method. It takes more time to run the decoupling algorithm than the traditional two-way coupled modes method. At the same time, the decoupling algorithm requires about twice as much as storage as the traditional two-way coupled modes method.

2.3 C-SNAP: Coupled SACLANTCEN Normal Mode Propagation Loss Model([10])

2.3.1 Introduction

In ocean environments where either the water depth, the sound-speed profile, or the bottom composition vary significantly over the propagation path, sonar performance predictions cannot be satisfactory addressed without taking into account the

range-dependent properties of the environment. Though several numerical models are currently available for solving propagation problems in range-dependent environments, they tend to be quite sophisticated and their correct use requires considerable skill on the part of the model user. C-SNAP is built with the main objective of being particularly easy to handle and competitive in terms of execution time with the existing parabolic equation algorithm C-SNAP code is written in standard Fortran and thus can be easily implemented on a personal computer.

C-SNAP has the following properties:

(a) The code incorporates a reliable algorithm for the automatic selection of the vertical grid spacing to be used for accurately matching the solution all in range.

(b) It bypasses the calculation of mode coupling matrices and compute the mode coefficients in a new segment by projecting the pressure field onto the new mode set.

(c) To preserve accuracy, an energy-conserving matching condition(impedance matching) is implemented at the coupling interfaces.

(d) The SACLANTCEN range independent normal mode program SNAP([12]) was taken as the main building block on top of which range-dependent features have been added.

2.3.2   Program Overview

The Mathematical Model

From 1.2, we know the normal mode representation of the acoustic pressure produced by a harmonic point source in a horizontally stratified medium is given by the following expression:

$$p(r, z) = \frac{i}{4\rho(z_s)} \sum_{m=1}^{\infty} \Psi_m(z_s)\Psi_m(z)H_0^{(1)}(k_{rm}r), \tag{2.67}$$

In C-SNAP, we use the large-argument asymptotic approximation of the Hankel function and neglect the contribution of the continuous spectrum. With M indicating the largest-order discrete mode of the problem, we come to the following expression:

$$p(r, z) = \frac{i}{\rho(z_s)\sqrt{8\pi r}} e^{-i\frac{\pi}{4}} \sum_{m=1}^{M} \Psi_m(z_s)\Psi_m(z)\frac{e^{ik_{rm}r}}{\sqrt{k_{rm}}}. \tag{2.68}$$

The numerical method employed to find the mode amplitudes(Ψ_m) is based on the finite difference algorithm in combination with an inverse iteration technique. The eigenvalue(k_{rm}) may be successively refined over a sequence of meshes and finally extrapolated to yield the solution of an infinitely dense mesh, thus resulting as an improved estimate of the continuous problem([19]).

Loss mechanisms such as volume attenuation in the water column, bottom absorption, shear, and scattering from surface and bottom boundaries are included int the imaginary part of the eigenvalue k_{rm}. They are computed through a perturbational approach.

The range-dependent case is solved by generalizing the one-way formulation of the range-independent solution as follows:

(a) Subdividing the propagation path in a sequence of range-independent segments, with sloping bottoms treated by the staircase approximation. Environmental properties for the various range subdivisions are obtained through a linear interpolation in range between adjacent profile inputs.

(b) Finding the normal modes, the eigenvalues and the associated properties in the first segment and computing the pressure field as in the range-independent case until the interface to the next segment is reached.

(c) The mode set pertaining to the next segment is computed and the pressure field to the left of the interface is projected onto the new mode set. The resulting mode coefficients (excitation coefficients) are then used to carry on the computation of the pressure field in the new segment. This procedure is repeated for each new segment.

76

Similar to the one-way approximation described in 2.1.1, C-SNAP neglects the backscattered amplitudes b^j in all segments. Thus the pressure field in segment j is

$$p^j(r, z) = \sum_{m=1}^{M^j} a_m^j \frac{H_0^{(1)}(k_{rm}^j r)}{H_0^{(1)}(k_{rm}^j r^{j-1})} \Psi_m^j(z), \qquad (2.69)$$

and in the first segment($j = 1$) as a special case we set $r^{j-1} = r^1$, and define the mode coefficient as

$$a_m^1 = \frac{i}{4\rho(z_s)} \Psi_m^1(z_s) H_0^{(1)}(k_{rm}^1 r^1). \qquad (2.70)$$

Also, to preserve accuracy, the interface condition which is suggested by Collins and Westwood([17]), and implemented in a PE code, is implemented in C-SNAP([16]). This approach, which we will refer to as an impedance matching, consists in matching $\frac{p}{\sqrt{\rho c}}$ across each interface.

By observing that at the beginning of each interface the ratio of the Hankel functions is always equal to one, the impedance matching at the interface $r = r^j$ yields

$$\frac{1}{\sqrt{\rho^{j+1}(z)c^{j+1}(z)}} \sum_{m=1}^{M^{j+1}} a_m^{j+1} \Psi_m^{j+1}(z) = \frac{1}{\sqrt{\rho^j(z)c^j(z)}} \sum_{m=1}^{M^j} a_m^j \frac{H_0^{(1)}(k_{rm}^j r^j)}{H_0^{(1)}(k_{rm}^j r^{j-1})} \Psi_m^j(z).$$
$$(2.71)$$

By applying to Eq. (2.71) the operator

$$\int (\cdot) \frac{\Psi_l^{j+1}(z)}{\sqrt{\rho^{j+1}(z)}} dz,$$

We obtain

$$a_l^{j+1} = \int \sum_{m=1}^{M^j} a_m^j \frac{H^{(1)}(k_{rm}^j r^j)}{H_0^{(1)}(k_{rm}^j r^{j-1})} \frac{\Psi_m^j(z)\Psi_l^{j+1}(z)}{\sqrt{\rho^j(z)\rho^{j+1}(z)\frac{c^j(z)}{c^{j+1}(z)}}} dz, \qquad l = 1, \ldots, M^{j+1}$$

insert in Eq. (2.69)

$$= \int p^j(r^j, z) \frac{\Psi_l^{j+1}(z)}{\sqrt{\rho^j(z)\rho^{j+1}(z)\frac{c^j(z)}{c^{j+1}(z)}}} dz, \qquad l = 1, \ldots, M^{j+1}, \qquad (2.72)$$

Eq. (2.72) is the expression evaluated at each interface by C-SNAP. It only requires

the pressure field over depth to the left of the interface and the eigenfunction in the new range segment.

In C-SNAP, the Hankel functions are replaced with their large-argument asymptotic representation. Other interface conditions such as pressure-matching and reduced-pressure matching([20]) are also obtained from C-SNAP and may be convenient in comparing results with different models.

The Environmental Model

As shown in Fig. 2-4, the different segments used to describe the range-dependent environment are treated as a half-space subdivided into three main layers consisting of a water column of depth H_0, a sediment layer of thickness H_1, and a semi-infinite homogeneous subbottom. The sound speeds c_0 in the water column and c_1 in the sediment layer may vary with depth, while density (ρ_0, ρ_1) and volume attenuation (β_0, β_1) are kept constant within the two layers. The subbottom is treated as a solid with depth independent properties: c_2 is the compressional speed, ρ_2 the density, β_2 the compressional attenuation, c_{2s} is the shear speed and β_{2s} the shear attenuation. Furthermore, the sea surface and the seafloor are treated as rough boundaries, with s_0 and s_1 indicating the rms wave height.

The environment between any two input profiles is approximated by a series of range-independent segments with a sloping bottom being described by a staircase approximation. In Fig. 2-5 we show a case with distinct slopes at both the water-sediment and sediment-subbottom interfaces. The symbols P_1, P_2, and P_m denote the location of the different input profiles used to represent the range-dependent environment, S_1, S_2, and S_n are the range-independent segments used for representing a sloping bottom via a staircase approximation, r_1, r_2, and r_n are the positions of the interfaces between adjacent segments where the mode coupling is performed. The number of range subdivisions between any consecutive input profiles (P_j, P_{j+1}) is controlled by an input parameter. The environmental properties in each of the resulting segments are obtained through linear interpolation in range.

In the case of a sloping bottom, the interpolation to compute the sound-velocity

profile in the water and/or in the sediment layer is performed after the shallowest sound-velocity profile is extended with data points from the deepest one. Also, these data points are adjusted through a parallel shift in order to match the last point in the shallowest sound-velocity profile. Care should be taken to ensure that this technique is adequate to describe the expected environment.
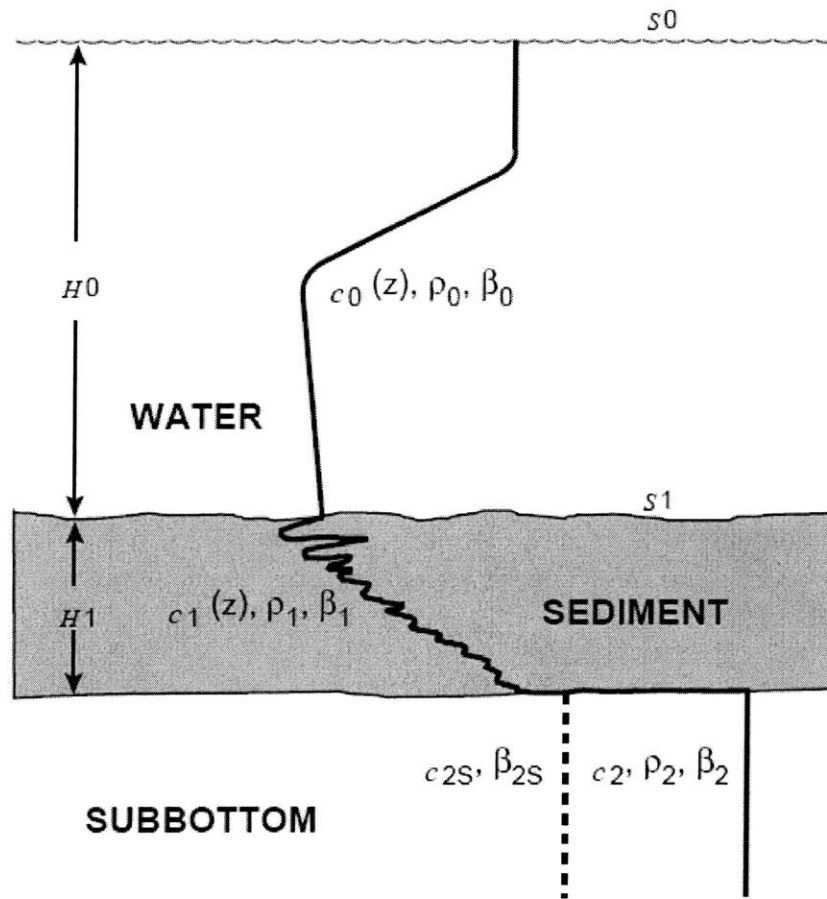
Figure 2-4: Propagation media handled by C-SNAP.
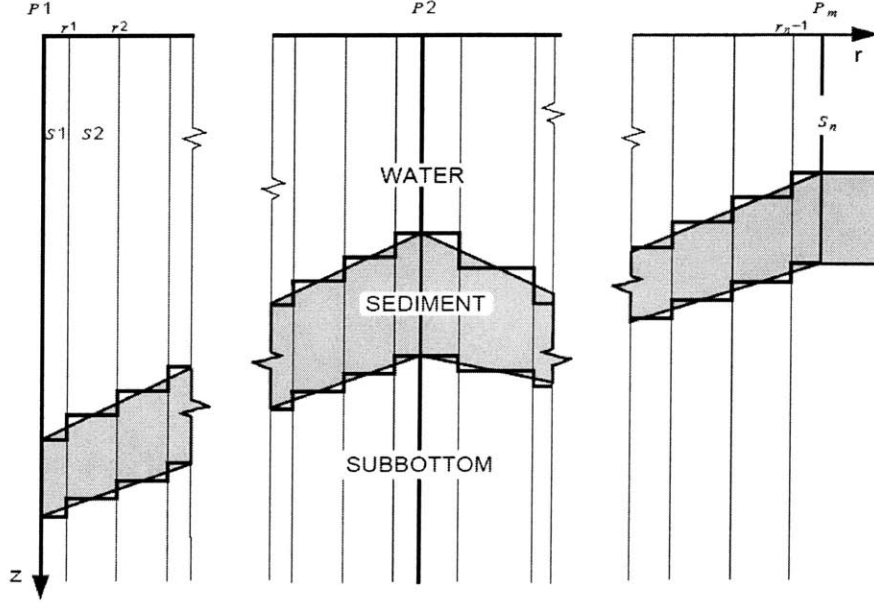
Figure 2-5: Stair step approximation of sloping bottom environment.

2.4 An Approximate Two-Way Model

From section 2.3, we know C-SNAP is a one-way coupled modes model, with impedance matching to preserve accuracy. We may approximate a two-way coupled modes model based on C-SNAP.

2.4.1 Introduction

We take two steps to build an approximate two-way model. In the first step, we march forward with single-scatter approximation; in the second step, beginning with the backscattered component from the rightmost interface, we march backward with one-way approximation. Each time an interface is crossed, the new mode amplitude **b** is added to the old one generated by the single-scatter matching in the first step, and the sum is used to carry on the backward propagation until the source region is reached. Refer to Fig. 2-6.

In the approximate two-way model, we use the left interface to normalize $H1$ function, while use the right interface to normalize $H2$ function. With this normalization

80
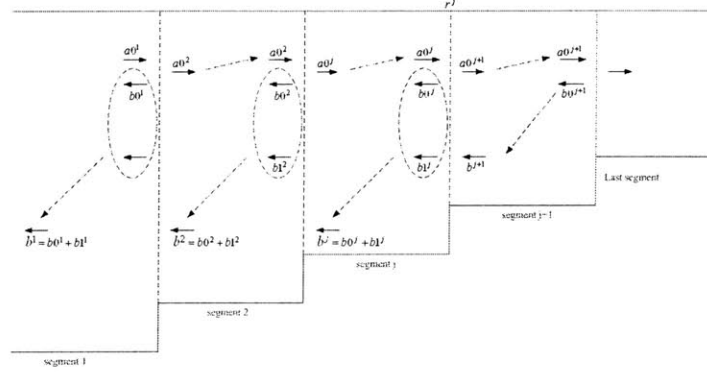
Figure 2-6: Illustration of an approximate two-way coupled modes model.

of $H1$ and $H2$ functions, the outgoing and incoming decaying modes are illustrated in Fig. 2-7.
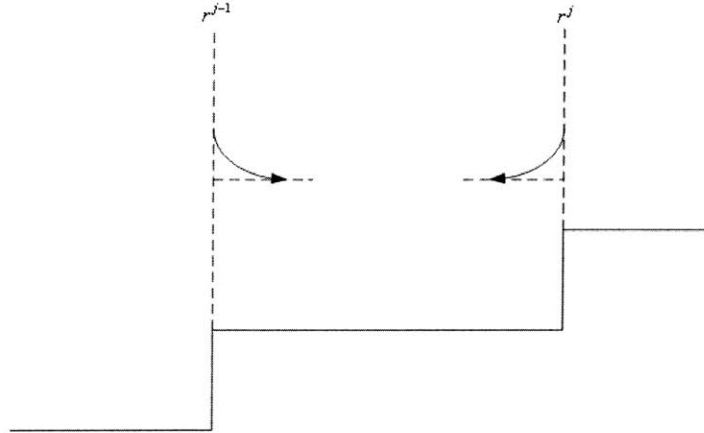
Figure 2-7: Outgoing and incoming decaying modes with $H1$ normalized at the left interface while $H2$ normalized at the right interface.

Thus the field in segment j is represented as

$$p^j(r,z) = \sum_m [a_m^j H1_m^j(r) + b_m^j H2_m^j(r)] \Psi_m^j(z) \tag{2.73}$$

where

$$\begin{cases} H1_m^j(r) = \sqrt{\dfrac{r^{j-1}}{r}} e^{ik_{rm}^j(r-r^{j-1})} \\ H2_m^j(r) = \sqrt{\dfrac{r^j}{r}} e^{-ik_{rm}^j(r-r^j)} \end{cases} \quad \text{for point source} \tag{2.74}$$

81

or

$$\begin{cases} H1_m^j(r) = e^{ik_{rm}^j(r-r^{j-1})} \\ H2_m^j(r) = e^{-ik_{rm}^j(r-r^j)} \end{cases} \qquad \text{for line source} \qquad (2.75)$$

2.4.2 Formulas of Single-Scatter Approximation in the Forward Marching Process

With the new normalization method, the results of the single-scatter approximation in the forward marching process are presented below (Refer to Fig. 2-8).
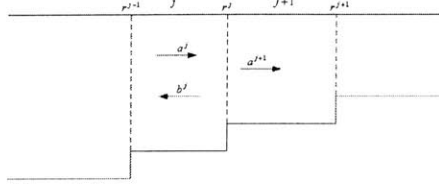
Figure 2-8: Geometry for forward marching process.

After imposing continuity of pressure and continuity of radial particle velocity at the interface between segment j and segment $j+1$, i.e., at $r = r^j$, we get

$$\begin{cases} \boldsymbol{b}^j = -(\boldsymbol{C}_a^j + \boldsymbol{C}_b^j)^{-1}(\boldsymbol{C}_a^j - \boldsymbol{C}_b^j)\boldsymbol{H}1^j(r^j)\boldsymbol{a}^j \\ \boldsymbol{a}^{j+1} = \frac{1}{2}(\boldsymbol{C}_a^j + \boldsymbol{C}_b^j)\boldsymbol{H}1^j(r^j)\boldsymbol{a}^j + \frac{1}{2}(\boldsymbol{C}_a^j - \boldsymbol{C}_b^j)\boldsymbol{b}^j \end{cases} \qquad (2.76)$$

where

$$C_a^j[l,m] = \int \frac{1}{\rho^{j+1}(z)}\Psi_l^{j+1}(z)\Psi_m^j(z)\mathrm{d}z \qquad (2.77)$$

$$C_b^j[l,m] = \frac{k_{rm}^j}{k_{rl}^{j+1}} \int \frac{1}{\rho^j(z)}\Psi_l^{j+1}(z)\Psi_m^j(z)\mathrm{d}z \qquad (2.78)$$

and the initial mode amplitude is

$$\boldsymbol{a}^1 = \boldsymbol{d},$$

where

$$d_m = \begin{cases} \frac{i}{4\rho(z_s)}\Psi_m^1(z_s)H_0^{(1)}(k_{rm}^1 r^1), & \text{for point source} \\ \frac{i}{2\rho(z_s)}\Psi_m^1(z_s)\frac{e^{ik_{xm}^1 x^1}}{k_{xm}^1}, & \text{for line source} \end{cases}$$

82

2.4.3 Formulas of One-Way Approximation in the Backward Marching Process

We apply one-way approximation in the backward marching process (Refer to Fig. 2-9). After imposing continuity of pressure and continuity of radial particle velocity at
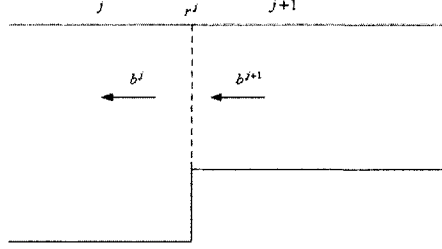
Figure 2-9: Geometry for one-way approximation.

the interface between segment j and segment $j + 1$, i.e., at $r = r^j$, we get

$$b^j = \frac{1}{2}(C_c^{j+1} + C_d^{j+1}) \cdot H2^{j+1}(r^j) \cdot b^{j+1}$$

where

$$C_c^{j+1}[l, m] = \int \frac{1}{\rho^j(z)} \Psi_l^j(z) \Psi_m^{j+1}(z) \mathrm{d}z$$

$$C_d^{j+1}[l, m] = \frac{k_{rm}^{j+1}}{k_{rl}^j} \int \frac{1}{\rho^{j+1}(z)} \Psi_l^j(z) \Psi_m^{j+1}(z) \mathrm{d}z$$

2.4.4 Modify C-SNAP to an Approximate Two-Way Model

The original C-SNAP has three matching options, i.e., pressure matching (MATCH 1), reduced-pressure matching (MATCH 2) and impedance matching (MATCH 3). We add to C-SNAP the fourth matching option, i.e., MATCH 4, which includes a forward marching process applying single-scatter approximation followed by a backward marching process applying one-way approximation, and gives an approximate two-way result.

Appendix E contains some of the notifications we took when we modified the one-way C-SNAP to a two-way coupled modes model.

2.5 Numerical Examples

The issue of establishing reference solutions for range-dependent ocean acoustic problems was addressed within the Acoustic Society of America (ASA). Special sessions at two consecutive ASA meetings were dedicated to this problem, and relevant benchmark problems were identified and solved([13]).

What we present in this part are solutions of several problems generated with the two-way C-SNAP code and comparison with other numerical codes, for example, COUPLE.

2.5.1 Propagation in an Ideal Waveguide

As indicated schematically in Fig. 2-10, the waveguide consists of a 200 m water layer bounded above by a pressure-release surface and below by a rigid bottom. The source is located at 100 m and the receiver is located at 100 m. The frequency is 50 Hz. We may obtain the analytical result from the formulas in section 1.3.1. The analytical result and result by two-way C-SNAP (MATCH 4) are shown in Fig. 2-11. The input file for C-SNAP is listed in Appendix H.

As seen from Fig. 2-11, the accuracy control[1] should be set to the highest level (NMESH 4) to obtain an accurate result for ideal problems. Otherwise (NMESH 1, 2 or 3), the eigenvalues computed by C-SNAP are not accurate enough.

---

[1]NMESH arg [10]: Number of subsequent meshes used to refine the wavenumbers. To get a reasonable balance between execution time and accuracy the default choice for NMESH is 1, as in most cases the solution obtained from a single mesh is already sufficiently accurate. A good choice for higher accuracy is "NMESH 4". The ratio between the number of mesh points in any two consecutive meshes is roughly 1/3. Consequently, a ratio of 2 will exist between the first and fourth mesh.
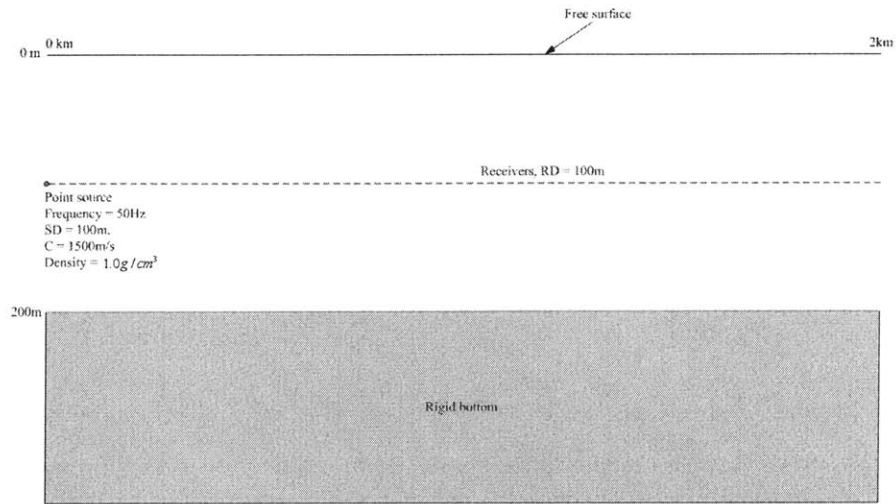
Figure 2-10: Flat geometry for ideal problem.
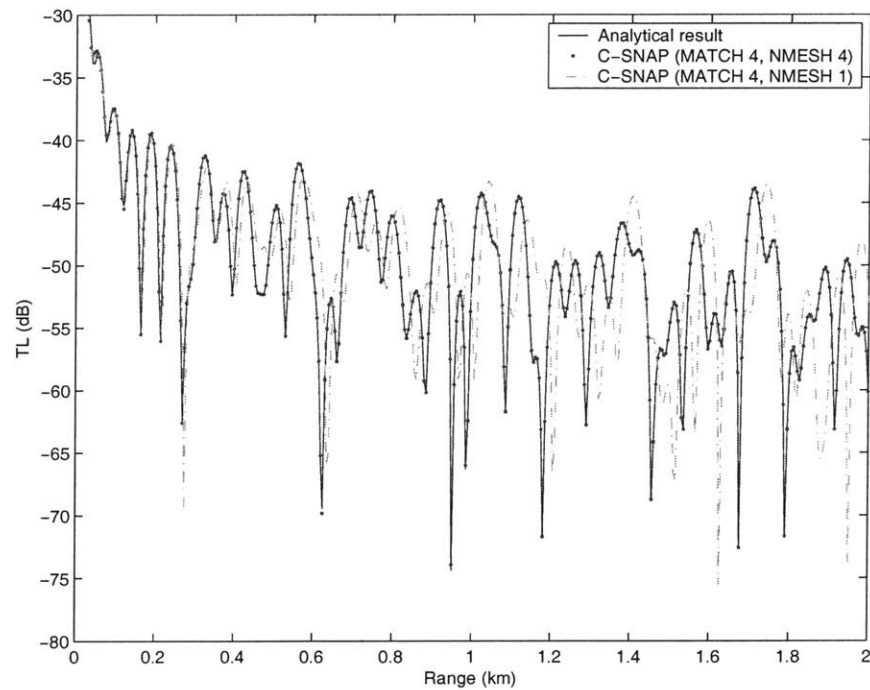
Figure 2-11: Comparison of analytical result and result by C-SNAP with NMESH 1 and NMESH 4.

85

2.5.2   Propagation in a Waveguide with a Cosine-Bell Shaped Ridge

In this example, the computations were based on a cosine-bell shaped ridge described by a simple cosine-bell([6]),

$$
\zeta(x) = \begin{cases} (a/2)[1 + \cos{(2\pi(x - x_0)/w)}], & |x - x_0| < w/2 \\ 0, & |x - x_0| > w/2 \end{cases} \tag{2.79}
$$

where a is the height and w is the width of the ridge. We choose $a = 50$ m, $w = 100$ m and $x_0 = 250$ m in this example. The constant sound-speed in water is 1470 m/s. The bottom is rigid, with initial depth 200 m. We compute propagation loss for a 25 Hz line source in plane geometry located 250 m away from the center of the ridge and the source depth is 30 m. The geometry of this example is illustrated in Fig. 2-12.
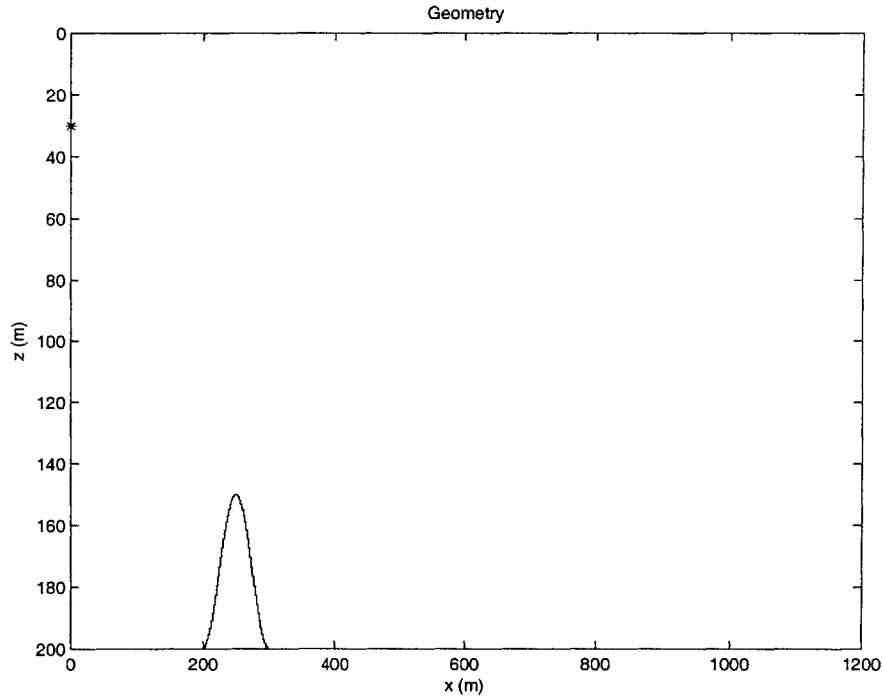
Figure 2-12: Geometry of the cosine-bell shaped ridge problem.

This problem requires accurate representation of the near field, which means we

must include many evanescent modes. Due to the problem of stability, we apply the analytical solutions for eigenvalue and eigenfunction in our two-way model described in section 2.4. The results from one-way model (single-scatter) and two-way model are shown in Fig. 2-13. In Fig. 2-13(b), interference between incident and backscattered fields is clearly visible in the region between the source and the ridge.

(a)   (b)
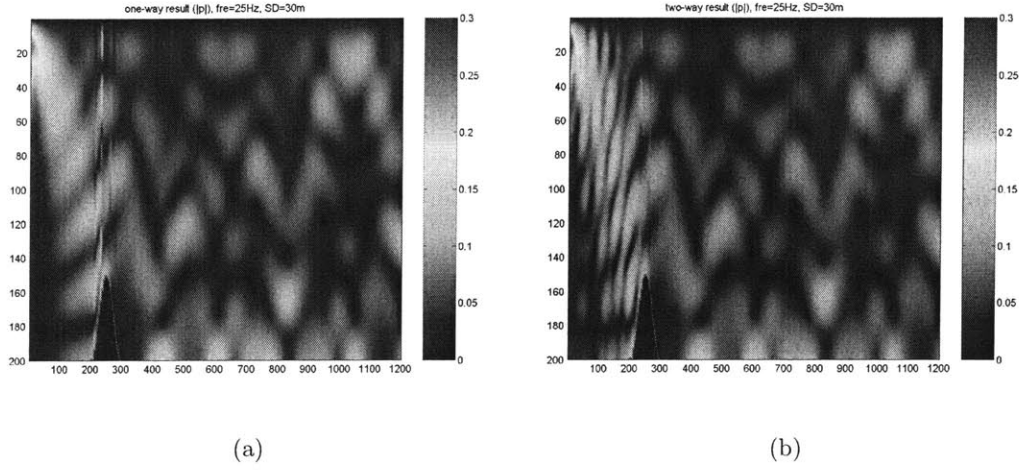
Figure 2-13: Transmission loss for cosine-bell shaped ridge problem from (a) one-way (single-scatter) (b) two-way.

2.5.3   Upslope Propagation in a Wedge-Shaped Waveguide

As one of the ASA benchmark problems, the geometry for the wedge problem is given in Table 2.1 and graphically illustrated in Fig. 2-14. The environment consists of a homogeneous water column ($c = 1500$ m/s, $\rho = 1.0$ g/cm^3) limited above by a pressure-release flat sea surface and below by a sloping sea floor. The water depth at the source position is 200 m decreasing to zero at a distance of 4 km from the source with a slope of approximately 2.86^o. Accurate field solutions are sought for a 25 Hz source placed at middepth (100 m) and for two receivers at 30 m and 150 m depth, respectively. As seen from Fig. 2-14, the selected depths provide samples of the acoustic field in the water column as well as in the bottom. The points in range where the two receivers cross the water/bottom interface is 3.4 km for the shallow receiver and 1.0 km for the deep receiver.

Table 2.1: Benchmark problems associated with a wedge-shaped waveguide.

1. BENCHMARK WEDGE PROBLEMS

Accurate solutions are invited for upslope acoustic propagation in a wedge with the geometry described below. The parameters of the problem are listed below, including a three choices of bottom boundary condition (pressure release, case I and two penetrable bottoms, case II and III). The wedge geometry is shown in Fig. 2-14. Parameters common to all three cases.

wedge angle $\theta_0 = 2.86°$
frequency $f = 25$ Hz
isovelocity sound speed in water column $c_1 = 1500$ m/s
source depth $= 100$ m
source range from the wedge apex $= 4$ km
water depth at source position $= 200$ m
pressure-release surface

Case I: pressure-release bottom.
This problem should be done for a line source parallel to the apex i.e., 2-D geometry.

Case II: penetrable bottom with zero loss.
sound speed in the bottom $c_2 = 1700$ m/s
density ratio $\rho_2/\rho_1 = 1.5$
bottom attenuation $= 0$ dB/λ

This problem should be done for a point source in cylindrical geometry.
Case III: penetrable lossy bottom.

As in case II except with bottom loss $= 0.5$ dB/λ.

OUTPUT

Plots should be presented on overhead transparencies of propagation loss versus range measured from the source to the apex. The scaling should be as shown. It is important to conform to this format for the purpose of comparison. The dB scale of propagation loss should cover exactly 50 dB. The start and end points of this 50-dB scale should be chosen to ensure that the results are entirely contained in the plot. Propagation loss is defined for the present purpose as

$$PL = -10\log_{10} \frac{\text{(Intensity at a field point)}}{\text{(Intensity at one meter away from source)}}$$

Receiver depths
Case I: 30 m
Case II and case III: 30 and 150 m

Free surface

0   1   2   3   4 km

Pressure receivers   30 m

100 m

150 m c_1 = 1500 m/s
                ρ_1 = 1 g/cm^3

CW
25 Hz
Source

Pressure receivers

2.86° c_2 = 1700 m/s
200   ρ_2 = 1.5 g/cm^3
m β_2 = 0.5 dB/λ
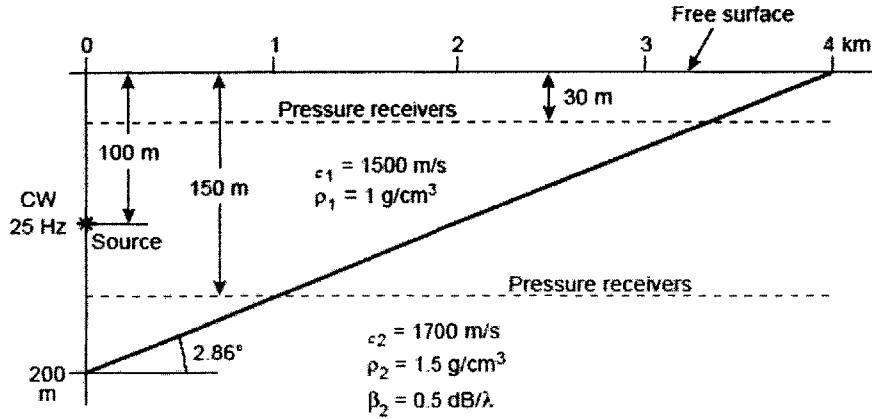
Figure 2-14: Wedge geometry for test problems 1, 2 and 3.

Three different bottom boundary conditions are considered:

Case 1: Perfectly reflecting pressure-release bottom. This is an idealized wedge problem for which an independent reference solution can be formulated. The problem should be solved in plane geometry (line source) with a radiation condition applied at the left boundary.

Case 2: Penetrable lossless bottom. This is a slightly idealized ocean acoustic problem where attenuation in the bottom has been neglected. The bottom is a homogeneous fluid half-space with a compressional speed of 1700 m/s and a density of 1.5 g/cm^3. As is customary in ocean acoustics, this problem should be solved for a point source in cylindrical geometry.

Case 3: Penetrable lossy bottom. This is a more realistic ocean acoustic problem where a wave attenuation of 0.5 dB/λ in the bottom has been included. Otherwise parameters are the same as in case 2.

Case 3 is the most realistic ocean acoustic problem (lossy penetrable bottom). However, some numerical codes only handle lossless media, and case 2 (lossless penetrable bottom) was therefore included as an alternative test problem. Case 1 (perfectly reflecting bottom) was chosen simply because an analytic reference solution can be formulated for the pressure-release wedge. Moreover, since sound propagating towards the wedge apex will be completely backscattered due to the reflecting bound-

89

aries, this test problem is an ideal benchmark for a full two-way solution of the wave equation.

CASE 1: WEDGE WITH PRESSURE RELEASE BOUNDARIES

Buckingham and Tolstoy ([4]) presented an analytical solution for this ideal problem (See Appendix G), we may use that analytical solution as a reference.

Instead of trying to figure out the correct handling of the pressure-release bottom boundary condition for C-SNAP, we apply a Matlab code to fulfill the approximate two-way method described in section 2.4, in which we use the analytical expressions for eigenvalue and eigenfunction as in section 1.3.2. Fig. 2-15(a) shows the transmission loss calculated by the approximate two-way method, compared with the reference provided by Buckingham and Tolstoy ([4]). Fig. 2-15(b) shows an extended view of the field in Fig. 2-15(a) over the range 0-1 km. From Fig. 2-15 we can see the two-way C-SNAP results are in excellent agreement with the reference solutions by Buckingham and Tolstoy ([4]).

(a)   (b)
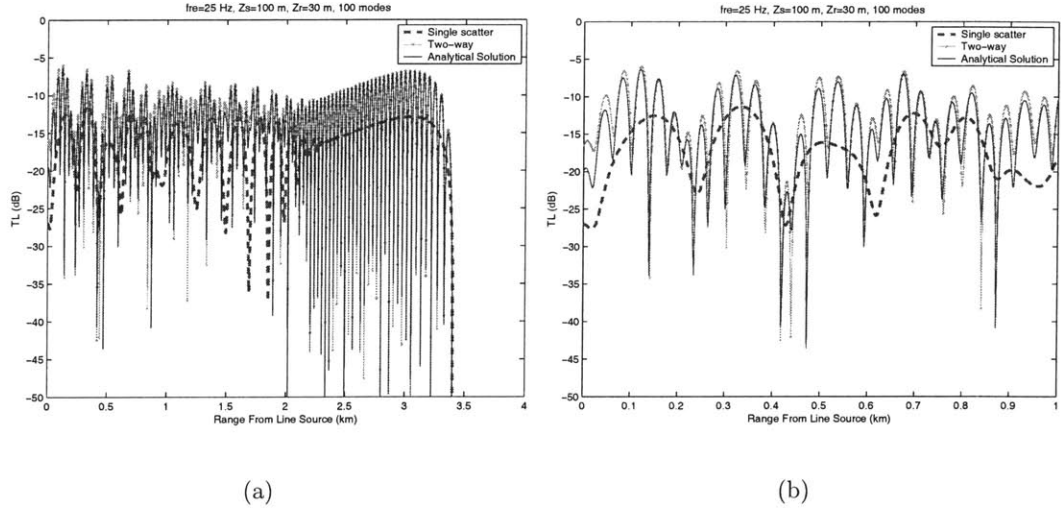
Figure 2-15: Transmission loss for benchmark problem 1 case 1, for a receiver depth of 30 m and frequency of 25 Hz from (a) 0-4 km (b) 0-1 km.

90

CASE 2: WEDGE WITH PENETRABLE LOSSLESS BOTTOM

Test case 2 is a wedge-shaped homogeneous ocean (1500 m/s) overlying a homoge-
neous fast bottom with a speed of 1700 m/s, a density of 1.5 g/cm^3, and an attenua-
tion of 0.0 dB/λ. These bottom properties result in perfect reflection for waterborne-
energy incident at angles up to the critical angle of 28° (discrete mode spectrum),
while energy incident at steeper angles (continuous mode spectrum) is subject to in-
creasing reflection loss with angle, with a maximum loss of approximately 12 dB per
bounce at normal incidence.

Fig. 2-16 shows the solution of one-way C-SNAP (MATCH 3) and that of two-
way C-SNAP (MATCH 4). From Fig. 2-16 we see one-way C-SNAP and two-way
C-SNAP give almost the same results in this case. Fig. 2-17 shows the solution of
two-way C-SNAP (MATCH 4) and that of COUPLE. In this case, both C-SNAP
and COUPLE compute 90 modes, 3 proper discrete modes and 87 improper modes.
The comparison of COUPLE and C-SNAP results without attenuation loss from the
sediment layer shows excellent results for both receiver depth at 30 m and receiver at
150 m. The input files of C-SNAP and COUPLE are listed in Appendix I.

(a)   (b)
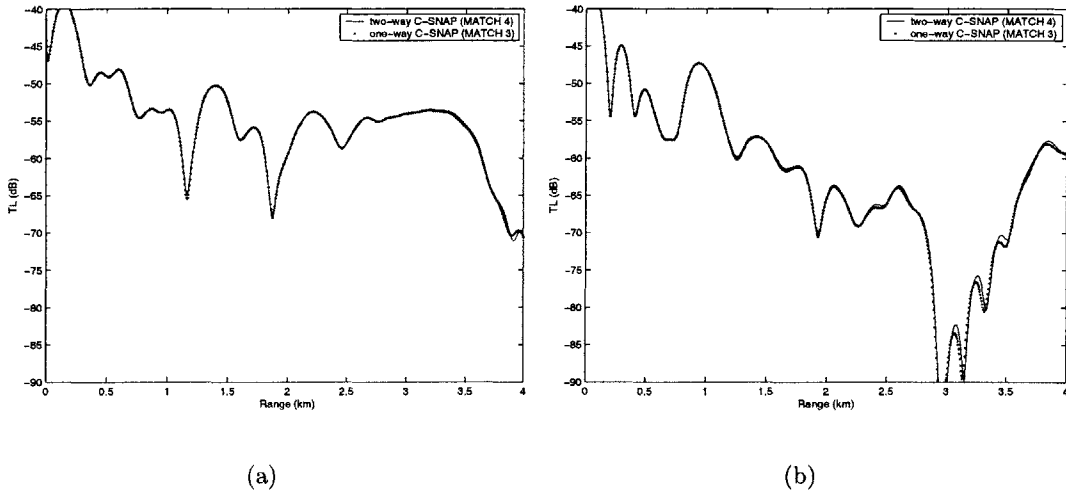
Figure 2-16: Comparison of result from one-way C-SNAP with impedance matching
(MATCH 3) and two-way C-SNAP (MATCH 4) for problem 1 case 2 (a) receiver at
30 m (b) receiver at 150 m.

(a)   (b)
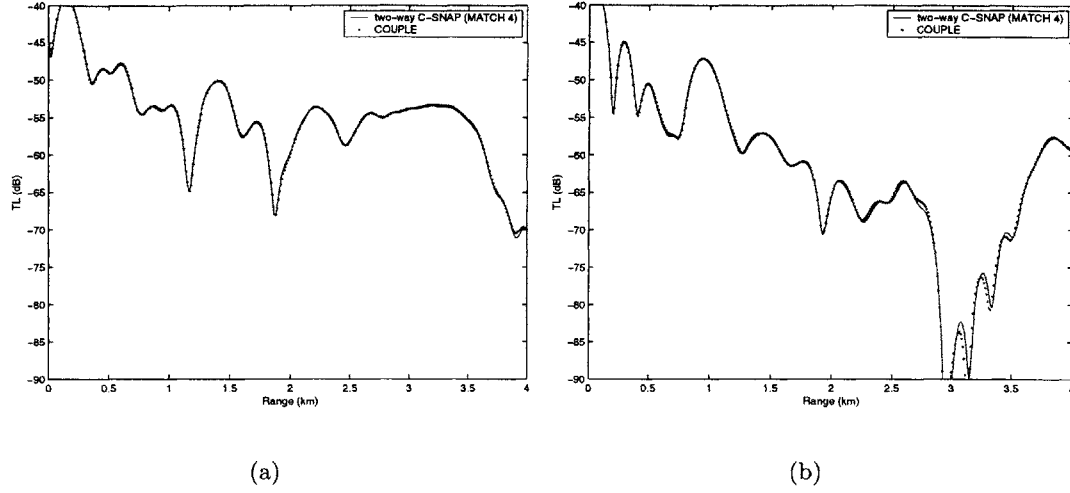
Figure 2-17: Comparison of result from two-way C-SNAP (MATCH 4) and COUPLE for problem 1 case 2 (a) receiver at 30 m (b) receiver at 150 m.

CASE 3: WEDGE WITH PENETRABLE LOSSY BOTTOM

This is a more realistic ocean acoustic problem where a bottom attenuation of 0.5 dB/λ has been included. Otherwise, the parameters are the same as in Case 2.

Stable numerical results were obtained by including 90 modes and by subdividing the slope into 200 stair steps. Fig. 2-18 shows the results from one-way C-SNAP with impedance matching (MATCH 3) and from two-way C-SNAP (MATCH 4). They are almost the same in this case. Two-way C-SNAP (MATCH 4) solutions for case 3 are compared with COUPLE results in Fig. 2-19.

The propagation loss plots for the two receivers presented in Fig. 2-19 show excellent results for the receiver at 30 m but not as good for the receiver at 150 m. This fact is explained in [10] as below:

- (in C-SNAP)The eigenfunctions are obtained through algorithms which use real arithmetic and their solution becomes approximate in the presence of loss. To get the exact solution, complex calculations should be used instead, at the expense of a less robust algorithm and more CPU time.

- While the influence of bottom loss on the waterborne modes is practically insignificant (water is a relatively low loss region), the opposite occurs for the

92

bottom-bounce modes as they have a large oscillatory size in the bottom layer. Though these bottom-bounce modes usually carry little energy, they are essential for mode coupling. The effect of inaccurate bottom-bounce modes in range-independent environments is rarely observed as no mode coupling is required and these modes decay rapidly out in range.

- While the 30 m receiver hits the bottom only at a range of 3.4 km, the 150 m receiver will lie in the sediment (lossy layer with the pressure field represented by the bottom-bounce modes) starting at at a range of 1 km, which is exactly the range where the agreement deteriorates.

The input files of C-SNAP and COUPLE are listed in Appendix J.

(a)   (b)
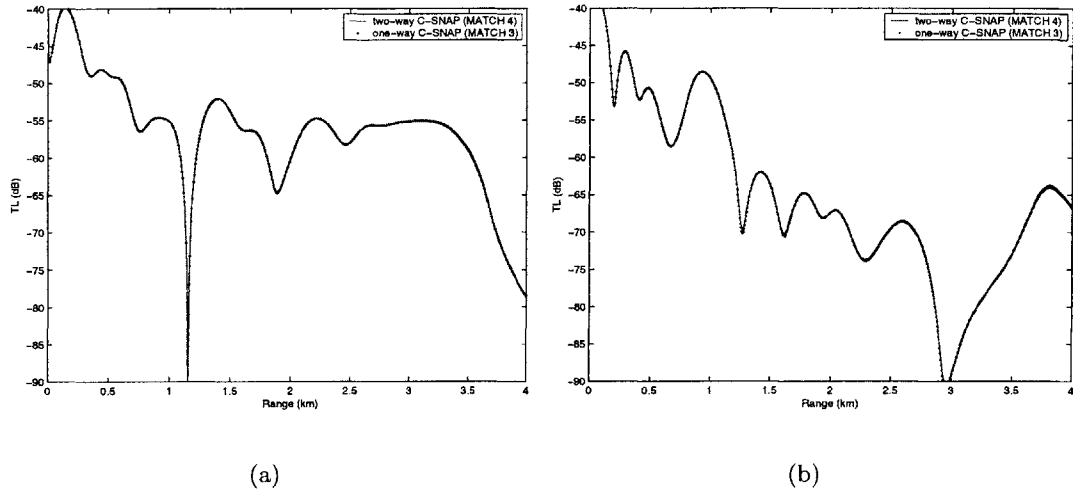
Figure 2-18: Comparison of result from one-way C-SNAP with impedance matching (MATCH 3) and two-way C-SNAP (MATCH 4) for problem 1 case 3 (a) receiver at 30 m (b) receiver at 150 m.

2.5.4 Downslope Propagation in a Wedge-Shaped Waveguide

The geometry of this problem is illustrated in Fig. 2-20. The initial water depth is 100 m and increases linearly to 1000 m at a range of 4 km, resulting in a downslope wedge with an angle of 12.7^o. The sound speed in the water column is 1500 m/s, while in the bottom the sound speed is 1700 m/s, the density is 2 g/cm^3 and the

93

(a)   (b)
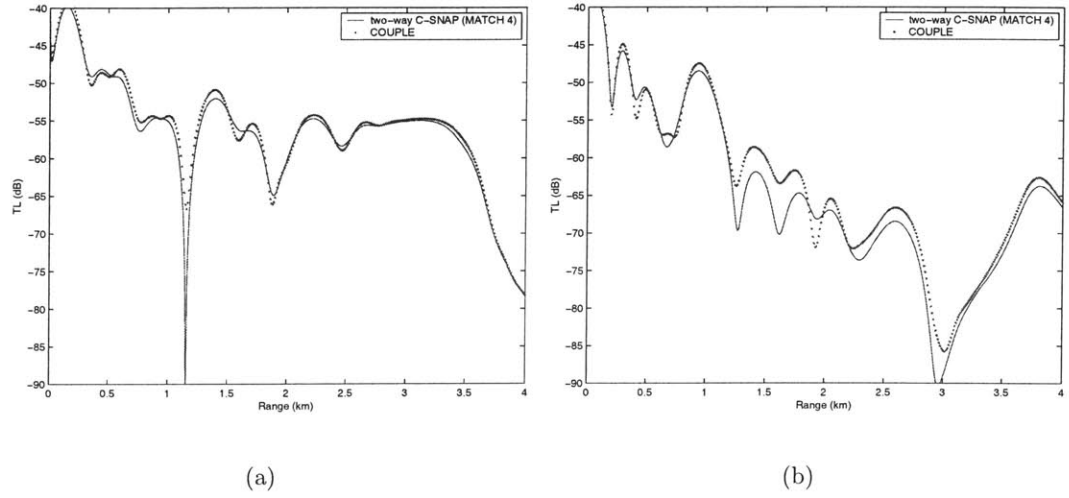
Figure 2-19: Comparison of result from two-way C-SNAP (MATCH 4) and COUPLE for problem 1 case 3 (a) receiver at 30 m (b) receiver at 150 m.

attenuation is 0.5 dB/λ. We compute propagation loss for a 25 Hz line source in plane geometry located at 50 m depth. We introduce a false-bottom at depth 4000 m, and allow for a maximum of 160 modes in the propagation field.
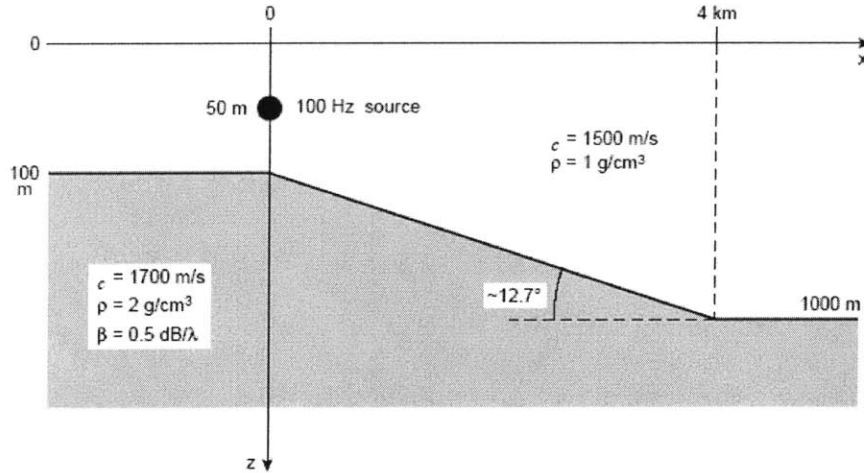
Figure 2-20: Wedge geometry for downslope propagation.

We illustrate in Fig. 2-21 the comparison of the propagation loss over the water column obtained from one-way C-SNAP with impedance matching (MATCH 3) and two-way C-SNAP (MATCH 4). The difference between one- and two-way C-SNAP

94

results is seen to be approximately 2 dB from range 0.5 km to 2.5 km. The input file
for two-way C-SNAP is listed in Appendix K.
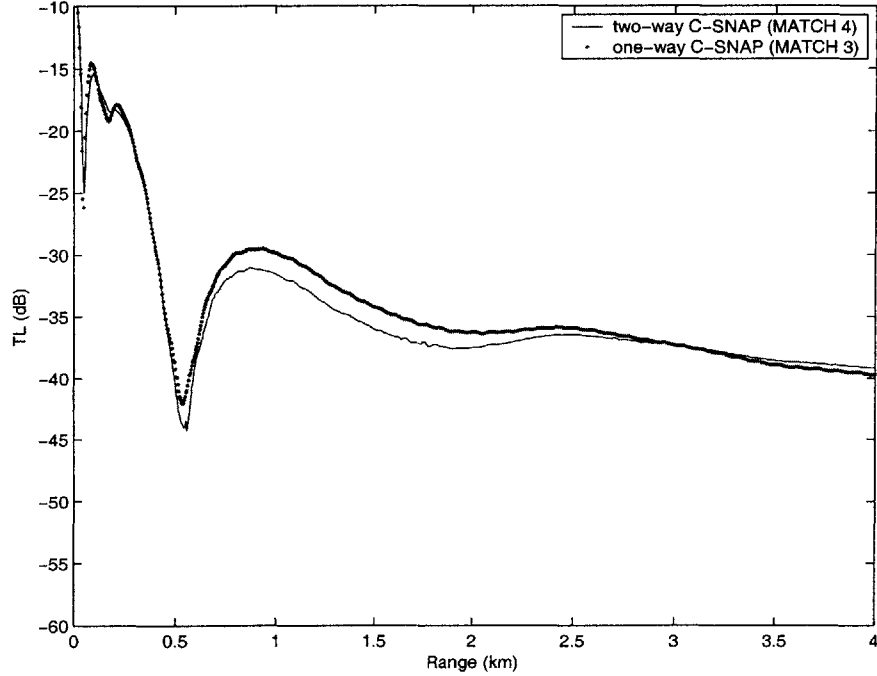
Figure 2-21: Coupled mode results for the $12.7°$ wedge from two-way C-SNAP
(MATCH 4) and one-way C-SNAP with impedance matching (MATCH 3).

2.5.5 Deep Water Propagation over a Seamount

Here we test the model along a 200 km deep-water track where the range dependence
is obtained through a combination of upslope and downslope environments so as to
build an idealized seamount. The environment is illustrated in Fig. 2-22. The initial
water depth is 5000 m. The seamount is located around 100 km away from the source,
with a width of 40 km and a height of 1000 m. The source depth is 100 m and the
frequency is 50 Hz.

We limit in this problem the modal starting field to retain only those modes which
are water borne. The contoured propagation losses versus depth and range is shown
in Fig. 2-23(a). The result for a single source/receiver combination is shown in Fig. 2-
23(b). From Fig. 2-23(b) we see the one- and two-way C-SNAP results are almost
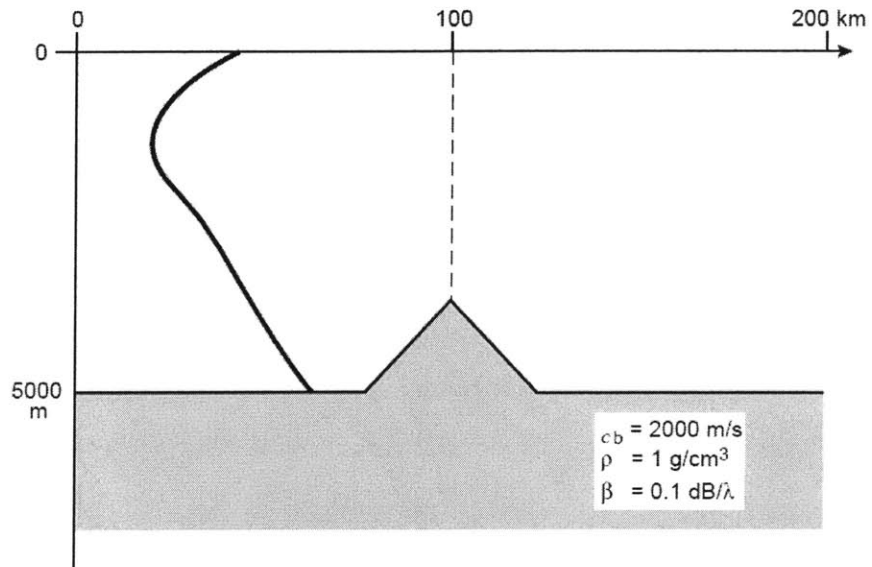
Figure 2-22: Schematic of the seamount problem.

the same in this case. The input file for Fig. 2-23(a) from the two-way C-SNAP is
listed in Appendix L.
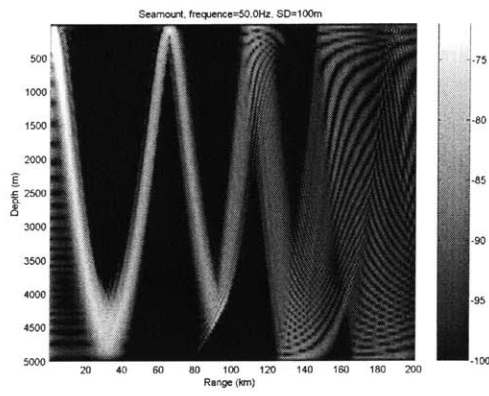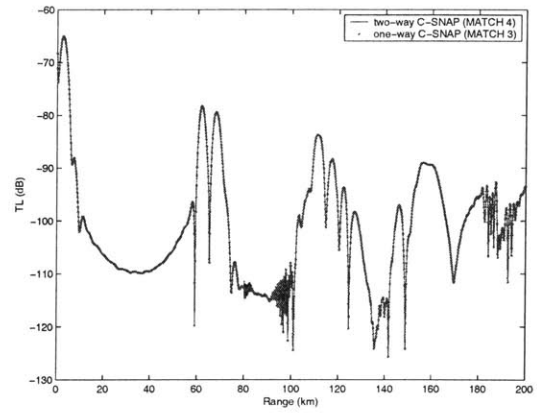
(a)   (b)

Figure 2-23: Transmission losses of the seamount problem (a) Two-way C-SNAP filed versus depth and range for the seamount problem (b) Coupled mode results for the seamount problem from two-way C-SNAP (MATCH 4) and one-way C-SNAP with impedance matching (MATCH 3).

Chapter 3

Three-Dimensional Scattering in a Two-Dimensional Waveguide

In Chapter 2, we developed a two-way coupled modes model, which can handle two-dimensional problems involving a point or line source. In this chapter, we extend the two-way coupled modes model to three-dimensional problems involving a point source in a waveguide in which the acoustic properties vary with depth and range (one of the horizontal Cartisian coordinates). Problem of this type are representative of backscattering from extended features such as ridges. Sketch of the basic waveguide for this problem is shown in Fig. 3-1. After Fourier transforming out the cross range (the other horizontal coordinate), the three-dimensional wave equation reduces to a two-dimensional wave equation in which the wave number depends on the separation constant.

Several methods have been developed for this problem. For example, Fawcett and Dawson([9]) presented a model using boundary integral equation method (BIEM), Orris and Collins([18]) presented a model using parabolic equation (PE) method, etc.

3.1 Theory

Following the derivation in ([9]), we work in Cartesian coordinates $x = (x, y, z)$, where x is the range, y is the cross range, and z is the depth below the ocean surface. The
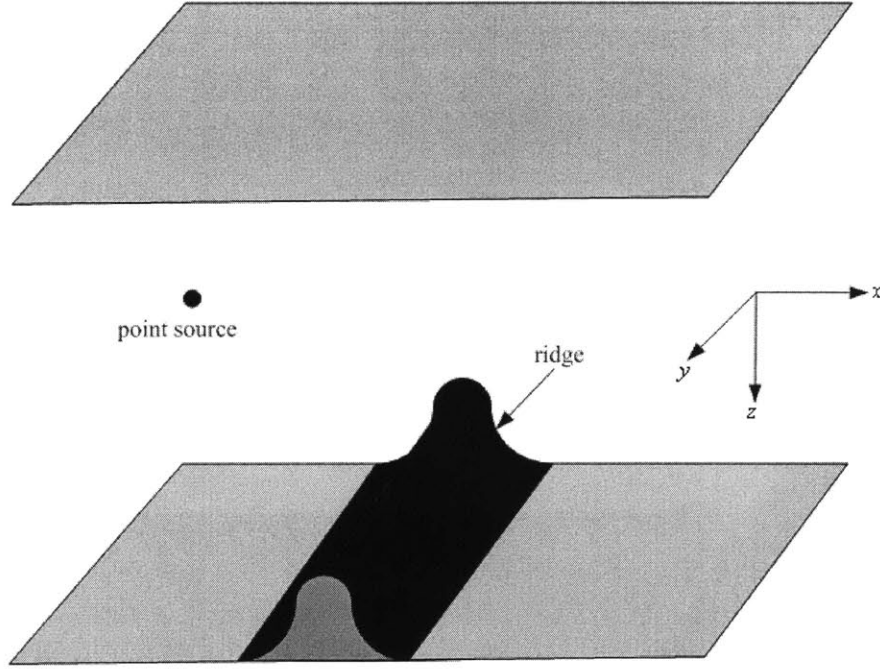
Figure 3-1: Sketch of the basic waveguide model.

sound speed c, density ρ, and attenuation β are assumed to vary with x and z but not y, i.e., the waveguide is two-dimensional.

The Fourier transform pair

$$\tilde{p}(x, k_y, z) = \int_{-\infty}^{\infty} p(x, y, z)e^{iyk_y}\mathrm{d}y, \tag{3.1}$$

$$p(x, y, z) = \frac{1}{2\pi} \int_{-\infty}^{\infty} \tilde{p}(x, k_y, z)e^{-iyk_y}\mathrm{d}k_y, \tag{3.2}$$

will be used in developing our three dimensional model.

The three dimensional Helmholtz equation is

$$\frac{\partial^2 p}{\partial x^2} + \frac{\partial^2 p}{\partial y^2} + \frac{\partial^2 p}{\partial z^2} + \frac{\omega^2}{c^2}p = -\delta(x - x_s)\delta(y - y_s)\delta(z - z_s), \tag{3.3}$$

where $\boldsymbol{x_s} = (x_s, y_s, z_s)$ is the location of the point source.

Apply operator $\int_{-\infty}^{\infty}(\cdot)e^{iyk_y}dy$ to Eq. (3.3). Since from Eq. (3.1), we have

$$\frac{\partial^2 \tilde{p}}{\partial x^2} = \frac{\partial^2}{\partial x^2}\int_{-\infty}^{\infty} p e^{iyk_y}dy$$

$$= \int_{-\infty}^{\infty} \frac{\partial^2 p}{\partial x^2}e^{iyk_y}dy,$$

similarly, we have

$$\frac{\partial^2 \tilde{p}}{\partial z^2} = \int_{-\infty}^{\infty} \frac{\partial^2 p}{\partial z^2}e^{iyk_y}dy.$$

While from Eq. (3.2), we have

$$\frac{\partial^2 p}{\partial y^2} = \frac{1}{2\pi}\frac{\partial^2}{\partial y^2}\int_{-\infty}^{\infty} \tilde{p}e^{-iyk_y}dk_y$$

$$= \frac{1}{2\pi}\int_{-\infty}^{\infty} \tilde{p}(-ik_y)^2 e^{-iyk_y}dk_y$$

$$= \frac{1}{2\pi}\int_{-\infty}^{\infty} \tilde{p}(-k_y^2)e^{-iyk_y}dk_y,$$

which leads to

$$-k_y^2\tilde{p} = \int_{-\infty}^{\infty} \frac{\partial^2 p}{\partial y^2}e^{iyk_y}dy.$$

Thus, after transforming, Eq. (3.3) becomes

$$\frac{\partial^2 \tilde{p}}{\partial x^2} + \frac{\partial^2 \tilde{p}}{\partial z^2} + (\frac{\omega^2}{c^2} - k_y^2)\tilde{p} = -\delta(x - x_s)\delta(z - z_s)e^{iy_s k_y}. \qquad (3.4)$$

For simplicity, we assume $x_s = y_s = 0$.

For each specified value of k_y, Eq. (3.4) is a two dimensional Helmholtz equation with a line source, the equivalent wavenumber[1] is

---

[1]We notice that k_{zm}, $\Psi_m(z)$ are independent of k_y. This is because the depth-dependent problem,

$$\left\{ \begin{array}{l} \frac{d^2\Psi_m(z)}{dz^2} + k_{zm}^2\Psi_m(z) = 0 \\ \text{B.C.} \end{array} \right. \qquad (3.5)$$

is independent of k_y.

101

$$k'^2 = \frac{\omega^2}{c^2} - k_y^2$$

$$= (k_{xm}^2 + k_y^2 + k_{zm}^2) - k_y^2$$

$$= k_{xm}^2 + k_{zm}^2. \tag{3.6}$$

From section 1.6, we know the solution for Eq. (3.4) is

$$\tilde{p}(x, k_y, z) = \frac{i}{2\rho(z_s)} \sum_m \Psi_m(z_s) \Psi_m(z) \frac{e^{ik_{xm}x}}{k_{xm}}$$

$$k_{xm}^2 = k'^2 - k_{zm}^2 = \frac{\omega^2}{c^2} - k_y^2 - k_{zm}^2 = k_{xm}^{(0)\,2} - k_y^2$$

$$= \frac{i}{2\rho(z_s)} \sum_m \Psi_m(z_s) \Psi_m(z) \frac{e^{i\sqrt{k_{xm}^{(0)\,2} - k_y^2}}}{\sqrt{k_{xm}^{(0)\,2} - k_y^2}}. \tag{3.7}$$

where $k_{xm}^{(0)\,2} = \frac{\omega^2}{c^2} - k_{zm}^2$ are the eigenvalues of the two-dimensional problem ($k_y = 0$).

After the pressure $\tilde{p}(x, k_y, z)$ has been computed for a sequence of k_y values, the solution $p(x, y, z)$ can be computed from the inverse Fourier transform Eq. (3.2),

$$p(x, y, z) = \frac{1}{2\pi} \int_{-\infty}^{\infty} \tilde{p}(x, k_y, z) e^{-iyk_y} dk_y. \tag{3.8}$$

From Eq. (3.7), we can see the integrand of Eq. (3.8) is singular at $k_y^2 = k_{xm}^{(0)\,2}$.

3.2 Implementation of the Numerical Integration of the Inverse Fourier Transform

After the pressure $\tilde{p}(x, k_y, z)$ has been computed for a sequence of k_y values, the solution $p(x, y, z)$ can be computed from the inverse Fourier transform Eq. (3.2). However, the Fourier spectrum $\tilde{p}(x, k_y, z)$ of $p(x, y, z)$ has (integrable) singularities *on the real k_y axis* at the eigenvalues of the two-dimensional problem, i.e., at $k_y^2 = k_{xm}^{(0)\,2}$. In order

102

to use an inverse Fourier transform along the real line, the integral must be sampled very finely in k_y to obtain accurate results. Because of numerical problems associated with integrating through these singularities with the inverse Fourier transform, it will prove advantageous to compute the spectrum for complex values of k_y and use contour integration for the inversion process ([9]). Along such a contour which avoids the singularities in the complex plane, the integrand is analytic, and so more suitable for contour integration.

Specifically, the wave number is taken along the contour C in k_y plane described by the function

$$k_y = s + i\epsilon \tanh(\delta s), \quad -\infty < s < \infty \tag{3.9}$$

where ϵ is a measure of the distance by which the contour avoids the singularities, and δ governs the slope of the contour at the coordinate origin. Contour C is illustrated in Fig. 3-2.
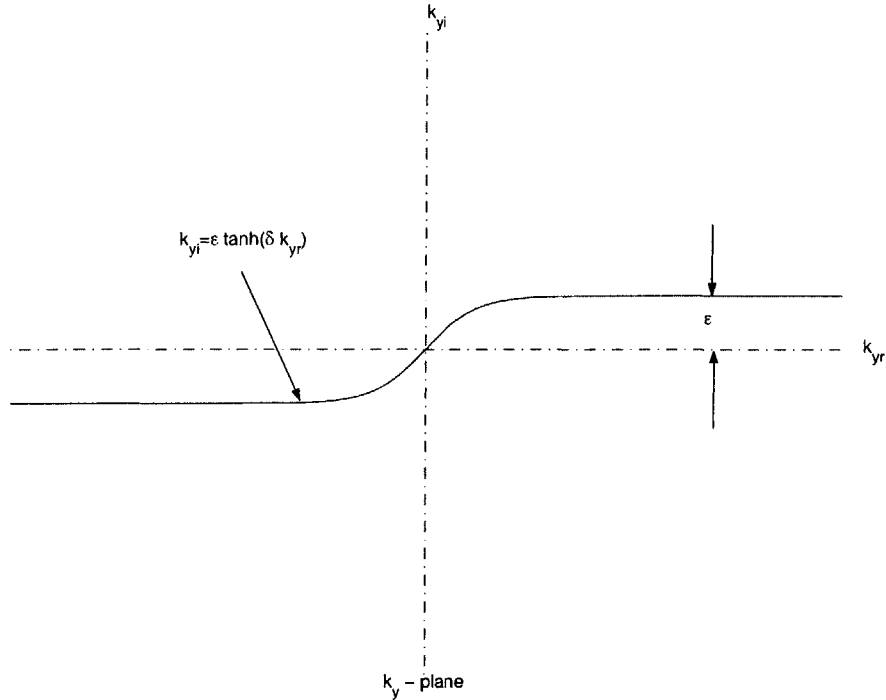
Figure 3-2: Sketch of the integration contour used for the Fourier inversion.

103

From Eq. (3.9), we have

$$\text{Re}\{k_y\} = s, \tag{3.10}$$

$$\text{Im}\{k_y\} = \epsilon \tanh(\delta s), \tag{3.11}$$

so, Eq. (3.9) is equivalent to

$$k_{yi} = \epsilon \tanh(\delta k_{yr}),$$

and

$$\begin{aligned}
\mathrm{d}k_y &= \mathrm{d}s + i\epsilon[\delta \text{sech}^2(\delta s)]\mathrm{d}s \\
&= [1 + i\epsilon\delta \text{sech}^2(\delta s)]\mathrm{d}s, \tag{3.12}
\end{aligned}$$

where we used the formula

$$\tanh'(x) = \text{sech}^2(x).$$

A brief review about the hyperbolic function $\tanh(x)$ is listed in Appendix M.

Thus along contour C, the inverse Fourier transform Eq. (3.2) becomes

$$\begin{aligned}
p(x, y, z) &= \frac{1}{2\pi} \int_{-\infty}^{\infty} \tilde{p} e^{-iyk_y} \mathrm{d}k_y \\
&= \frac{1}{2\pi} \int_{-\infty}^{\infty} \tilde{p}(k_y(s)) e^{-iyk_y(s)}[1 + i\epsilon\delta \text{sech}^2(\delta s)]\mathrm{d}s. \tag{3.13}
\end{aligned}$$

We denote

$$I = \int_{-\infty}^{0} \tilde{p}(k_y(s)) e^{-iyk_y(s)}[1 + i\epsilon\delta \text{sech}^2(\delta s)]\mathrm{d}s, \tag{3.14}$$

from Eq. (3.9), we have

$$\begin{aligned}
k_y(-s) &= -s + i\epsilon \tanh(-\delta s) \\
&= -s - i\epsilon \tanh(\delta s) \\
&= -k_y(s), \tag{3.15}
\end{aligned}$$

104

so, $k_y(s)$ is an odd function of s. From Eq. (3.7), we know $\tilde{p}(k_y)$ is even of k_y, so,

$$\tilde{p}(k_y(-s)) = \tilde{p}(-k_y(s)) = \tilde{p}(k_y(s)). \tag{3.16}$$

Thus, the integral in Eq. (3.14) becomes

$$I = \int_{-\infty}^{0} \tilde{p}(k_y(s))e^{-iyk_y(s)}[1 + i\epsilon\delta\text{sech}^2(\delta s)]\mathrm{d}s$$

$$u = -s$$

$$= \int_{\infty}^{0} \tilde{p}(k_y(-u))e^{-iyk_y(-u)}[1 + i\epsilon\delta\text{sech}^2(-\delta u)]\mathrm{d}u(-1)$$

insert in Eqs. (3.15) and (3.16)

$$= \int_{0}^{\infty} \tilde{p}(k_y(u))e^{iyk_y(u)}[1 + i\epsilon\delta\text{sech}^2(\delta u)]\mathrm{d}u.$$

So, the inverse Fourier transform Eq. (3.13) becomes

$$p(x, y, z) = \frac{1}{2\pi}[\int_{-\infty}^{0} + \int_{0}^{\infty}]\tilde{p}(k_y(s))e^{-iyk_y(s)}[1 + i\epsilon\delta\text{sech}^2(\delta s)]\mathrm{d}s$$

$$= \frac{1}{2\pi}\int_{0}^{\infty} \tilde{p}(k_y(s))(e^{iyk_y(s)} + e^{-iyk_y(s)})[1 + i\epsilon\delta\text{sech}^2(\delta s)]\mathrm{d}s$$

$$= \frac{1}{2\pi}\int_{0}^{\infty} \tilde{p}(k_y(s))2\cos(yk_y(s))[1 + i\epsilon\delta\text{sech}^2(\delta s)]\mathrm{d}s. \tag{3.17}$$

From Eq. (3.17) we see that we need to care about only the contribution from the region $s = \text{Re}(k_y) > 0$ to evaluate the integral in Eq. (3.17), and obtain the inverse Fourier transform.

In implementation, it was found([9]) that suitable values of ϵ and δ could be determined as follows. The rightmost singularity on the positive real k_y axis occurs at $k_y = k_{x1}^{(0)}(\omega)$, where $k_{xm}^{(0)}$ is the eigenvalue of the mth mode with $k_y = 0$. And for increasing $\text{Re}(k_y) > k_{x1}^{(0)}$, the integrand decays exponentially, which can be seen from Eq. (3.7). Integrations were carried out to $\text{Re}\{k_y\} = k_{ymax} = 1.4k_{x1}^{(0)}(\omega)$ typically. The value $\epsilon = k_{ymax}/250$ was used. For the examples in this chapter, the k_y integrations employed a trapezoidal rule on the interval $0 \leq \text{Re}\{k_y\} \leq k_{ymax}$ using $N_{k_y} = 513$ points. The value of δ was chosen so that the argument of the tanh function was

unity at the sixth k_y step, i.e., $\delta = (6\Delta k_y)^{-1}$, where $\Delta k_y = k_{ymax}/(N_{k_y} - 1)$.

3.3 Numerical Examples

In this section, we consider several examples. The first one is a range-independent problem with which we want to check our three-dimensional coupled modes model. The second one is a cosine-bell shaped ridge problem. We use analytical solutions for eigenvalues and eigenfunctions for both of these two examples.

3.3.1 Check Our Three-Dimensional Coupled Modes Model with a Range Independent Waveguide

The waveguide consists of a 200 m depth homogeneous water layer bounded above by a pressure-release surface and below by a rigid bottom. The sound speed in water is 1500 m/s. The point source is located at $(x_s, y_s, z_s) = (0\ \text{m}, 0\ \text{m}, 100\ \text{m})$, and the frequency is 50 Hz. Fig. 3-3 shows transmission loss versus range (r-axis in the two-dimensional model while x-axis in the three-dimensional model) at a depth of 100 m, from two-dimensional model and three-dimensional model. As observed, the two-dimensional and three-dimensional solutions are in perfect agreement.

3.3.2 Pressure Field in a Waveguide with a Cosine-Bell Shaped Ridge at the Bottom

In this example, we consider a two-dimensional waveguide with a cosine-bell ridge on the ocean floor. The water depth is 200 m and sound speed is 1470 m/s in the homogeneous water layer.

The planar upper surface is taken as free to model an open ocean surface, while the rigid bottom surface contains a simple cosine-bell shaped ridge model with a total width of 100 m and height of 50 m, centered on $x = 250$ m. A 30-Hz point source is situated at $(x_s, y_s, z_s) = (0\ \text{m}, 0\text{m}, 50\ \text{m})$.

106
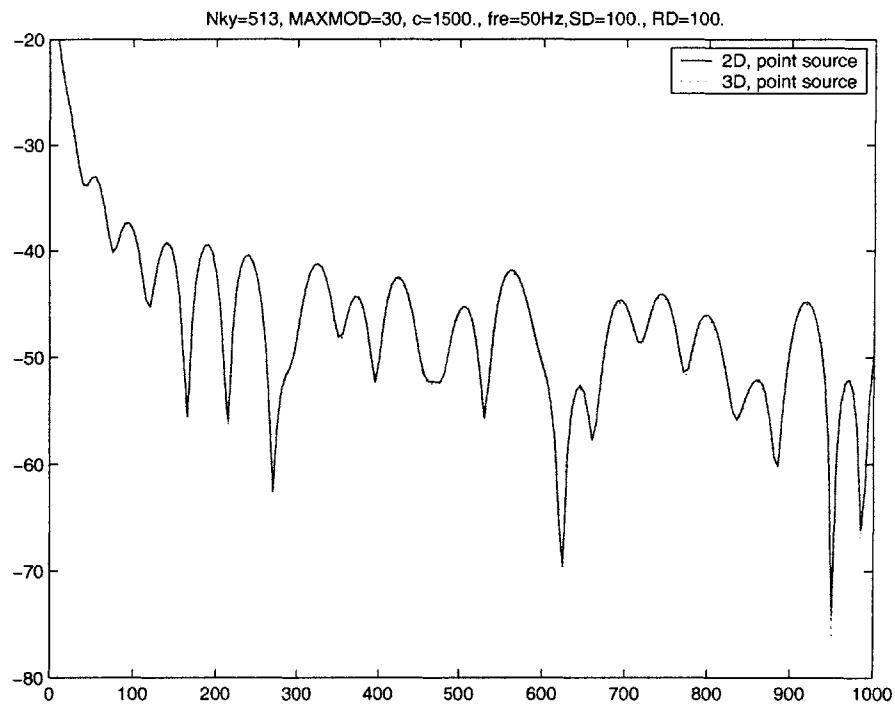
Figure 3-3: Results for a range-independent problem from our two-dimensional model and three-dimensional model.

Figs. 3-4, 3-5 and 3-6 show the modulus of the pressure field in three horizontal planes, i.e., they contain the values $|p(x, y, z)|$, 0 m $\leq x \leq$ 850 m, 0 m $\leq y \leq$ 600 m, at the depths $z = 35, 65, 135$ m. These depths are, respectively, slightly above the source, slightly below the source, and slightly above the ridge. In all these three figures, and especially the third, interference between incident and backscattered field is clearly visible in the region between the source and the ridge.
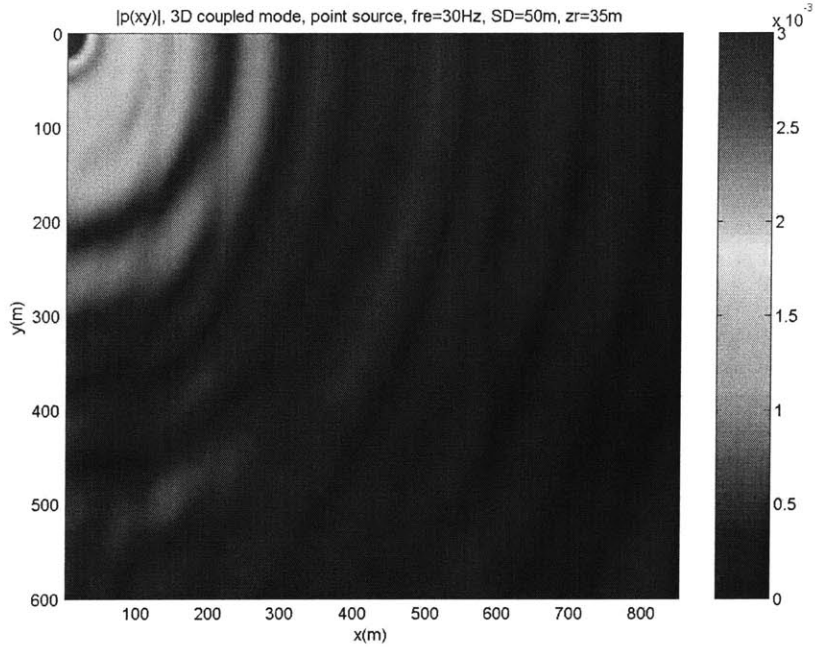
Figure 3-4: $|p(x, y, 35)|$, fre $= 30$ Hz, SD $= 50$ m.

Fig. 3-7 depicts the behavior of the pressure field in the vertical plane. Once again, interference between right-going (incident) and left-going (reflected) waves is visible between the source and the ridge.

This example is solved successfully by Fawcett and Dawson ([9]), and our results are consistent with those presented in paper [9].
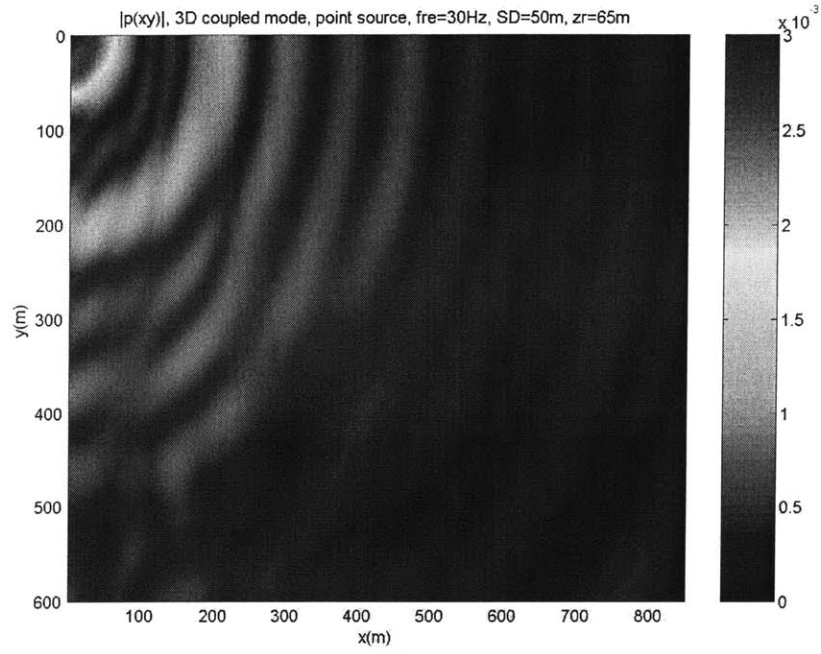
Figure 3-5: $|p(x, y, 65)|$, fre = 30 Hz, SD = 50 m.
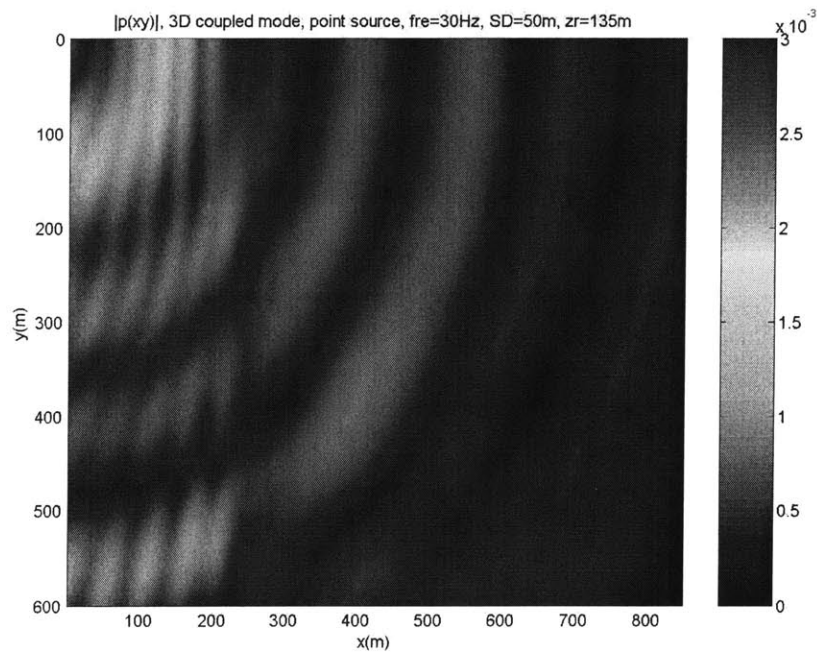
Figure 3-6: $|p(x, y, 135)|$, fre = 30 Hz, SD = 50 m.
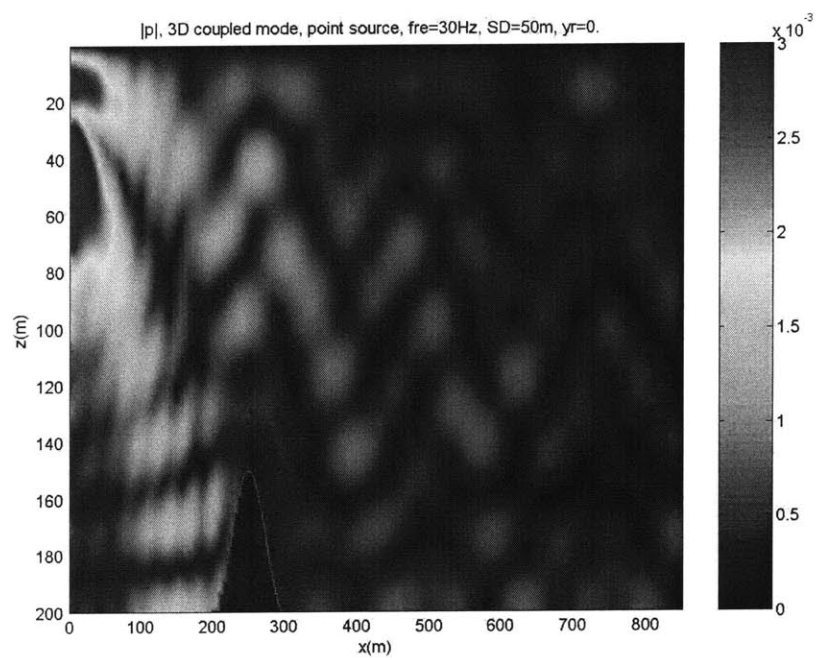
Figure 3-7: $|p(x, 0, z)|$, fre $= 30$ Hz, SD $= 50$ m.

Chapter 4

Conclusion and Future Work

In this thesis, we investigated the coupled mode solution in range-dependent waveguides. Based on C-SNAP, which is a one-way coupled modes model, we developed a two-way coupled modes model. This model works for two-dimensional problems, i.e., for problems with a point source in cylindrical geometry, or problems with a line source in plane geometry. The environment may be range-dependent, consisting of a series of horizontally stratified fluid filled regions. Each of the regions consists of a water layer and a sediment or bottom layer. The two-way C-SNAP is written in standard Fortran. An equivalent two-way coupled modes model written in Matlab is also developed, in which analytical solutions for eigenfunctions and eigenvalues are applied. This model works only for ideal waveguides which consist of a homogeneous water layer bounded above by a pressure-release surface and below by a rigid or soft bottom.

With Fourier transform based on a sequence of two-dimensional problems, we extend the two-dimensional coupled modes model to an three-dimensional model. This method can serve to model acoustic scattering from ridgelike bathymetry, or surface features such as ice ridges, in a realistic ocean waveguide model.

Until now, the three-dimensional model, which is based on the two-dimensional coupled modes model written in Matlab, can solve problems for ideal waveguides only. Next, we will apply the two-way C-SNAP to solve the two-dimensional problems in the three-dimensional model. In addition, we will try to use our three-dimensional

model to solve problems with more complicated waveguides.

Appendix A

Eigenfunction of Proper Modes in the Pekeris Waveguide

We write the eigenfunction as

$$\Psi_m(z) = \begin{cases} A_m \sin(k_{zm}z), & 0 \leq z \leq h \\ B_m e^{-\gamma_m z}, & z > h \end{cases}$$

To determine A_m and B_m, we apply

1. Continuity of pressure at $z = h$.

2. Orthonormal property of $\Psi_m(z)$.

Thus we have

$$\begin{cases} A_m \sin(k_{zm}h) = B_m e^{-\gamma_m h} \implies B_m = A_m \sin(k_{zm}h) e^{\gamma_m h}, \\ \int_0^\infty \frac{1}{\rho(z)} \Psi_m^2(z) \mathrm{d}z = \int_0^h \frac{1}{\rho} [A_m \sin(k_{zm}z)]^2 \mathrm{d}z + \int_h^\infty \frac{1}{\rho_1} [B_m e^{-\gamma_m z}]^2 \mathrm{d}z = 1. \end{cases}$$

So,

$$\int_0^h \frac{1}{\rho} A_m^2 \sin^2(k_{zm}z)\mathrm{d}z + \int_h^\infty \frac{1}{\rho_1} B_m^2 e^{-2\gamma_m z}\mathrm{d}z$$

$$=\frac{1}{\rho} A_m^2 \int_0^h \sin^2(k_{zm}z)\mathrm{d}z + \frac{1}{\rho_1} A_m^2 \sin^2(k_{zm}h)e^{2\gamma_m h} \int_h^\infty e^{-2\gamma_m z}\mathrm{d}z$$

$$=\frac{1}{\rho} A_m^2 \left[\frac{h}{2} - \frac{1}{2}\frac{\sin(2k_{zm}h)}{2k_{zm}}\right] + \frac{A_m^2}{\rho_1} \sin^2(k_{zm}h)\frac{1}{2\gamma_m}$$

$$=A_m^2 \left[\frac{1}{2\rho}(h - \frac{\sin(2k_{zm}h)}{2k_{zm}}) + \frac{1}{2\rho_1}\frac{1}{\gamma_m} \sin^2(k_{zm}h)\right]$$

$$=1,$$

thus we obtain

$$A_m = \sqrt{2} \left[\frac{1}{\rho}(h - \frac{\sin(2k_{zm}h)}{2k_{zm}}) + \frac{1}{\rho_1}\frac{1}{\gamma_m} \sin^2(k_{zm}h)\right]^{-\frac{1}{2}},$$

and

$$B_m = A_m \sin(k_{zm}h)e^{\gamma_m h}.$$

114

Appendix B

Input File of C-SNAP for Fig. 1-7

```
FLAT, IDEAL WAVEGUIDE WITH PRESSURE-SURFACE AND HARD BOTTOM
 1
 50.
 1    80    80
 100, 0
 100.  0.   0.    0.                    1         ! REG   1
   0.  1500.
 100.  1500.
 3900.  1.5  0.0
   0.  1800.
 3900.  1800.
  1.5   0.0     1.0E10
 0.  0.
 100.0   0.   0.    0.4                 0         ! REG   2
   0.  1500.
 100.  1500.
 3900.  1.5  0.0
   0.  1800.
 3900.  1800.
  1.5   0.0     1.0E10
 0.  0.
 MATCH 4
 NMESH 4
 !OPTMZ
 TLRAN,COH,PLT
 XAXIS  0., 4.0, 12., 1.
 YAXIS  40.  90.  7.5  10.
 0.    4.0  0.005
 25.  50.
```

Appendix C

Eigenvalue and Eigenfunction for the Configuration in Fig. 1-9

For $0 \leq z \leq h$(cf. Fig. 1-9),

$$
\begin{aligned}
\Psi_m(z) &= \Psi_{dm}(z) + \Psi_{um}(z) \\
&= a_m e^{ik_{zm}z} + b_m e^{-ik_{zm}z},
\end{aligned}
\tag{C.1}
$$

since $\Psi_m(0) = 0$, thus $b_m = -a_m$, so

$$
\begin{aligned}
\Psi_m(z) &= a_m 2i \sin(k_{zm}z) \\
&= A_m \sin(k_{zm}z).
\end{aligned}
\tag{C.2}
$$

For $h \leq z \leq h + H$,

$$
\begin{aligned}
\Psi_m(z) &= \Psi_{dm}(z) + \Psi_{um}(z) \\
&= c_m e^{ik_{1zm}z} + d_m e^{-ik_{1zm}z},
\end{aligned}
\tag{C.3}
$$

insert in hard boundary condition at $z = h + H$,

$$
\left. \frac{\mathrm{d}\Psi_m(z)}{\mathrm{d}z} \right|_{z=h+H} = 0,
$$

117

we have

$$d_m = c_m e^{i2k_{1zm}(h+H)},$$

so, Eq. (C.3) becomes

$$
\begin{aligned}
\Psi_m(z) &= c_m e^{ik_{1zm}z} + c_m e^{i2k_{1zm}(h+H)} e^{-ik_{1zm}z} \\
&= c_m e^{ik_{1zm}(h+H)} \left\{ e^{ik_{1zm}[z-(h+H)]} + e^{-ik_{1zm}[z-(h+H)]} \right\} \\
&= c_m e^{ik_{1zm}(h+H)} 2\cos\{k_{1zm}[z-(h+H)]\} \\
&= B_m e^{ik_{1zm}(h+H)} \cos\{k_{1zm}[z-(h+H)]\}.
\end{aligned}
\tag{C.4}
$$

Thus, we can write the eigenfunction as

$$
\Psi_m(z) =
\begin{cases}
A_m \sin(k_{zm}z), & 0 \le z \le h \\
B_m e^{ik_{1zm}(h+H)} \cos\{k_{1zm}[z-(h+H)]\}, & h \le z \le h+H
\end{cases}
\tag{C.5}
$$

Apply continuity of pressure and continuity of normal component of particle velocity at $z = h$, we can obtain the eigenvalue equation. Together with the orthonormal property of $\Psi_m(z)$, we can determine A_m and B_m.

With continuity of pressure at $z = h$, we have

$$A_m \sin(k_{zm}h) = B_m e^{ik_{1zm}(h+H)} \cos(k_{1zm}H), \tag{C.6}$$

with continuity of normal component of particle velocity, we have

$$
\begin{aligned}
\frac{1}{\rho} A_m k_{zm} \cos(k_{zm}h) &= -\frac{1}{\rho_1} B_m e^{ik_{1zm}(h+H)} k_{1zm} \sin[-k_{1zm}H] \\
&= \frac{1}{\rho_1} B_m k_{1zm} e^{ik_{1zm}(h+H)} \sin(k_{1zm}H).
\end{aligned}
\tag{C.7}
$$

Divide Eq. (C.6) by Eq. (C.7), we have

$$\frac{\rho \tan(k_{zm}h)}{k_{zm}} = \frac{\rho_1}{k_{1zm}\tan(k_{1zm}H)},$$

or,

$$\tan(k_{zm}h)\tan(k_{1zm}H) = \frac{\rho_1 k_{zm}}{\rho k_{1zm}}. \tag{C.8}$$

Eq. (C.8) is the eigenvalue equation for the configuration in Fig. 1-9.

With orthonormal property of $\Psi_m(z)$, i.e., $\int_0^\infty \frac{1}{\rho(z)}\Psi_m^2(z)\mathrm{d}z = 1$, we have

$$\int_0^h \frac{1}{\rho}A_m^2\sin^2(k_{zm}z)\mathrm{d}z + \int_h^{h+H} \frac{1}{\rho_1}B_m^2 e^{2ik_{1zm}(h+H)}\cos^2\{k_{1zm}[z-(h+H)]\}\mathrm{d}z$$

$$=\frac{A_m^2}{\rho}\left[\frac{h}{2}-\frac{\sin 2k_{zm}h}{4k_{zm}}\right] + \frac{B_m^2}{\rho_1}e^{2ik_{1zm}(h+H)}\left[\frac{H}{2}+\frac{\sin 2k_{1zm}H}{4k_{1zm}}\right]$$

insert in $B_m = A_m\frac{\sin(k_{zm}h)}{\cos(k_{1zm}H)}e^{-ik_{1zm}(h+H)}$

$$=\frac{A_m^2}{\rho}\left[\frac{h}{2}-\frac{\sin 2k_{zm}h}{4k_{zm}}\right] + \frac{1}{\rho_1}A_m^2\frac{\sin^2(k_{zm}h)}{\cos^2(k_{1zm}H)}\left[\frac{H}{2}+\frac{\sin 2k_{1zm}H}{4k_{1zm}}\right]$$

$$=A_m^2\left[\frac{1}{\rho}(\frac{h}{2}-\frac{\sin 2k_{zm}h}{4k_{zm}}) + \frac{1}{\rho_1}\frac{\sin^2(k_{zm}h)}{\cos^2(k_{1zm}H)}(\frac{H}{2}+\frac{\sin 2k_{1zm}H}{4k_{1zm}})\right]$$

$$=1,$$

so we obtain

$$A_m = \left[\frac{1}{\rho}(\frac{h}{2}-\frac{\sin 2k_{zm}h}{4k_{zm}}) + \frac{1}{\rho_1}\frac{\sin^2(k_{zm}h)}{\cos^2(k_{1zm}H)}(\frac{H}{2}+\frac{\sin 2k_{1zm}H}{4k_{1zm}})\right]^{-\frac{1}{2}},$$

and

$$B_m = A_m\frac{\sin(k_{zm}h)}{\cos(k_{1zm}H)}e^{-ik_{1zm}(h+H)}.$$

119

Appendix D

Eigenvalue Equation for the Leaky Modes in the Pekeris Waveguide

The eigenfunction of the leaky modes can be written as(cf. Fig. D-1)

$$\Psi_m(z) = \begin{cases} A_m \sin k_{zm}z, & 0 \le z \le h \\ B_m e^{ik_{1zm}z}, & z \ge h \end{cases}$$
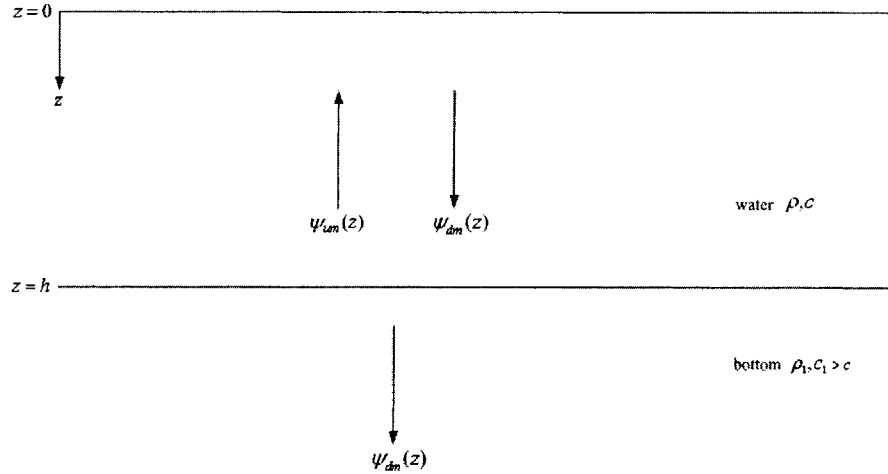
Figure D-1: Eigenfunction for leaky modes in the Pekeris waveguide.

Apply continuity of pressure and continuity of the normal particle velocity at $z = h$, we can obtain the eigenvalue equation.

Continuity of pressure at $z = h$ gives

$$A_m \sin k_{zm} h = B_m e^{i k_{1zm} h}. \tag{D.1}$$

Continuity of normal particle velocity at $z = h$ gives

$$\frac{1}{\rho} A_m k_{zm} \cos k_{zm} h = \frac{1}{\rho_1} B_m i k_{1zm} e^{i k_{1zm} h}. \tag{D.2}$$

Divide Eq. (D.1) by Eq. (D.2), we have

$$\frac{\rho}{k_{zm}} \tan(k_{zm} h) = \frac{\rho_1}{i k_{1zm}},$$

or,

$$\cot(k_{zm} h) = i \frac{\rho k_{1zm}}{\rho_1 k_{zm}}. \tag{D.3}$$

Appendix E

Solve Eq. (1.61) with Endpoint Method

E.1 Endpoint Method

The endpoint method ([11]) is a powerful method to construct the one-dimensional Green's function $\Gamma(x, x_0)$ which satisfies

$$P_0(x)\frac{\mathrm{d}^2\Gamma(x, x_0)}{\mathrm{d}x^2} + P_1(x)\frac{\mathrm{d}\Gamma(x, x_0)}{\mathrm{d}x} + P_2(x)\Gamma(x, x_0) = -\delta(x - x_0), \qquad \text{(E.1)}$$

on the interval $a \leq x \leq b$ and homogeneous boundary conditions or the Sommerfeld radiation condition at the two ends $x = a$ and $x = b$. The Green's function $\Gamma(x, x_0)$ is constructed from linearly independent solutions $u_a(x)$ and $u_b(x)$ of the homogeneous version of Eq. (E.1) which satisfy the boundary conditions at $x = a$ and $x = b$, respectively.

$$\Gamma(x, x_0) = \begin{cases} \Gamma_<(x, x_0) = -\frac{1}{C}u_a(x)u_b(x_0), & a \leq x \leq x_0 \\ \\ \Gamma_>(x, x_0) = -\frac{1}{C}u_a(x_0)u_b(x), & x_0 \leq x \leq b \end{cases} \qquad \text{(E.2)}$$

where

$$C = P_0(x_0)W,$$

and the Wronskian W is

$$W = \begin{vmatrix} u_a(x_0) & u_b(x_0) \\ u_a'(x_0) & u_b'(x_0) \end{vmatrix} = u_a(x_0)u_b'(x_0) - u_a'(x_0)u_b(x_0).$$

Next, let us show the derivation of Eq. (E.2).

We write the solution of Eq. (E.1) in the form

$$\Gamma(x, x_0) = \begin{cases} Au_a(x)u_b(x_0), & a \leq x \leq x_0 \\[2mm] Au_a(x_0)u_b(x), & x_0 \leq x \leq b \end{cases} \tag{E.3}$$

$\Gamma(x, x_0)$ satisfies the boundary conditions at the two ends $x = a$ and $x = b$, and $\Gamma(x, x_0)$ is continuous at $x = x_0$.

Integrate Eq. (E.1) from $x_0 - \epsilon$ to $x_0 + \epsilon$, and let $\epsilon \to 0$, we have

$$\lim_{\epsilon \to 0} \int_{x_0-\epsilon}^{x_0+\epsilon} P_0(x)\frac{\mathrm{d}^2\Gamma(x, x_0)}{\mathrm{d}x^2}\mathrm{d}x + \lim_{\epsilon \to 0} \int_{x_0-\epsilon}^{x_0+\epsilon} P_1(x)\frac{\mathrm{d}\Gamma(x, x_0)}{\mathrm{d}x}\mathrm{d}x + \lim_{\epsilon \to 0} \int_{x_0-\epsilon}^{x_0+\epsilon} P_2(x)\Gamma(x, x_0)\mathrm{d}x$$

$$= -\lim_{\epsilon \to 0} \int_{x_0-\epsilon}^{x_0+\epsilon} \delta(x - x_0)\mathrm{d}x. \tag{E.4}$$

Because $\Gamma(x, x_0)$ is continuous at $x = x_0$, so both the second term and the third term are zero, and

$$\lim_{\epsilon \to 0} \int_{x_0-\epsilon}^{x_0+\epsilon} P_0(x)\frac{\mathrm{d}^2\Gamma(x, x_0)}{\mathrm{d}x^2}\mathrm{d}x = P_0(x_0)\lim_{\epsilon \to 0} \left[\frac{\mathrm{d}\Gamma(x_0 + \epsilon, x_0)}{\mathrm{d}x} - \frac{\mathrm{d}\Gamma(x_0 - \epsilon, x_0)}{\mathrm{d}x}\right]$$

Insert in Eq. (E.3)

$$= P_0(x_0)\lim_{\epsilon \to 0} \left[Au_a(x_0)u_b'(x_0 + \epsilon) - Au_a'(x_0 + \epsilon)u_b(x_0)\right]$$

$$= P_0(x_0)\left[Au_a(x_0)u_b'(x_0) - Au_a'(x_0)u_b(x_0)\right],$$

So, Eq. (E.4) yields

$$P_0(x_0)\left[Au_a(x_0)u_b'(x_0) - Au_a'(x_0)u_b(x_0)\right] = -1,$$

thus,

$$A = \frac{-1}{P_0(x_0)\left[u_a(x_0)u_b'(x_0) - u_a'(x_0)u_b(x_0)\right]} = -\frac{1}{P_0(x_0)W}, \qquad \text{(E.5)}$$

where

$$W = \begin{vmatrix} u_a(x_0) & u_b(x_0) \\ u_a'(x_0) & u_b'(x_0) \end{vmatrix}.$$

Insert Eq. (E.5) into Eq. (E.3), we obtain the Green's function Eq. (E.2).

E.2 Apply the Endpoint Method to Solve Eq. (1.61)

To solve the ODE

$$\frac{\mathrm{d}^2\Phi_n(x)}{\mathrm{d}x^2} + k_{xn}^2\Phi_n(x) = -\frac{\delta(x)\Psi_n(z_s)}{\rho(z_s)}, \qquad \text{(E.6)}$$

i.e.,

$$\frac{\rho(z_s)}{\Psi_n(z_s)}\frac{\mathrm{d}^2\Phi_n(x)}{\mathrm{d}x^2} + \frac{\rho(z_s)}{\Psi_n(z_s)}k_{xn}^2\Phi_n(x) = -\delta(x),$$

we have,

$$P_0(x) = \frac{\rho(z_s)}{\Psi_n(z_s)}, \quad P_1(x) = 0, \quad P_2(x) = \frac{\rho(z_s)}{\Psi_n(z_s)}k_{xn}^2, \quad x_0 = 0,$$

and

$$u_a(x) = e^{-ik_{xn}x}, \quad u_b(x) = e^{ik_{xn}x},$$

$$\begin{aligned}
W &= \begin{vmatrix} u_a(0) & u_b(0) \\ u_a'(0) & u_b'(0) \end{vmatrix} \\
&= \begin{vmatrix} 1 & 1 \\ -ik_{xn} & ik_{xn} \end{vmatrix} \\
&= 2ik_{xn},
\end{aligned}$$

125

$$C = P_0(0)W = \frac{\rho(z_s)}{\Psi_n(z_s)} 2ik_{xn},$$

Thus, we obtain the solution:

for $x < 0$,

$$\begin{aligned}
\Phi_n(x) &= -\frac{1}{C} u_a(x) u_b(0) \\
&= -\frac{\Psi_n(z_s)}{\rho(z_s)} \frac{1}{2ik_{xn}} e^{-ik_{xn}x},
\end{aligned}$$

for $x > 0$,

$$\begin{aligned}
\Phi_n(x) &= -\frac{1}{C} u_a(0) u_b(x) \\
&= -\frac{\Psi_n(z_s)}{\rho(z_s)} \frac{1}{2ik_{xn}} e^{ik_{xn}x},
\end{aligned}$$

the uniform solution is

$$\Phi_n(x) = \frac{i}{2\rho(z_s)} \Psi_n(z_s) \frac{e^{ik_{xn}|x|}}{k_{xn}}.$$

Appendix F

Notifications in Modifying the One-Way C-SNAP to a Two-Way Coupled Modes Model

F.1 Square Root Problem

In our two-way coupled modes model, we use the square root with a nonnegative imaginary part, to be consistent with the exponential term

$$e^{ikr} = e^{i(\alpha+i\beta)r} = e^{i\alpha r}e^{-\beta r}, \quad \beta \geq 0$$

in representing the outgoing field.

In Matlab, the function $SQRT$ returns a complex number with nonnegative imaginary part, for example,

```
>> sqrt(-1)
ans =

          0 + 1.000000000000000i
>> sqrt(3+i)
ans =
  1.75531730182443 + 0.28484878459314i
```

While in Fortran, the result of *CDSQRT(x)* has a value equal to the square root of x. A result of type complex is the principal value, with the real part greater than or equal to zero. When the real part of the result is zero, the imaginary part is greater than or equal to zero. To make sure that the returned number has a nonnegative imaginary part, we use a function, *CDSRT.F*, from the project COUPLE.

```
      COMPLEX*16 FUNCTION CDSRT(Z)
C
C     THIS FUNCTION PROVIDES A SQUARE ROOT WITH A
C     NON-NEGATIVE IMAGINARY PART.
C
CHS   H. SCHMIDT, 14.APR.87. CHANGED TO WORK CORRECTLY FOR
CHS     SMALL NEGATIVE IMAGINARY PART OF THE ARGUMENT BY MOVING
CHS     THE BRANCH CUT TO THE NEGATIVE IMAGINARY AXIS.
C
      IMPLICIT REAL*8 (A-H,O-Z)
      COMPLEX*16 Z,U,W
C
CHS      IF (DREAL(Z) .LE. 0.0D0) THEN
CHS         CDSRT=DCMPLX(0.0D0,1.0D0)*CDSQRT(-Z)
CHS      ELSE
CHS         CDSRT=CDSQRT(Z)
CHS      END IF
C
      U=CDSQRT(Z)
      W=DCMPLX(-1.0D0,0.0D0)
      IF(DIMAG(U) .LT. 0.0D0) U=W*U
      CDSRT=U
C
      RETURN
      END
```

F.2   Option OPTMZ in C-SNAP

The function of the option OPTMZ is explained by [10] as below:

This code word may be used to limit the maximum number of modes which are propagated out in range. The criterion consists in removing, starting from the highest order mode, all the modes that cumulatively contribute for a minor fraction only of the total field, namely at a level corresponding to the round off error of the numerical scheme. The advantage is a speed up of the code.

However, the function of OPTMZ conflicts with the algorithm we applied in our two-way coupled modes model. So, never use this option to run two-way coupled modes model.

Appendix G

An Analytical Solution for Benchmark Problem 1, Case 1

In this part we review the analytical solution given by Buckingham and Tolstoy ([4]) for benchmark problem 1, case 1, which is the two-dimensional, "ideal" wedge problem: The acoustic field is required in a wedge, with pressure-release boundaries, which contains a line source parallel to the apex.

Fig. G-1 shows the geometry of the wedge and the cylindrical coordinates used in the analysis. The medium is a homogeneous fluid, the line source is parallel to the apex, and the boundaries are plane, pressure release surfaces.

G.1   The Analytical Solution

As suggested by ([4]), the velocity potential is found to be the following sum of uncoupled normal modes:

$$\Psi = \frac{2}{\theta_0} \sum_{m=1}^{\infty} I_{\nu_m}(r, r') \sin(\nu_m \theta) \sin(\nu_m \theta'), \tag{G.1}$$

where θ_0 is the wedge angle, r and r' are the ranges of the receiver and source from the apex of the wedge, θ and θ' are the angular depths of the receiver and source
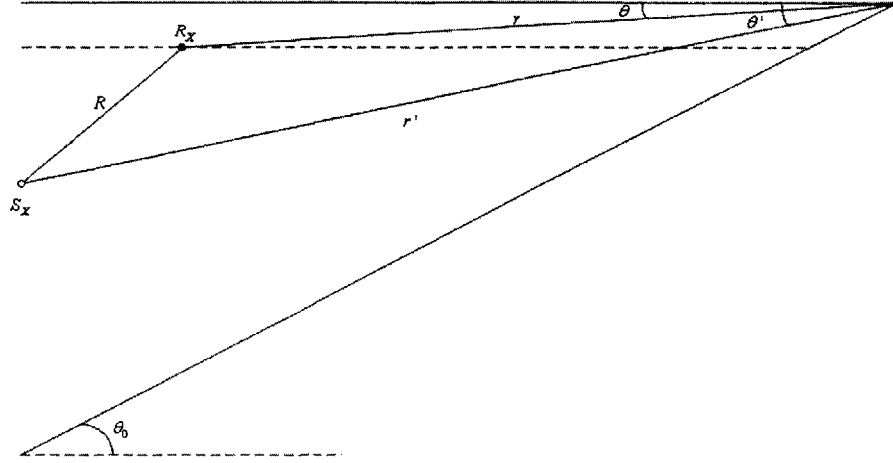
Figure G-1: Coordinates of the source, S_X and receiver, R_X, in the ideal wedge. The wedge angle is θ_0 and the radial distance between the source and receiver is R.

measured about the apex, and

$$\nu_m = m\frac{\pi}{\theta_0}. \tag{G.2}$$

The mode coefficients in Eq. (G.1) are

$$I_{\nu_m}(r, r') = \int_0^\infty \frac{p}{p^2 - k^2} J_{\nu_m}(pr) J_{\nu_m}(pr') \mathrm{d}p, \tag{G.3}$$

where k is the wavenumber of the source radiation and $J_{\nu_m}(\ )$ is a Bessel function of the first kind of order ν_m. When the result (G.3) is substituted into Eq. (G.1), the final expression for the field is found to be

$$\Psi(r, r', \theta, \theta') = \frac{i\pi}{\theta_0} \sum_{m=1}^\infty J_{\nu_m}(kr_<) H_{\nu_m}^{(1)}(kr_>) \sin(\nu_m\theta) \sin(\nu_m\theta'), \tag{G.4}$$

where $r_< = \min(r, r')$, $r_> = \max(r, r')$, and $H_{\nu_m}^{(1)}(\ )$ is the Hankel function of the first kind of order ν_m.

To calculate the transmission loss (TL), we have to find the reference velocity potential. The velocity potential of the field generated by a line source in an infinite medium is

$$\Phi(R) = \frac{i}{4} H_0^{(1)}(kR), \tag{G.5}$$

130

where R is the radial distance from the source to the field point and $H_0^{(1)}(\ )$ is the Hankel function of the first kind of order zero. With R set equal to 1 m, the normalized field in the wedge is

$$\Lambda = \frac{|\Psi(r,r',\theta,\theta')|}{|\Phi(1)|}, \tag{G.6}$$

and the transmission loss in dB is

$$\mathrm{TL} = 20\log_{10}(\Lambda). \tag{G.7}$$

This expression was evaluated for a fixed receiver depth as a function of horizontal range from the source to the apex.

G.2 The Computations

Full details of the parameter values for benchmark problem 1 are listed in section 2.5.3, and the source/receiver configuration in the wedge is illustrated in Fig. 2-14. Some parameters to evaluate Eq. (G.4) for benchmark problem 1 are listed below:

$$\theta_0 = \tan^{-1}(\frac{200}{4000}) \approx 0.049958(\mathrm{rad})$$

$$\theta' = \tan^{-1}(\frac{100}{4000}) \approx 0.024995(\mathrm{rad})$$

$$\nu_m = m\frac{\pi}{\theta_0} \approx 62.9m$$

$$k = \frac{2\pi f}{c} = \frac{2\pi \times 25}{1500.} \approx 0.104720(\mathrm{m}^{-1})$$

$$r_> = r' = \sqrt{100^2 + 4000^2} \approx 4001.2(\mathrm{m})$$

As described in [4], problem arises as calculating $H_{\nu_m}^{(1)}(kr_>)$ for fixed $kr_>$ as $\nu_m \to \infty$, because

$$H_{\nu_m}^{(1)}(X) = J_{\nu_m}(X) + iY_{\nu_m}(X)$$

where $X = kr_>$. For a fixed value of X, as $\nu_m \to \infty$, $J_{\nu_m}(X) \to 0$ while $Y_{\nu_m}(X) \to \infty$. Thus for large ν_m, $H_{\nu_m}^{(1)}(X)$ is an infinite value.

However, from Eq. (G.4) we see, as $\nu_m \to \infty$, $J_{\nu_m}(kr_<) \to 0$, and $H_{\nu_m}^{(1)}(kr_>) \to$

$0+i\infty$, so the product of $J_{\nu_m}(kr_<)$ and $H_{\nu_m}^{(1)}(kr_>)$ may be a finite value. Thus, instead of evaluating $J_{\nu_m}(kr_<)$ and $H_{\nu_m}^{(1)}(kr_>)$ respectively, we apply the Debye asymptotic expansions for large ν_m to evaluate $J_{\nu_m}(kr_<)H_{\nu_m}^{(1)}(kr_>)$.

Debye's Asymptotic Expansion ([1]):

If α is fixed and positive and ν is large and positive, then

$$J_\nu(\nu \mathrm{sech}\alpha) \sim \frac{e^{\nu(\tanh\alpha - \alpha)}}{\sqrt{2\pi\nu\tanh\alpha}}\{1 + \sum_{k=1}^{\infty} \frac{u_k(\coth\alpha)}{\nu^k}\},$$

$$Y_\nu(\nu \mathrm{sech}\alpha) \sim -\frac{e^{\nu(\alpha - \tanh\alpha)}}{\sqrt{\frac{1}{2}\pi\nu\tanh\alpha}}\{1 + \sum_{k=1}^{\infty}(-1)^k \frac{u_k(\coth\alpha)}{\nu^k}\},$$

where

$$u_0(t) = 1,$$

$$u_1(t) = (3t - 5t^3)/24,$$

$$u_2(t) = (81t^2 - 462t^4 + 385t^6)/1152,$$

etc.

When ν_m is large (when the value of Y_{ν_m} drops below -10^{10}), we use the Debye asymptotic expansion with the first two terms, and evaluate $J_{\nu_m}(kr_<)H_{\nu_m}^{(1)}(kr_>)$ as below,

$$kr_< = \nu_m \mathrm{sech}\alpha_1 \implies \alpha_1 = \mathrm{asech}(\frac{kr_<}{\nu_m}),$$

$$kr_> = \nu_m \mathrm{sech}\alpha_2 \implies \alpha_2 = \mathrm{asech}(\frac{kr_>}{\nu_m}),$$

and then

$$J_{\nu_m}(\alpha_1)H_{\nu_m}^{(1)}(\alpha_2) = J_{\nu_m}(\alpha_1)[J_{\nu_m}(\alpha_2) + iY_{\nu_m}(\alpha_2)]$$

$$= J_{\nu_m}(\alpha_1)J_{\nu_m}(\alpha_2) + iJ_{\nu_m}(\alpha_1)Y_{\nu_m}(\alpha_2)$$

where

$$J_{\nu_m}(\alpha_1)J_{\nu_m}(\alpha_2) = \frac{e^{\nu_m(\tanh\alpha_1-\alpha_1+\tanh\alpha_2-\alpha_2)}}{2\pi\nu_m\sqrt{\tanh\alpha_1\tanh\alpha_2}}$$
$$\times\{1+\frac{u_1(\coth\alpha_1)}{\nu_m}+\frac{u_2(\coth\alpha_1)}{\nu_m^2}\}\{1+\frac{u_1(\coth\alpha_2)}{\nu_m}+\frac{u_2(\coth\alpha_2)}{\nu_m^2}\},$$

$$J_{\nu_m}(\alpha_1)Y_{\nu_m}(\alpha_2) = -\frac{e^{\nu_m(\tanh\alpha_1-\alpha_1+\alpha_2-\tanh\alpha_2)}}{\pi\nu_m\sqrt{\tanh\alpha_1\tanh\alpha_2}}$$
$$\times\{1+\frac{u_1(\coth\alpha_1)}{\nu_m}+\frac{u_2(\coth\alpha_1)}{\nu_m^2}\}\{1-\frac{u_1(\coth\alpha_2)}{\nu_m}+\frac{u_2(\coth\alpha_2)}{\nu_m^2}\}.$$

In the benchmark problem 1, from the formulas in Section 1.3.2, we may find the number of propagating modes,

$$M = [\frac{2D}{\lambda}]$$
$$D = 200, \lambda = \frac{c}{f} = \frac{1500}{25} = 60$$
$$= [\frac{2\times200}{60}]$$
$$= 6.$$

Moreover, the eigenfunction at source depth are

$$\Psi_m(z_s) = \sqrt{\frac{2\rho}{D}}\sin(k_{zm}z_s), \quad \text{for } m = 1,2,\ldots$$

where $k_{zm} = \frac{m\pi}{D}$, $z_s = \frac{D}{2} \implies k_{zm}z_s = m\frac{\pi}{2}$, $m = 1,2,\ldots$. So, for even modes, i.e., $m = 2n$, $n = 1,2,\ldots$, we have

$$\Psi_{2n}(z_s) = \sqrt{\frac{2\rho}{D}}\sin(m\frac{\pi}{2})\Big|_{m=2n}$$
$$= \sqrt{\frac{2\rho}{D}}\sin(n\pi)$$
$$= 0,$$

thus we can see, only odd-order modes are excited, so only mode 1, 3 and 5 will propagate through the wedge. However, in the near field, many more modes should

133

be included to achieve acceptable accuracy.

G.3   Results

Fig. G-2(a) shows the transmission loss calculated from Eq. (G.7) for benchmark problem 1 case 1. We use 100 modes to generating this result.

Fig. G-2(b) shows an extended view of the field in Fig. G-2(a) over the range 0-1 km.

(a)   (b)
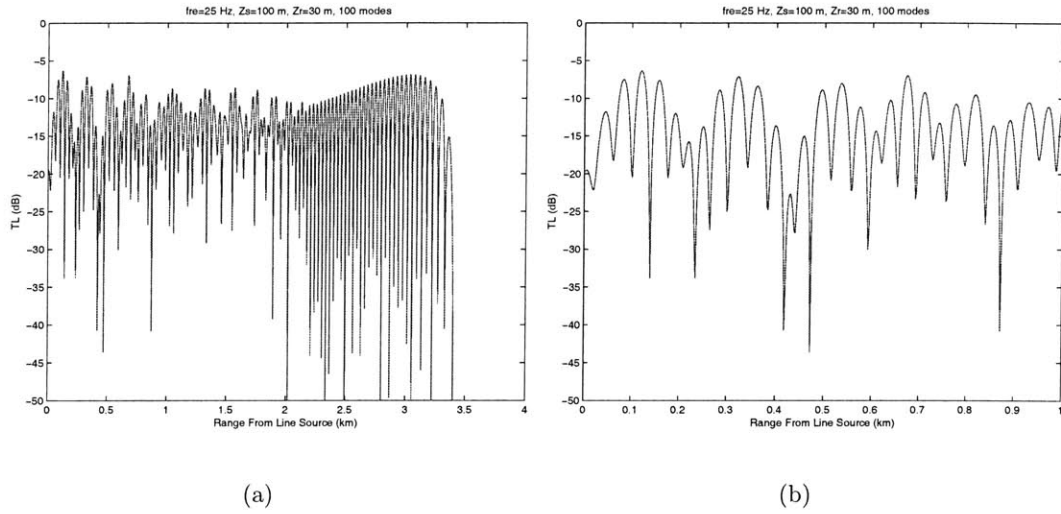
Figure G-2: Transmission loss for benchmark problem 1 case 1, calculated from Eq. (G.7) for a receiver depth of 30 m and frequency of 25 Hz from (a) 0-4 km (b) 0-1 km.

Appendix H

Input File of C-SNAP for Fig. 2-11

```
FLAT, IDEAL WAVEGUIDE WITH RIGID BOTTOM
 1
 50.
 1    100    100
100, 0
200.  0.   0.    0.                    1        ! REG   1
   0.  1500.
 200.  1500.
3800.  1.0E20  0.0
   0.  1.0E5
3800.  1.0E5
 1.0E10  0.0      1.0E5
 0.  0.
 200.0   0.  0.     0.4                0        !  REG   2
   0.  1500.
 200.  1500.
3800.  1.0E20  0.0
   0.  1.0E5
3800.  1.0E5
 1.0E10  0.0      1.0E5
 0.  0.
MATCH 4
NMESH 4
!PLANE
!OPTMZ
TLRAN,COH,PLT
XAXIS  0., 4.0, 12., 1.
YAXIS  40.  90.  7.5  10.
0.  4.0  0.005
100.  100.
```

Appendix I

Input Files for Fig. 2-16 and Fig. 2-17

I.1 Input File of C-SNAP for Fig. 2-16 and Fig. 2-17

```
WEDGE-SHAPED WAVEGUIDE
1
25.
1    90    90
100, 0
200.  0.   0.    0.                    9         ! REG    1
  0.  1500.
200.  1500.
3800. 1.5  0.
  0.  1700.
3800. 1700.
1.5  0.00      1.0E10
0.   0.
  0.0   0.   0.     4.0                0         !  REG   2
4000.0   1.5  0.
  0.     1700.
4000.00  1700.
1.5  0.00      1.0E10
0.   0.
MATCH 4
NMESH 4
!PLANE
!OPTMZ
TLRAN,COH,PLT
XAXIS  0., 4.0, 12., 1.
YAXIS  40.  90.  7.5  10.
0.   4.0  0.005
100.  30.
100.  150.
100.  180.
```

I.2 Input File of COUPLE for Fig. 2-17

```
ASA Benchmark Wedge, Galerkin procedure, 90 modes, 500 steps
4000.  25.0   1.0   1.5    0.0        !HB,FREQ,ROHW,ROHB,DBPWL
1700.0    00.                         !CB,CW
90  0  0  0  0  0                     !M,NATEN,IEIG,NDPTH,IGEOM,IREFL
1  100.0    0.0                       !NSDEP,ZSMIN,ZSINC
2   30.0  120.0                       !NDEP,ZMIN,ZINC
0.01   4.01   0.01                    !RMIN,RMAX,RINC
2   50   0   0                        !N,IPRT,IOUT,MAMP
0.01     500   200.0   2  3   0       !RANGE,IRLIN,DPTH,NPW,NPB,IREIG
0.0      1500.0    .0    1.00         !DEPW,SVPW,DBPWLW,RHOW
200.0    1500.0    .0    1.00
200.0    1700.0    .0    1.5          !DEPB,SVPB,DBPWLB,RHOB
3000.0   1700.0    .0    1.5
4000.0   1700.0   2.5    1.5
4.00     0        0.01   2  3   0
0.0      1500.0    .0    1.00         !DEPW,SVPW,DBPWLW,RHOW
0.01     1500.0    .0    1.00
0.01     1700.0    .0    1.5          !DEPB,SVPB,DBPWLB,RHOB
3000.0   1700.0    .0    1.5
4000.0   1700.0   2.5    1.5
```

138

Appendix J

Input Files for Fig. 2-18 and Fig. 2-19

J.1 Input File of C-SNAP for Fig. 2-18 and Fig. 2-19

```
WEDGE-SHAPED WAVEGUIDE
1
25.
1    90    90
100, 0
200.   0.   0.    0.                    8        ! REG   1
   0.  1500.
 200.  1500.
3800.  1.5  0.5
   0.     1700.
3800.    1700.
 1.5  0.5      1.0E10
 0.  0.
   0.0   0.  0.    4.0                   0        !  REG  2
4000.  1.5  0.5
   0.     1700.
 4000.    1700.
 1.5  0.5      1.0E10
 0.  0.
MATCH 3
NMESH 4
!PLANE
!OPTMZ
TLRAN,COH,PLT
XAXIS  0., 4.0, 12., 1.
YAXIS  40.  90.  7.5  10.
0.  4.0  0.005
100.   30.
100.  150.
100.  180.
```

J.2 Input File of COUPLE for Fig. 2-19

```
ASA Benchmark Wedge, Galerkin procedure, 90 modes, 250 steps
4000.  25.0    1.0    1.5    0.5          !HB,FREQ,ROHW,ROHB,DBPWL
1700.0     00.                            !CB,CW
90  0  0  0  0  0                         !M,NATEN,IEIG,NDPTH,IGEOM,IREFL
1  100.0     0.0                          !NSDEP,ZSMIN,ZSINC
2   30.0  120.0                           !NDEP,ZMIN,ZINC
0.01   4.01   0.01                        !RMIN,RMAX,RINC
2   50    0   0                           !N,IPRT,IOUT,MAMP
0.01       250   200.0    2  3    0       !RANGE,IRLIN,DPTH,NPW,NPB,IREIG
0.0       1500.0    .0    1.00            !DEPW,SVPW,DBPWLW,RHOW
200.0     1500.0    .0    1.00
200.0     1700.0    .5    1.5             !DEPB,SVPB,DBPWLB,RHOB
3000.0    1700.0    .5    1.5
4000.0    1700.0   2.5    1.5
4.00       0        0.01  2  3    0
0.0       1500.0    .0    1.00            !DEPW,SVPW,DBPWLW,RHOW
0.01      1500.0    .0    1.00
0.01      1700.0    .5    1.5             !DEPB,SVPB,DBPWLB,RHOB
3000.0    1700.0    .5    1.5
4000.0    1700.0   2.5    1.5
```

Appendix K

Input File of C-SNAP for Fig. 2-21

```
DOWNSLOPE WEDGE, 12.7 degrees
1
25.
1   160    160
10, 0
 100.0   0.   0.              0.0        8        ! Reg   1
    0.    1500.
 100.    1500.
3900.       2.0    0.500
    0.    1700.
3900.    1700.
2.0    0.50       1.0E10
0.    0.
1000.0   0.   0.              4.         0        ! Reg   2
    0.    1500.
1000.    1500.
3000.       2.0    0.500
    0.    1700.
3000.    1700.
2.0    0.50       1.0E10
0.    0.
!OPTMZ
NMESH   4
MATCH   4
PLANE
TLRAN,COH,PLT
XAXIS  0., 4., 16., 1.0
YAXIS 10    60   10   10
  0.    4.0  0.004
 50.   50.
```

Appendix L

Input File of C-SNAP for

Fig. 2-23(a)

```
DEEP WATER PROPAGATION OVER A SEAMOUNT, REDUCED PRESSURE MATCHING
1
50
1  62  100
100  0
5000.0  0.0   0.0                      0           -1      ! Profile  1
      0.0, 1536.00
  200.0, 1528.00
  700.0, 1502.00
  800.0, 1500.00
 1200.0, 1497.00
 1500.0, 1497.00
 2000.0, 1500.00
 3000.0, 1512.00
 4000.0, 1528.00
 5000.0, 1545.00
     0.
1.0, 0.1, 2000.0
0.0  0.0
5000.0  0.0   0.0                     80            5      ! Profile  2
      0.0, 1536.00
  200.0, 1528.00
  700.0, 1502.00
  800.0, 1500.00
 1200.0, 1497.00
 1500.0, 1497.00
 2000.0, 1500.00
 3000.0, 1512.00
 4000.0, 1528.00
 5000.0, 1545.00
     0.
1.0, 0.1, 2000.0
0.0   0.0
4000.0  0.0   0.0                    100            5      ! Profile  3
      0.0, 1536.00
  200.0, 1528.00
  700.0, 1502.00
  800.0, 1500.00
```

```
 1200.0, 1497.00
 1500.0, 1497.00
 2000.0, 1500.00
 3000.0, 1512.00
 4000.0, 1528.00
     0.
 1.0, 0.1, 2000.0
 0.0   0.0
 5000.0, 0.0   0.0              120.           0      ! Profile  4
     0.0, 1536.00
   200.0, 1528.00
   700.0, 1502.00
   800.0, 1500.00
 1200.0, 1497.00
 1500.0, 1497.00
 2000.0, 1500.00
 3000.0, 1512.00
 4000.0, 1528.00
 5000.0, 1545.00
     0.
 1.0, 0.1, 2000.0
 0.0  0.0
 !LARGE
 MATCH    4
 NMESH    1
 !OPTMZ
 TLRAN,COH,PLT
 XAXIS 0,  200,  16, 40
 YAXIS 60, 120,  10, 10
 0    200  0.1
 100.  0.1
 100.  5000.
```

Appendix M

Hyperbolic Tangent Function $\tanh(x)$

M.1 Definition

$$\tanh(x) = \frac{\sinh(x)}{\cosh(x)} = \frac{e^x - e^{-x}}{2} \Big/ \frac{e^x + e^{-x}}{2} = \frac{e^x - e^{-x}}{e^x + e^{-x}}. \qquad (M.1)$$

M.2 Asymptotic Perperties

1. As $x \to \infty$,

$$\tanh(x) \to \frac{e^x - 0}{e^x + 0} = 1.$$

2. As $x \to -\infty$

$$\tanh(x) \to \frac{0 - e^{-x}}{0 + e^{-x}} = -1.$$

M.3 Special Points

At $x = 0$,

$$\tanh(0) = \frac{e^0 - e^0}{e^0 + e^0} = \frac{1 - 1}{1 + 1} = 0.$$

M.4 Symmetry Property

Since

$$\tanh(-x) = \frac{e^{-x} - e^{x}}{e^{-x} + e^{x}} = -\tanh(x),$$

$\tanh(x)$ is an odd function of x.

M.5 Derivative

$$\begin{aligned}
\tanh'(x) &= \frac{(e^{x} + e^{-x})(e^{x} + e^{-x}) - (e^{x} - e^{-x})(e^{x} - e^{-x})}{(e^{x} + e^{-x})^2} \\
&= \frac{2e^{x}2e^{-x}}{(e^{x} + e^{-x})^2} \\
&= \frac{4}{(e^{x} + e^{-x})^2} \\
\mathrm{sech}\, x &= \frac{1}{\cosh x} = \frac{2}{e^{x} + e^{-x}} \\
&= \mathrm{sech}^2 x.
\end{aligned}$$

M.6   Shape of Function $y = \tanh(x)$

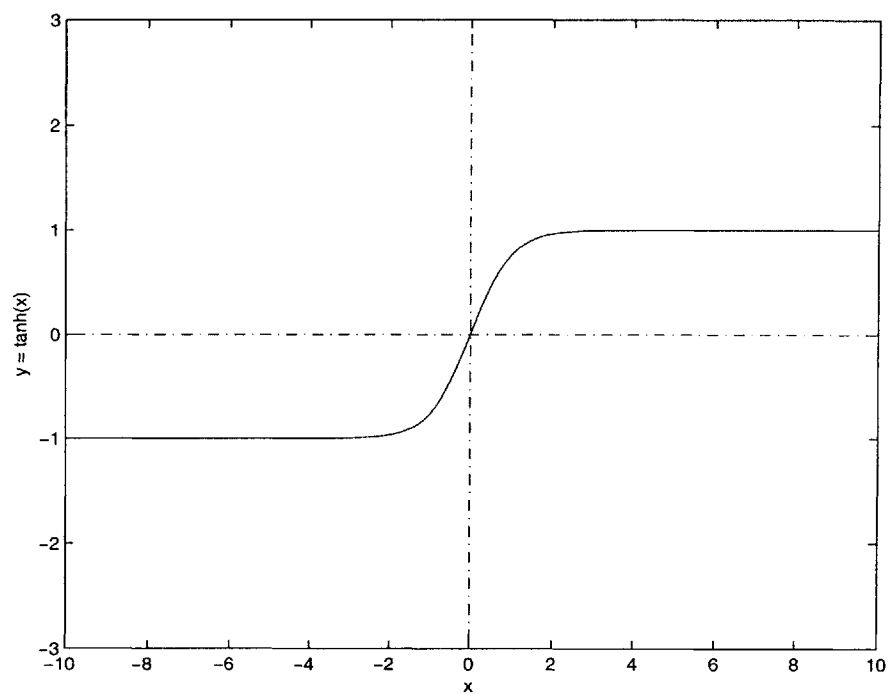The shape of function $y = \tanh(x)$ is shown in Fig. M-1.

Figure M-1: Shape of function $y = \tanh(x)$.

Bibliography

[1] M. Abramowitz and I. A. Stegun. *Handbook of Mathematical Functions with Formulas, Graphs and Mathematical Tables*. Appl. Math. Ser. No. 55. National Bureau of Standards, Washington, DC, 1972.

[2] C. M. Bender and S. A. Orszag. *Advanced Mathematical Methods for Scientists and Engineers*. McGraw-Hill, New York, 1978.

[3] H. Bremmer. The W.K.B. approximation as the first term of a geometricaloptical series. *Comm. Pure Appl. Math.*, 4:105–115, 1951.

[4] M.J. Buckingham and A. Tolstoy. An analytical solution for benchmark problem 1: The "ideal" wedge. *J. Acoust. Soc. Am*, 87:1511–1513, 1990.

[5] M. D. Collins and E. K. Westwood. A higher-order energy-conserving parabolic equation for range-dependent ocean depth, sound speed, and density. *J. Acoust. Soc. Am*, 89:1068–1075, 1991.

[6] Trevor W. Dawson and John A. Fawcett. A boundary integral equation method for acoustic scattering in a waveguide with nonplanar surfaces. *J. Acoust. Soc. Am*, 87:1110–1125, 1990.

[7] R. B. Evans. A coupled mode solution for acoustic propagation in a waveguide with stepwise depth variations of a penetrable bottom. *J. Acoust. Soc. Am.*, 74, 1983.

[8] Richard B. Evans. The decoupling of stepwise coupled modes. *J. Acoust. Soc. Am.*, 80(5), November 1986.

[9] John A. Fawcett and Trevor W. Dawson. Fourier synthesis of three-dimensional scattering in a two-dimensional oceanic waveguide using boundary integral equation methods. *J. Acoust. Soc. Am*, 88:1913–1920, 1990.

[10] C.M. Ferla, M.B. Porter, and F.B. Jensen. *CSNAP: Coupled SACLANTCEN normal mode propagation loss model, SACLANTCEN SM-274*. Underwater Research Division.

[11] George V. Frisk. *Ocean and Seabed Acoustics*. PTR Prentice Hall, 1994.

[12] F.B. Jensen and Ferla C.M. *SNAP: The SACLANTCEN normal-mode acoustic propagation model, SACLANTCEN SM-121*. NATO SACLANT Undersea Research Center, La Spezia, Italy, 1979. [AD A 067 256].

[13] F.B. Jensen and C.M. Ferla. Numerical solutions of range-dependent benchmark problems in ocean acoustics. *J. Acoust. Soc. Am*, 87:1499–1510, 1990.

[14] Finn B. Jensen, William A. Kuperman, Michael B. Porter, and Henrik Schmidt. *Computational Ocean Acoustics*. AIP Press, American Institute of Physics, 1993.

[15] D. Lee. The state-of-the-art parabolic equation approximations as applied to underwater acoustic propagation. Rep. TD-7247, Naval Underwater Systems Center, New London, CT, 1984.

[16] Collins M.D. A split step padeé solution for the parabolic equation method. *Journal of the Acoustical Society of America*, 93:1–7, 1993.

[17] Collins M.D. and E.K. Westwood. A higher order energy conserving parabolic equation for range-dependent ocean depth. *Journal of the Acoustical Society of America*, 89:1068–1075, 1991.

[18] Gregory J. Orris and Michael D. Collins. The spectral parabolic equation and three-dimensional backscattering. *J. Acoust. Soc. Am*, 96:1725–1731, 1994.

[19] M.B. Porter and Reiss E.L. A numerical method for bottom interacting ocean acoustic normal modes. *Journal of the Acoustical Society of America*, 77, 1985.

[20] M.B. Porter, F.B. Jensen, and C.M. Ferla. The problem of energy conservation in one-way models. *J. Acoust. Soc. Am*, 89:1058–1067, 1991.

[21] M. R. Scott and H. A. Watts. Computational solution of linear two-point boundary value problems via orthonormalization. *SIAM J. Numer. Anal.*, 14, 1977.

[22] Ralph A. Stephen. Solutions to range-dependent benchmark problems by the finite-difference method. *J. Acoust. Soc. Am*, 87:1527–1534, 1990.

[23] David J. Thomson. Wide-angle parabolic equation solutions to two range-dependent benchmark problems. *J. Acoust. Soc. Am*, 87:1514–1520, 1990.